CHAPTER 3

Time-Domain Interferometry with Laser-Cooled Atoms

B. Barrett[a], **I. Chan**[a], **C. Mok**[a], **A. Carew**[a], **I. Yavin**[b], **A. Kumarakrishnan**[a], **S. B. Cahn**[c], and **T. Sleator**[d]

[a]*Department of Physics & Astronomy, York University, 4700 Keele St., Toronto, ON M3J 1P3, Canada*
[b]*Department of Physics & Astronomy, McMaster University, 1280 Main St. W, Hamilton, Ontario, Canada L8S 4M1*
[c]*Department of Physics, Yale University, New Haven, Connecticut 06511, USA*
[d]*Department of Physics, New York University, New York, NY 10003, USA*

Contents

Advances in Atomic, Molecular, and Optical Physics, Volume 60, Copyright © 2011 Elsevier Inc.
ISSN 1049-250X, DOI: 10.1016/B978-0-12-385508-4.00003-6.

Abstract

A single-state grating echo interferometer offers unique advantages for time-domain studies of light–matter interactions using laser-cooled atoms, including applications that involve precision measurements of atomic recoil, rotation, and gravitational acceleration. To illustrate the underlying physics, we first discuss the output signal of the interferometer in the absence of spontaneous emission. The influence of spontaneous emission, magnetic sublevels, and the spatial profile of excitations beams on matter wave interference in a two-pulse interferometer is described, followed by a discussion of transit time limited experiments using a multipulse technique that offers several advantages. We also examine the enhancement in signal size achieved by a lattice interferometer. The sensitivity of the interferometer to magnetic gradients and gravitational acceleration is discussed along with extensions to frequency-domain studies of atomic recoil and rotation. Applications of coherent transient effects and echo techniques associated with internal state labeled interferometers that utilize magnetic sublevels of a single hyperfine state are considered for precise measurements

of magnetic interactions such as atomic g-factor ratios. The article concludes with an overview of the suitability of the traditional two-pulse photon echo technique for measurements of atomic lifetimes and studies of superradiant emission in laser-cooled samples.

1. INTRODUCTION AND DESCRIPTION OF TWO-PULSE STANDING WAVE INTERFEROMETER

1.1 Introduction

Matter wave interference has intrigued scientists since the early days of quantum mechanics. It was not until the late 1980s, however, that the field of atom interferometry was born. There have been a series of beautiful experiments carried out over the past two decades that have probed the fundamental nature of matter wave interference using atom interferometers (Berman, 1997). These include interference of "large" objects and of biomolecules (Hackermüller et al., 2004), interference of independently prepared particles (Andrews et al., 1997), and the origin of quantum mechanical complementarity (Durr et al., 1998). Advances in microfabrication techniques and the development of laser-cooling and trapping for neutral atoms has opened up many new possibilities for constructing atomic interferometers (Keith et al., 1988; Weiss et al., 1993). Besides testing the fundamental nature of matter wave interference, atom interferometers play an essential role in many high-precision measurements of fundamental constants, such as the fine structure constant α and the Newtonian constant of gravity. They offer an independent method for determining these constants that expands our understanding of the fundamental nature of physical laws (Cladé et al., 2006; Fixler et al., 2007; Weiss et al., 1993). Moreover, precise measurements of quantities such as the local gravitational field hold promise for technological advances in navigation and mineral exploration (McGuirk et al., 2002).

This article discusses the physics and various extensions of a particular atom interferometer design developed at New York University (NYU) in the mid-1990s (Cahn et al., 1997). The interferometer involves the interaction of a set of pulsed laser fields with a sample of laser-cooled Rb atoms in a magneto-optical trap. A schematic of the experimental setup of this interferometer is shown in Figure 1. The principle of the NYU interferometer is that the interaction of an off-resonant optical standing-wave pulse (made up of traveling waves with k-vectors $\boldsymbol{k}_1$ and $\boldsymbol{k}_2$) with a two-level atomic system effectively modulates the atomic ground-state energy with a spatial period $2\pi/q$, with $\boldsymbol{q} = \boldsymbol{k}_2 - \boldsymbol{k}_1$. The pulse therefore acts as

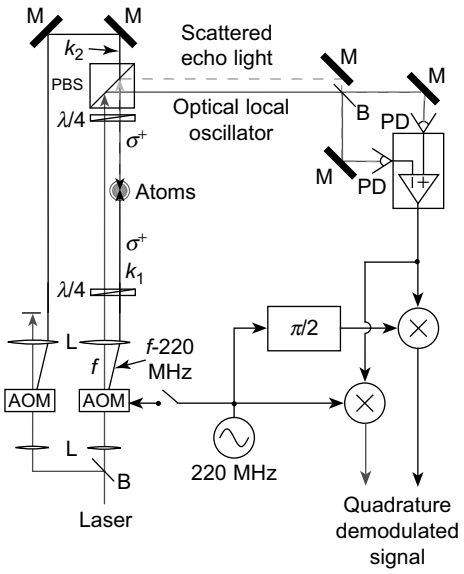

Figure 1 Schematic diagram of the experimental setup (for σ^+-polarized sw experiment). M = mirror, B = beamsplitter, PD = photodiode, AOM = acousto-optic modulator, $\lambda/4$ = quarter-wave plate, L = lens, PBS = polarizing beam splitter.

a phase grating for atomic de Broglie waves, and an initial atomic plane-wave is scattered into a set of diffraction orders differing by multiples of momentum $\hbar\boldsymbol{q}$. A second standing-wave pulse, separated from the first by a time T, produces further diffraction orders, and at various times after the second pulse, these diffraction orders interfere to produce a spatial modulation in the atomic density that can be observed by the scattering of a traveling wave pulse with wavevector $\boldsymbol{k}_2$ into the direction $\boldsymbol{k}_1$. An important property of this interferometer is that a high degree of "collimation" of the atoms is not necessary. This is because, for various times after the second pulse (called *echo* times), the relative phase between interfering diffraction orders is independent of the initial atomic velocity. An interferometer that is based on the cancelation of this Doppler phase is referred to as an *echo* interferometer, in analogy with the spin echo (Hahn, 1950a), or the photon echo (Abella et al., 1965). Another important feature of this interferometer is that the measured signal results from coherences involving a single atomic ground state, making the interference signal relatively insensitive to external electric and magnetic fields.

Like many of the atom interferometers developed over the past two decades, this interferometer can be used to make measurements of various physical quantities of interest to high precision. Examples are the atomic recoil frequency $\omega_q = \hbar q^2/2M$ (M is the mass of the test atom), which is

useful for determining the fine-structure constant α, and inertial effects such as acceleration and rotation.

The original experiments (Cahn et al., 1997) were carried out with counter-propagating beams having identical circular polarizations, as shown in Figure 1. The $\boldsymbol{k}_1$ and $\boldsymbol{k}_2$ beams were independently controlled with acousto-optic modulators (AOMs). In the experiment, the $\boldsymbol{k}_1$ and $\boldsymbol{k}_2$ beams are simultaneously pulsed at time $t = 0$ for a duration of about 100 ns, followed by a second standing-wave pulse a time T later. Then, at a later time in the vicinity of $t = (\bar{N} + 1)T$ for integer $\bar{N}$, the resulting atomic grating is probed by switching on only the traveling wave along $\boldsymbol{k}_2$ and measuring the (complex) amplitude of the light wave scattering into the direction $\boldsymbol{k}_1$. The scattered wave is detected by beating it with an optical local-oscillator in a balanced heterodyne arrangement (see Figure 1). The local oscillator is derived from the light passing undiffracted through the AOM used to switch the $\boldsymbol{k}_1$ beam. During the experiment, the echo beat signal is further mixed down by a 220-MHz reference from the rf oscillator using a quadrature demodulator. The two outputs of this demodulator represent the real and imaginary parts of the scattered light field, where the real part is in phase with the $\boldsymbol{k}_1$ field (which is *not* on during detection), and the imaginary part is $\pi/2$ out of phase with $\boldsymbol{k}_1$. The phase of the signal is stabilized against mirror motion in between experiments (where an "experiment" consists of 90% trapping [sample preparation] time and 10% standing-wave pulse excitation and detection time), by phase-shifting the rf local oscillator.

1.2 Calculation of the Signal

We model the system as a two-level atom interacting with an off-resonant optical standing wave (Cahn et al., 1997; Dubetsky, 1997). We assume, first, that the detuning $\Delta = \omega - \omega_0$ is sufficiently large that the atom always remains in the ground state and that spontaneous emission can be neglected. Here ω is the laser frequency and ω_0 is the resonance frequency of the atom. The effects of spontaneous emission are discussed in Section 2. We also assume that, during the standing-wave pulse, the kinetic energy term in the Hamiltonian can be neglected (Raman–Nath approximation). This approximation is valid when $\omega_q \tau \ll 1$ and $\sqrt{\omega_q \chi}\, \tau \ll 1$ for two-photon Rabi frequency χ and standing-wave pulse duration τ.

For $\sigma^+ - \sigma^+$ or Lin–Lin illumination, we treat the separate transitions as independent two-level systems. For a single two-level system, we can adiabatically eliminate the excited state (Berman & Malinovsky, 2011) to obtain an effective Hamiltonian for the atomic ground state

$$H = \frac{\boldsymbol{p}^2}{2M} + V(\boldsymbol{r}, t), \tag{1}$$

where

$$V(\boldsymbol{r},t) = \hbar\chi(t)\cos(\boldsymbol{q}\cdot\boldsymbol{r}). \tag{2}$$

The time-dependent two-photon Rabi frequency is $\chi(t) = \Omega_0^2/2\Delta$, where $\Omega_0(t) = -\boldsymbol{\mu}\cdot\boldsymbol{E}(t)/\hbar$ is the on resonance Rabi frequency, $\boldsymbol{\mu}$ is a matrix element of the dipole moment operator, and $\boldsymbol{E}_0(t)$ is the electric field amplitude.

To calculate the signal, we first find the signal for a single atomic momentum state $\hbar\boldsymbol{k}_0$, and then sum that signal over all the initial momentum states. We therefore assume that just before the first standing-wave pulse, the atomic state is given by

$$\psi(\boldsymbol{r},0^-) = \mathrm{e}^{i\boldsymbol{k}_0\cdot\boldsymbol{r}}. \tag{3}$$

We will now apply the pulse to get

$$\psi(\boldsymbol{r},0^+) = \exp[iu_1\cos(\boldsymbol{q}\cdot\boldsymbol{r}) + i\boldsymbol{k}_0\cdot\boldsymbol{r}], \tag{4}$$

where $u_1 = \int_0^\tau \chi(t)\mathrm{d}t$ is a pulse area and τ is the duration of the pulse. Expanding Equation (4) in a Fourier series, we have

$$\psi(\boldsymbol{r},0^+) = \sum_n i^n J_n(u_1)\mathrm{e}^{i(n\boldsymbol{q}+\boldsymbol{k}_0)\cdot\boldsymbol{r}}, \tag{5}$$

which is a sum of plane waves with momenta differing by integer multiples of $\hbar\boldsymbol{q}$.

Each of the momentum states in Equation (5) oscillates at the frequency $\hbar(\boldsymbol{k}_0 + n\boldsymbol{q})^2/2M$, so the wave function at time t is given by

$$\psi(\boldsymbol{r},t) = \mathrm{e}^{i(\boldsymbol{k}_0\cdot\boldsymbol{r}-\omega_{k_0}t)}\sum_{n_1} i^{n_1}J_{n_1}(u_1)\mathrm{e}^{in_1\boldsymbol{q}\cdot(\boldsymbol{r}-\boldsymbol{v}_0t)}\mathrm{e}^{-in_1^2\omega_q t}, \tag{6}$$

where $\omega_{k_0} = \hbar k_0^2/2M$ and $\omega_q = \hbar q^2/2M$ is the two-photon recoil frequency.

As an aside, we compute the expected signal immediately after the first pulse. The atomic density after the pulse is given by $\rho(\boldsymbol{r},t) = \psi(\boldsymbol{r},t)\psi^*(\boldsymbol{r},t)$, and for a given initial velocity $\boldsymbol{v}_0$ is

$$\rho_{v_0}(\boldsymbol{r},t) = \sum_{n_1,n_1'} i^{n_1-n_1'}J_{n_1}(u_1)J_{n_1'}(u_1)\mathrm{e}^{i(n_1-n_1')\boldsymbol{q}\cdot(\boldsymbol{r}-\boldsymbol{v}_0t)}\mathrm{e}^{-(n_1^2-n_1'^2)\omega_q t}. \tag{7}$$

In the experiment, we apply a laser field along the direction $\boldsymbol{k}_2$ and observe a scattered field along the direction $\boldsymbol{k}_1$ (see Figure 1). This signal

is proportional to the spatial Fourier component of the atomic density involving $e^{iq\cdot r}$ for which $n_1 - n_1' = 1$:

$$\rho_{q,v_0}(\boldsymbol{r},t) = \sum_{n_1} iJ_{n_1}(u_1)J_{n_1+1}(u_1)e^{-iq\cdot v_0 t}e^{-i(2n_1-1)\omega_q t}. \tag{8}$$

The expression can be summed using the identity (Watson, 1980)

$$i^{\nu}J_{\nu}[2u\sin(\alpha/2)] = \sum_{l=-\infty}^{\infty} e^{i\nu\alpha/2}J_{l+\nu}(u)J_l(u)e^{il\alpha}, \tag{9}$$

resulting in a density

$$\rho_{q,v_0}(t) = J_1[2u_1\sin(\omega_q t)]e^{-iq\cdot v_0 t}. \tag{10}$$

After summing over the initial Maxwellian velocity distribution, we find

$$\rho_q(t) = J_1[2u_1\sin(\omega_q t)]\langle e^{-iq\cdot v_0 t}\rangle = J_1[2u_1\sin(\omega_q t)]e^{-(q\sigma_v t/2)^2}, \tag{11}$$

where σ_v is the e^{-1} width of the velocity distribution.

Figure 2 shows data (Cahn, 1997) and a theoretical fit based on Equation (11). In the experiment, a short standing-wave pulse made up of counter-propagating fields with wave vectors $\boldsymbol{k}_1$ and $\boldsymbol{k}_2$ is applied. Immediately after the pulse, a traveling wave is applied along $\boldsymbol{k}_2$, and the scattered signal along $\boldsymbol{k}_1$ is detected. A physical picture of the data shown in Figure 2 can be understood as follows. Before the pulse the atomic density is uniform. The effect of the standing-wave pulse is a momentum kick

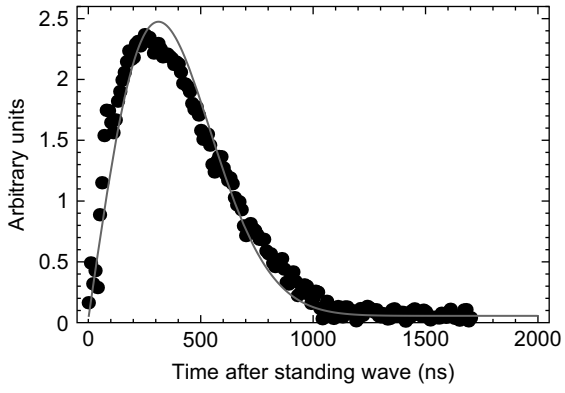

Figure 2 Doppler-broadened Kapitza-Dirac effect.

to the atoms in a direction toward the minima of the potential defined by the standing wave. Immediately after the pulse, there is no scattered signal, since the atoms have had no time to move from their initial position. With time, the atoms move toward the potential minima, creating a grating in atomic density, which scatters the light. Since there is a spread in initial velocities, the grating will wash out because of the fact that gratings produced by different velocity classes will dephase from one another on a time scale $t \sim d/\sigma_v$, where σ_v is the initial velocity spread and $d = \lambda/2$ is the period of the grating.

At time $t = T$, we apply a second pulse with area u_2. The result is that each atomic plane wave generated by the first pulse is split into a set of plane waves, and the wave function after the second pulse is given by

$$\psi(\boldsymbol{r},t) = \mathrm{e}^{i(\boldsymbol{k}_0\cdot\boldsymbol{r}-\omega_{k_0}t)}\sum_{n_1,n_2} i^{n_1+n_2}J_{n_1}(u_1)J_{n_2}(u_2) \times \mathrm{e}^{-in_1\boldsymbol{q}\cdot\boldsymbol{v}_0T}\mathrm{e}^{i(n_1+n_2)\boldsymbol{q}\cdot[\boldsymbol{r}-\boldsymbol{v}_0(t-T)]}\,\mathrm{e}^{-in_1^2\omega_qT}\mathrm{e}^{-i(n_1+n_2)^2\omega_q(t-T)}. \quad (12)$$

We find that the resulting density $\rho_{v_0}(\boldsymbol{r},t) \equiv \psi^*(\boldsymbol{r},t)\psi(\boldsymbol{r},t)$ is

$$\rho_{\boldsymbol{q},v_0}(\boldsymbol{r},t) = \sum_{n_1,n_1',n_2,n_2'} i^{n_1+n_1'+n_2+n_2'}J_{n_1}(u_1)J_{n_1'}(u_1)J_{n_2}(u_2)J_{n_2'}(u_2) \times \mathrm{e}^{-i(n_1-n_1')\boldsymbol{q}\cdot\boldsymbol{v}_0T}\mathrm{e}^{i[(n_1+n_2)-(n_1'+n_2')]\boldsymbol{q}\cdot[\boldsymbol{r}-\boldsymbol{v}_0(t-T)]} \times \mathrm{e}^{-i(n_1^2-n_1'^2)\omega_qT}\mathrm{e}^{-i[(n_1+n_2)^2-(n_1'+n_2')^2]\omega_q(t-T)}. \quad (13)$$

Since the experiment measures the scattering of the light field with wave-vector $\boldsymbol{k}_1$ into wave-vector $\boldsymbol{k}_2$, we are interested only in the $\mathrm{e}^{i\boldsymbol{q}\cdot\boldsymbol{r}}$ Fourier component of the atomic density. We therefore consider only the terms in Equation (13) for which $(n_1 + n_2) - (n_1' + n_2') = 1$. In addition, we define $\bar{N} \equiv n_1' - n_1$, and find

$$\rho_{\boldsymbol{q},v_0}(\boldsymbol{r},t) = \sum_{n_1,n_1',n_2,n_2'} i^{n_1+n_1'+n_2+n_2'}J_{n_1}(u_1)J_{n_1'}(u_1)J_{n_2}(u_2)J_{n_2'}(u_2) \times \mathrm{e}^{-i\boldsymbol{q}\cdot\boldsymbol{v}_0[t-(\bar{N}+1)T]}\mathrm{e}^{i(n_1+n_1')\bar{N}\omega_qT}\mathrm{e}^{-i[2(n_1+n_2)+1]\omega_q(t-T)}. \quad (14)$$

This expression, when averaged over initial velocities $\boldsymbol{v}_0$, will be equal to zero unless the Doppler phase, $\phi_D = \boldsymbol{q}\cdot\boldsymbol{v}_0[t-(\bar{N}+1)T] \approx 0$. Thus, for a given value of $\bar{N}$, no signal will be observed unless $|t - t_{\bar{N}}| < 1/q\sigma_v$, where $t_{\bar{N}} = (\bar{N}+1)T$ is the echo time. We now apply Equation (9) to Equation (14) twice to get

$$\rho_{\boldsymbol{q}}(t) = (-1)^{\bar{N}+1}J_{\bar{N}}[2u_1\sin(\omega_q\Delta t)]J_{\bar{N}+1}[2u_2\sin(\bar{N}\omega_qT+\omega_q\Delta t)]\langle\mathrm{e}^{-i\boldsymbol{q}\cdot\boldsymbol{v}_0t}\rangle, \quad (15)$$

where $\Delta t = t - t_{\text{echo}}$. This equation can be simplified further by replacing $\langle e^{-iq\cdot v_0 t}\rangle$ with $e^{-(q\sigma_v t/2)^2}$, and realizing that the velocity spread of the laser-cooled atoms is much larger than the recoil velocity, so that a signal will be observed only when $\omega_q \Delta t \ll 1$. With this approximation, we can write

$$\rho_q(t) \sim (\Delta t)^{\bar{N}} J_{\bar{N}+1}[2u_2 \sin(\bar{N}\omega_q T)]e^{-(q\sigma_v t/2)^2}, \tag{16}$$

Figures 3a and b show the echo signal as a function of Δt for $\bar{N} = 1$ and $\bar{N} = 2$, respectively. We see that for $\bar{N} = 1$, the signal is linear at the time $\Delta t = 0$, and for $\bar{N} = 2$, the signal is quadratic, which is consistent with Equation (16).

Figure 3c and d show the amplitude of the echo signal as a function of T, for $\bar{N} = 1$ and $\bar{N} = 2$, respectively. In this case, the signal is periodic with a period equal to $2\pi/\omega_q \sim 32.4\,\mu s$. We point out here that an accurate measurement of this periodicity would allow one to make an accurate determination of the recoil frequency, and hence $\hbar/M$. The precision $d\omega_q$ with which one can determine the recoil frequency is given approximately by $dT/T_{\max}$, where dT is the uncertainty in the time of the zeros of the signal and $T_{\max}$ is the maximum value of T that yields a significant signal. As will be discussed further in Section 2, a precision measurement of ω_q would allow a precise determination of the fine structure constant.

Since the development of the time-domain de Broglie wave interferometer discussed earlier, a number of extensions of the basic interferometer design have been carried out by various groups. At NYU, the theory has been extended to an arbitrary sequence of short pulses, and data have been taken for a three-pulse interferometer (Strekalov et al., 2002).

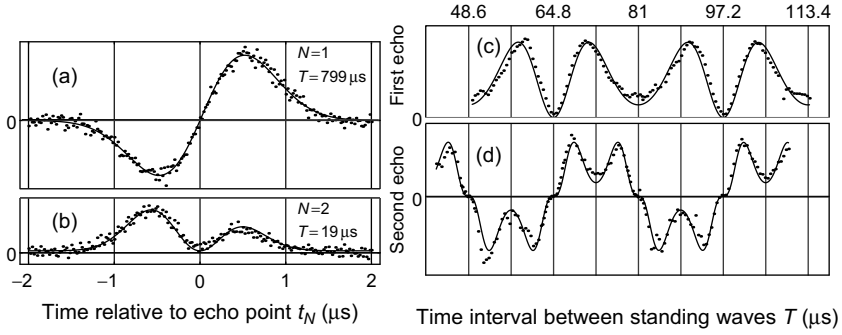

Figure 3 (a), (b) First two echoes as a function of Δt. (c), (d) First two echoes as a function of T. In all the plots, data are represented by solid dots. The solid curves in (a) and (b) are fits based on Equation (15). In (c) and (d) the solid curves are fits based on Equation (16).

At MIT, an interferometer of the type described here has been demonstrated with a Bose–Einstein condensate (BEC) (Gupta et al., 2002). At NIST in Gaithersburg, output coupling of BECs was also demonstrated using a standing-wave interferometer (Hagley et al., 1999). Other pioneering studies at MIT and Duke University have examined the role of atomic collisions on echo interferometers and developed techniques for phase-space imaging using coherent transient effects (Bacon et al., 1994; Forber et al., 1990; Thomas & Wang, 1995). Recent studies of the kicked-rotor in a magnetically guided trap for investigations of quantum dynamics and for applications to precision measurements have also used internal-state interferometers of this type (Tonyushkin & Prentiss, 2010; Tonyushkin et al., 2009a; Wu et al., 2005, 2009). At York University, the focus has been on precision measurements of atomic recoil (Beattie et al., 2009b). A complete understanding of mechanisms affecting the two-pulse interferometer was developed on the basis of analytical calculations and numerical simulations (Barrett et al., 2010; Cahn, 1997; Dubetsky, 1997) including effects such as spontaneous emission, magnetic sublevels, and standing-wave pulse parameters (rise time, duration, detuning, intensity). Systematic effects on the recoil frequency (angle between excitation beams, sample density, and index of refraction) have also been investigated. A multipulse interferometer was also developed, which has significant advantages for precision measurements (Beattie et al., 2009a). The theoretical description of this interferometer was developed using the wave function evolution approach discussed in Strekalov et al. (2002) and, separately, using the coherence function approach shown in Mandel (1979). The coherence function approach resulted in an understanding of the complete recovery of contrast in the interferometer using pulsed standing waves and the partial recovery of contrast using pulsed traveling waves and continuous wave light. The results of these studies of traveling-wave excitation were similar to the results of atomic beam experiments carried out by several pioneering groups (Chapman et al., 1995; Kokorowski et al., 2001; Pfau et al., 1994; Uys et al., 2005).

The outline of this chapter is as follows. Section 2 provides a physical description of the two-pulse interferometer described earlier and its application for precision measurements. It also presents an analysis of the effects of spontaneous emission and magnetic sublevels on the interferometer signal. The sensitivity of the interferometer to magnetic gradients and gravitational acceleration, g, is also discussed. This is followed by a description of the multipulse interferometer and a review of recent experimental results at the transit-time limit. Section 3 presents a modification to the techniques outlined earlier, in that instead of the first pulse, the atoms are cooled in an optical lattice potential, and at time $t = 0$, suddenly released. At time T a pulse of the optical lattice is applied and, at times close to $t = (\bar{N} + 1)T$, an echo is observed by the scattering of a

traveling wave. In addition, Section 3 discusses the behavior of the system if the applied pulse is of very long duration, in extreme violation of the Raman–Nath condition. Section 4 discusses frequency-domain techniques for measurements of atomic recoil and rotation. Section 5 includes a discussion of techniques for measurements of g using the two-pulse interferometer and presents recent results that show the potential for high-precision measurements. Section 6 presents techniques for measuring magnetic interactions using an internal state labeled interferometer that utilizes magnetic sublevels in a single ground state. Section 7 shows the suitability of the traditional two-pulse photon echo technique for precision measurements of atomic lifetimes. The article concludes with Section 8, which is a review of recent studies of superradiant emissions in laser-cooled atoms.

2. TIME-DOMAIN ATOM INTERFEROMETER EXPERIMENTS—ATOMIC RECOIL

2.1 Introduction

During the last 20 years, the field of precision measurements has focused on new determinations of fundamental constants. In particular, there has been renewed emphasis on independent measurements of the atomic fine structure constant, α, to test quantum electrodynamics (QED). Experiments based on the electron g-factor (Hanneke et al., 2008) and helium fine structure (Smiciklas & Shiner, 2010) rely on QED to define α. In contrast, precision measurements of α using atom interferometers (AIs) have relied on the following relationship (Taylor, 1994)

$$\alpha^2 = \left(\frac{2R_\infty}{c}\right)\left(\frac{m_p}{m_e}\right)\left(\frac{M}{m_e}\right)\left(\frac{h}{M}\right), \tag{17}$$

where R_∞ is the Rydberg constant, c is the speed of light, m_p (m_e) is the mass of the proton (electron), h is Planck's constant, and M is the mass of the test atom. Since R_∞ and the mass ratios have been measured with a precision greater than 0.1 parts per billion (ppb), AIs are well suited for precision measurements of α. Importantly, an AI-based measurement of α does not rely on QED and the precision in determining h/M is better than the precision with which h and M can be measured independently (Taylor, 1994).

AIs involving Raman transitions between hyperfine ground states have exploited the properties of laser-cooled atoms for a variety of experiments related to precision measurements and inertial sensing (Chiow et al., 2009; Dubetsky & Kasevich, 2006; Gupta et al., 2002; Lamporesi et al., 2008; McGuirk et al., 2002; Müller et al., 2010; Peters et al., 1999; Weiss et al.,

1993; Wicht et al., 2002). Recent AI-based work using Bloch oscillations in cold optical lattices (Cadoret et al., 2008) have also produced competitive measurements of α.

In this section we review, two time-domain echo-type AI techniques (Barrett et al., 2010; Beattie et al., 2009a,b, 2008; Cahn et al., 1997) that allow of precise measurements of the atomic recoil frequency, $\omega_q = \hbar q^2/2M$, where $\hbar q$ is the two-photon momentum transfer from counter-propagating laser fields. The different techniques for extracting ω_q are introduced briefly, followed by a more detailed discussion of signal formation.

2.1.1 Physical Description of the AI

The AI functions on the basis of phase modulation of the atomic wave function due to the interaction with standing-wave (sw) pulses. Although this phase modulation is directly connected to the recoil energy, the functional form of the signal has a complicated dependence on a number of mechanisms that we explore in the following subsections. These include the dynamic population of magnetic sublevels, phase shifts due to spontaneous and stimulated processes, excitation of multiple momentum states, and the spatial profile of the excitation beams. Recent work has successfully modeled the signal shape on the basis of analytical calculations as well as numerical simulations (Barrett et al., 2010; Beattie et al., 2008).

The AI uses a cold gas of rubidium atoms. The sample is excited by sw pulses that satisfy the Raman–Nath criterion and are far-detuned from the excited state. Each such pulse results in the diffraction of atoms into a superposition of momentum states separated by $\hbar q = 2\hbar k$ (as shown in Figure 4a), where $k = 2\pi/\lambda$ is the wavenumber of the traveling wave components of the sw. Each pulse transfers momenta in integer multiples of $\hbar q$, due to scattering of radiation between the two traveling-wave components of the sw field. After excitation, the sample evolves into a superposition of momentum states corresponding to the same internal ground state—which can have several magnetic sublevels.

The recoil phase of momentum state $|p = n\hbar q\rangle$ scales as $n^2\omega_q t$, where n is an integer denoting the number of two-photon transitions induced by the sw pulse. The Doppler phase of these states evolves as nqv_0t, where v_0 is the initial atomic velocity. The modulation of the wave function occurs on a timescale $\tau_q = \pi/\omega_q$ ($\sim$32 μs for ^{85}Rb). This occurs because atoms differing in velocity by the recoil velocity, $v_q = \hbar q/M$, are displaced relative to one another by one grating period ($\lambda/2$) in a time τ_q. This time scale should be compared to the coherence time, $\tau_{\text{coh}} \sim 2/q\sigma_v$, of the atomic density grating induced by the sw potential. Here, $\sigma_v = \sqrt{2k_B\mathcal{T}/M}$ is the e^{-1} width of the velocity distribution and $\mathcal{T}$ is the temperature of the sample. This is the time scale on which the temporal modulation of the wave

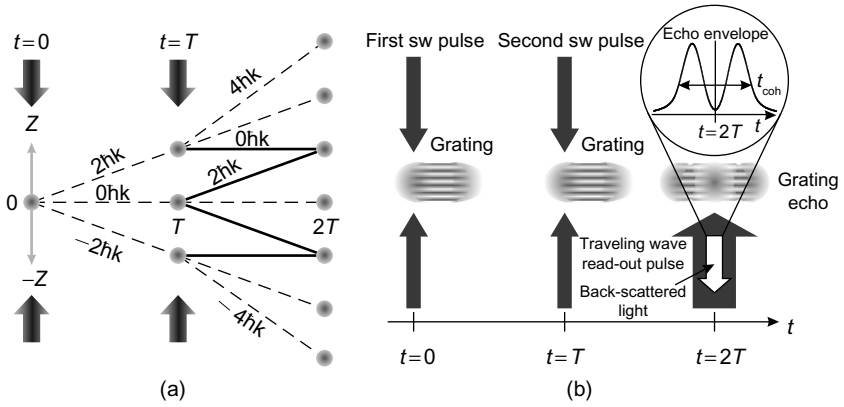

Figure 4 (a) Recoil diagram for the two-pulse AI. Center-of-mass momentum states are shown as dots. Standing-wave pulses are applied at $t = 0$ and $t = T$ to diffract the momentum states of the atom into multiples of the two-photon recoil momentum $2\hbar k$. Only the zeroth-order and the $\pm$ first-order diffractions from each sw pulse are drawn for simplicity. Two pairs of interfering momentum states are shown as solid lines. (b) Pulse timing diagram for the experiment. After each sw pulse, a modulation in atom density forms and then decays in a time τ_{coh} because of Doppler dephasing. At time $t = 2T$, the grating echo forms as a result of the interference between different momentum states. A traveling-wave read-out pulse coherently scatters light from the grating at this time. The intensity of this light is detected as the signal.

function decoheres because of Doppler dephasing from the finite velocity distribution of the sample.

For BEC conditions with $\mathcal{T} \sim 10^{-8}$ K, the dephasing time can be much longer than the modulation period of the wave function. In this case, the recoil modulation can be observed with a single sw pulse, as discussed in detail in Section 2.3.

The theoretical expression for the recoil signal in the two-pulse regime was originally derived in Cahn et al. (1997). The treatment in (Beattie et al., 2008) addressed the role of spontaneous emission (SE) on the recoil signal. A comprehensive study of effects on the two-pulse AI related to both stimulated and spontaneous processes between magnetic sublevels in the ground and excited states was carried out using numerical simulations in Barrett et al. (2010). An analytical model of the two-pulse AI including both SE and magnetic sublevels was also derived in this work. We discuss these issues in Section 2.4.

An alternative technique for measuring ω_q, described in Section 2.5, involves excitation with a third sw pulse applied at $t = T + \delta T$. One then observes the influence of this pulse on the echo at $t = 2T$. Figure 5 shows the timing diagrams for both the two-pulse and three-pulse AI techniques. In the absence of SE, the contrast at $t = 2T$ can be recovered when δT is

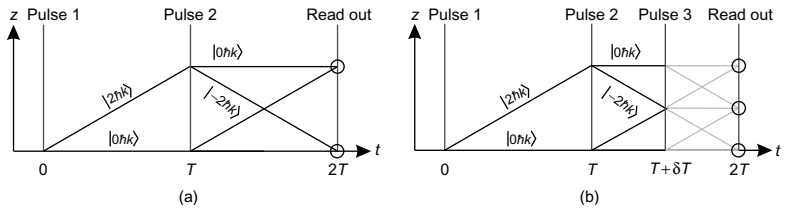

Figure 5 Recoil diagram for the two-pulse AI (a) and the three-pulse AI (b). The grating contrast at $t = 2T$ is measured by varying the pulse separation, T, in the two-pulse AI. In the case of the three-pulse AI, T is held fixed and the time of the third pulse, δT, is varied. The contrast exhibits a periodic revival when δT is an integer multiple of the recoil period, τ_q.

an integer multiple of τ_q, due to constructive interference of phase-shifted momentum states produced by the third pulse, as shown in Figure 5b. The basic signal shape produced by this AI can be described by a coherence function (Beattie et al., 2009b; Mandel, 1979)—a Fourier transform of the atomic momentum distribution produced by a sw pulse. A more detailed quantum mechanical calculation of the echo formation (Beattie et al., 2009a; Strekalov et al., 2002) predicts certain scaling laws for the fringe width as a function of the area of the third pulse which can be exploited to improve the precision of a measurement of ω_q.

In contrast, if the third pulse is a traveling wave, the quasi-periodic contrast cannot be fully recovered because of decoherence from SE. The contrast as a function of δT in this case can also be described using a coherence function, as in atomic beam experiments (Chapman et al., 1995; Kokorowski et al., 2001; Pfau et al., 1994; Uys et al., 2005) and in time-domain experiments in cold atoms (Beattie et al., 2009a).

2.2 Experimental Work

Although the timescale and precision associated with the recoil experiment should be limited only by the transit time of the atoms through the region of interaction, in practice it is necessary to eliminate the effects of decoherence due to atomic collisions and background light. Magnetic field gradients also cause amplitude oscillations that must be eliminated (Weel et al., 2006). A plot of the signal decay as a function of the pulse separation, T, is shown in shown in Figure 6a. The decrease in signal with T is mainly due to residual magnetic field gradients and the loss of atoms from the region of interaction defined by the excitation beams.

An interesting aspect of using the echo technique is that the Doppler phases accumulated by momentum states cancel at the echo times. As a result, the experiment does not rely on velocity selection. Although velocity selection is not required for the grating echo AI, sub-Doppler cooling

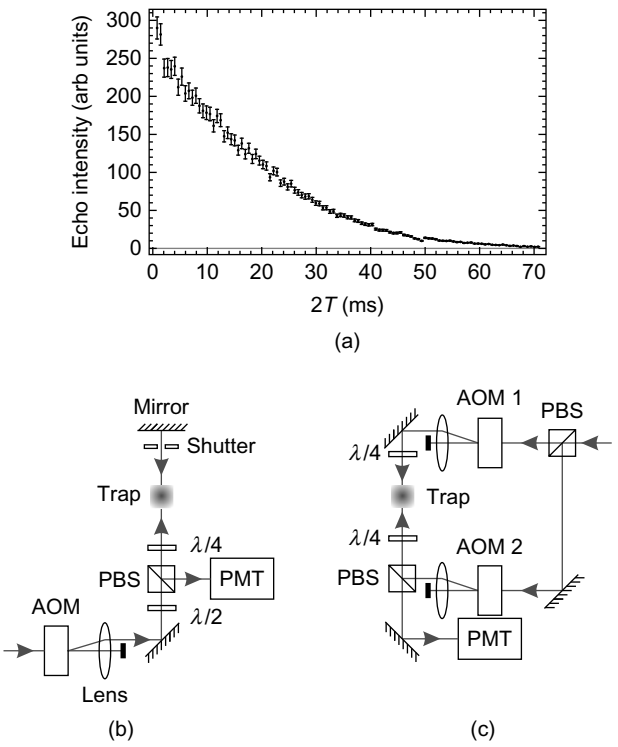

Figure 6 (a) Signal decay of the two-pulse AI as a function of pulse separation, T. The first pulse is held fixed while the second pulse and read-out pulse are moved out in integer units of the recoil period, τ_q, and twice the recoil period, respectively. The loss of signal is primarily due to atoms leaving the region of interaction. (b) Experimental setup used for the two-pulse recoil experiment and (c) for the three-pulse experiment.

of the sample is necessary to extend the transit time, which is the primary limitation for the timescale of the experiment.

Experiments involving the two-pulse technique (Beattie et al., 2008) were carried out in a stainless steel vacuum chamber. The light used for atom trapping and atom interferometry is derived from a Ti:Sapphire ring laser and from a semiconductor tapered amplifier seeded by light from the Ti:Sapphire laser. Approximately 10^8 ^{85}Rb atoms are loaded into a magneto-optical trap (MOT) in ∼200 ms. The temperature of the sample was typically ∼50 μK (Vorozcovs et al., 2005).

The excitation pulses for the AI are derived from a chain of acousto-optic modulators (AOMs) controlled by transistor-transistor logic (TTL) switches that ensure an extinction ratio for the radio frequency (RF) power of ∼40 dB. Pulsing a chain of AOMs ensures that excitation and read-out pulses have on/off contrast greater than $10^6 : 1$, thereby minimizing

decoherence due to background light. The last AOM in this chain operates at 250 MHz and is shown in Figure 6b. The diffracted beam from this AOM serves as the excitation beam. A beam diameter of ∼0.5 cm was used, which is comparable to the initial cloud diameter of ∼0.6 cm. The mirror shown at the top of Figure 6c is used to retro-reflect the traveling-wave pulses from the AOM and produce the sw excitation pulses used for the AI. A shutter with a closing time of ∼600 μs is used to block the retro-reflection at the time of the read-out pulse.

The grating contrast is detected using a read-out pulse that has the same polarization and detuning as the excitation pulses. The scattered light from the sample due to the read-out pulse is detected using a gated photomultiplier tube (PMT). Owing to jitter in the shutter closing time of ∼200 μs, the smallest pulse separation, T, for which the echo can be recorded using this technique is ∼1 ms. The grating contrast is determined by integrating the echo envelope over the signal duration of ∼2 μs.

For recent experiments with the three-pulse technique, a glass vacuum system was used. Here, the trap loads $\sim 10^9$ atoms in ∼300 ms. Both the MOT laser beams and the magnetic field gradient are switched off prior to the AI experiment. Three pairs of coils, one pair along each direction, are used to cancel residual magnetic fields and field gradients. These coils remain on continuously. Under these conditions, the magnetic field at the time of the echo experiment is canceled at the level of ∼1 mG over the volume of the trap. The AI excitation pulses are derived from two off-resonant, circularly polarized, traveling wave beams. They are overlapped at the location of the trap to form a sw along the vertical direction. The AI beams have a Gaussian intensity profile and are collimated to a diameter of ∼1 cm. Two separate AOMs operating at 250 MHz were used to generate counter-propagating traveling-wave pulses as shown in Figure 6c. This arrangement allowed the shutter to be eliminated so that the time separation between the standing-wave excitation pulses, T, could be reduced to a few microseconds.

2.3 One-Pulse Atom Interferometer

In order to fully understand the origin of the signal used in the experiments, a quantum theory of matter wave interference is essential. Such a theory is governed by the quantization of the atomic center-of-mass motion and is analogous to the diffraction of light in classical optics.

The simplest signal is presented first, namely the recoil signal produced by one sw pulse. In order to observe interference between momentum states after one pulse, the velocity distribution of the sample must be very narrow ($\sigma_v/v_q \ll 1$) such that the coherence of the sample is preserved much longer than the onset time of recoil modulation (τ_q). The calculation of the signal is then carried out in two stages. First, the Schrödinger equation is solved for the ground-state amplitude of the atomic wave

function using the two-level Hamiltonian for a sw laser field. The Hamiltonian assumes that the sw pulse is short (Raman–Nath regime) such that the motion of the atoms along the axis of the sw can be neglected during the interaction. It also assumes that the pulse is far off-resonance ($|\Delta| \gg \Omega_0, \gamma$) such that the excited state is not significantly populated. This leads to Kapitza-Dirac diffraction of the atomic wave function into a superposition of momentum states. Here, $\Delta \equiv \omega - \omega_0$ is the detuning of the laser frequency, ω, from the atomic resonance frequency, ω_0, $\Omega_0 \equiv \mu_{eg} E_0/\hbar$ is the Rabi frequency, μ_{eg} is a dipole matrix element, E_0 is the electric-field amplitude of each traveling-wave component of the sw, and $\gamma = \Gamma/2$, where Γ is the spontaneous emission rate.

In the second stage of the calculation, after the pulse has turned off, the atom is allowed to evolve in free space for a time t, which results in a modification of the phase of the ground-state amplitude. In an experiment involving a BEC, a traveling-wave read-out pulse with wavelength λ can be applied to the atomic sample and the back-scattered electric field can be detected as the signal (Gupta et al., 2002). The amplitude of the scattered field is proportional to the $\lambda/2$-periodic component of the atomic density modulation (the $2k = q$-Fourier harmonic) produced by the sw interaction. For a long read-out pulse, the scattered signal would exhibit temporal modulation proportional to the contrast of the atomic density distribution.

For a two-level atom, the Hamiltonian in the field-interaction representation is (Berman & Malinovsky, 2011)

$$\mathcal{H} = \hbar \begin{pmatrix} -\Delta - i\gamma & \Omega(\boldsymbol{r}) \\ \Omega(\boldsymbol{r}) & 0 \end{pmatrix}, \tag{18}$$

where $\Omega(\boldsymbol{r}) = \Omega_0 \cos(\boldsymbol{k} \cdot \boldsymbol{r})$ for a sw laser field. The energy is defined to be zero for the ground state and $-\hbar\Delta$ for the excited state. The $-i\hbar\gamma$ term is a phenomenological constant added to account for SE during the interaction, which gives rise to amplitude decay of the excited state. For the moment, the effects due to SE are ignored by setting $\gamma = 0$ in Equation (18). These effects are discussed in a later section.

The ground-state density produced after the interaction with one sw pulse is

$$\rho_g^{(1)}(\boldsymbol{r}, t) = \frac{1}{V} \sum_{\nu=-\infty}^{\infty} \chi_\nu^{(1)}(t) \mathrm{e}^{-i\nu \boldsymbol{q}\cdot\boldsymbol{r}}, \tag{19a}$$

$$\chi_\nu^{(1)}(t) = i^\nu \mathrm{e}^{i\nu \boldsymbol{q}\cdot\boldsymbol{v}_0(t-T_1)} \sum_n J_n(u_1) J_{n+\nu}(u_1) \mathrm{e}^{i\nu(2n+\nu)\omega_q(t-T_1)}. \tag{19b}$$

Here, $\chi_\nu^{(1)}(t)$ is the amplitude of the $\nu\boldsymbol{q}$-Fourier harmonic of the density distribution and the superscript (1) denotes that this is valid for one sw

pulse. The field scattered from the density grating is proportional to $\chi_1^{(1)}(t)$ and can be shown to be (Barrett et al., 2010)

$$E^{(1)}(t) \propto -J_1\big[2u_1 \sin \omega_q(t - T_1)\big], \tag{20}$$

where T_1 is the onset time of the pulse, ω_q is the recoil frequency and u_1 is the pulse area, which, for a pulse duration of τ_1, is given by

$$u_1 = \frac{\Omega_0^2}{2\Delta}\tau_1. \tag{21}$$

Figure 7 shows the atomic density (obtained using Equation [19a]) and corresponding scattered field amplitude (obtained using Equation [20]) for two different pulse areas.

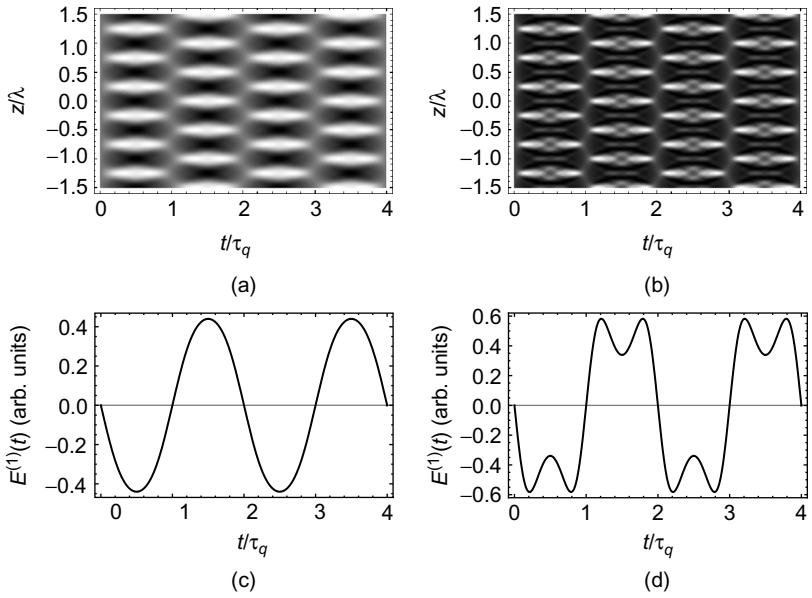

Figure 7 Density distribution, $\rho_g^{(1)}(z, t)$, and corresponding back-scattered electric field amplitude, $E^{(1)}(t)$, for an atomic sample after the interaction with a weak sw pulse (a, c) and a strong sw pulse (b, d). In plots (a) and (b), z is the distance along the sw field. Dark portions correspond to low density while light portions correspond to high density. $\rho_g^{(1)}(z, t)$ shows spatial modulation that is periodic at integer multiples of $\lambda/2$, and shows temporal modulation at integer multiples of $2\omega_q$ as the pulse area increases. Equation (19a) was used to produce plots (a) and (b) with pulse area $u_1 = 0.5$ and 1.5, respectively. In plots (c) and (d), Equation (20) was used with the same respective pulse areas. The zeroes in the contrast of the density modulation correspond to the zeroes in $E^{(1)}(t)$.

The recoil signal in the one-pulse regime is the intensity of the scattered field, which is proportional to the square of Equation (20): $s^{(1)}(t) \propto |E^{(1)}(t)|^2$.

2.4 Two-Pulse Atom Interferometer

Here, the two-pulse atom interferometer is discussed, along with the qualitatively new features that arise in this case. When the velocity dispersion of the sample is large, that is, $\sigma_v/v_q > 1$, the grating in Equation (19a) is washed out. By subjecting the sample to a second sw pulse, the grating is reformed at a later time. The grating echoes occur only at times where the Doppler phase cancels, (as shown in Figure 8)

$$t^{(2)}_{\text{echo}} = T_2 + \bar{N}(T_2 - T_1) = (\bar{N} + 1)T, \tag{22}$$

for pulse onset times of $T_1 = 0$ and $T_2 = T$.

The first echo time where all momentum states interfere is $t^{(2)}_{\text{echo}} = 2T$, corresponding to $\bar{N} = 1$, which will be the focus of most of this work. The scattered field amplitude in the vicinity of the $\bar{N}$th- order echo time is

$$\begin{aligned} E^{(2)}_{\bar{N}}(\Delta t; T) \propto (-1)^{\bar{N}+1} \mathrm{e}^{-(\Delta t/\tau_{\text{coh}})^2} J_{\bar{N}}\big(2u_1 \sin(\omega_q \Delta t)\big) \\ \times J_{\bar{N}+1}\big(2u_2 \sin[\omega_q(\Delta t + \bar{N}T)]\big), \end{aligned} \tag{23}$$

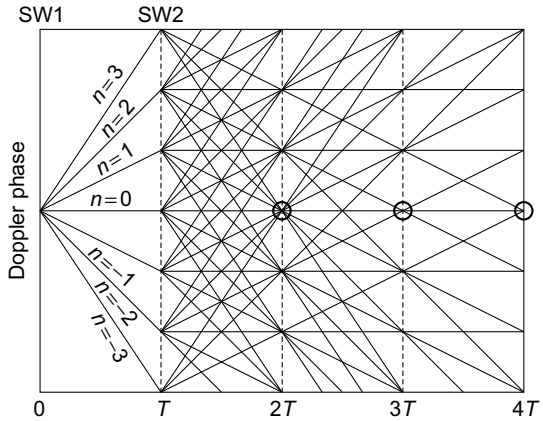

Figure 8 Two-pulse recoil diagram: Doppler phase as a function of time for momentum states $|n\hbar q\rangle$. Only $n = -3, \ldots, 3$ are shown for simplicity. The first sw pulse (SW1) is applied at $t = 0$, while the second (SW2) is applied at $t = T$. Echo times (given by Equation [22]) are marked by circles. The number of crossings at each echo time is proportional to the contrast of the $\lambda/2$-periodic density grating formed at those times.

where $\Delta t = t - t^{(2)}_{\text{echo}}$, with $t^{(2)}_{\text{echo}}$ given by Equation (22). From this expression, it is clear that the scattered field amplitude is periodic at multiples of the recoil frequency as a function of the pulse separation T. It is interesting to note that, for the $\bar{N}$th-order echo, the scattered field amplitude changes at frequency $\bar{N}\omega_q$, which is advantageous for a precision measurement of ω_q. However, the maximum contrast of the $\bar{N}$th-order echo is reduced by a factor of $\sim J_{\bar{N}-1}(2u_1)/J_{\bar{N}}(2u_1) \sim (2u_1)^{-1}$ relative to the $(\bar{N}-1)$th order echo, which manifests as a loss in the signal to noise ratio in the experiment.

In the experiment, the measurable quantity is the relative contrast of the atomic density grating in the vicinity of the echo. This quantity—defined as the recoil signal—is obtained by integrating the scattered field intensity over the duration of the echo, which can be written as

$$s^{(2)}_{\bar{N}}(T) \propto J^2_{\bar{N}+1}\big(2u_2 \sin(\bar{N}\omega_q T)\big), \tag{24}$$

where the superscript (2) denotes the number of pulses used to produce the signal and the subscript $\bar{N}$ denotes the order of the echo.

2.4.1 Effects due to Spontaneous Emission

Spontaneous emission during the sw interaction strongly affects the recoil signal (Beattie et al., 2008). Taking it into account, the expression for the scattered field in the case of both one and two pulses is modified as follows:

$$E^{(1)}(t) \propto -J_1\left(2u_1\sqrt{\sin(\phi_1^{(1)}+\theta)\sin(\phi_1^{(1)}-\theta)}\right)\left(\frac{\sin(\phi_1^{(1)}-\theta)}{\sin(\phi_1^{(1)}+\theta)}\right)^{1/2}, \tag{25a}$$

$$\begin{aligned} E^{(2)}_{\bar{N}}(\Delta t;T) \propto{}& (-1)^{\bar{N}+1} e^{-(\Delta t/\tau_{\text{coh}})^2} \\ &\times J_{\bar{N}}\left(2u_1\sqrt{\sin(\phi_1^{(2)}+\theta)\sin(\phi_1^{(2)}-\theta)}\right) \\ &\times J_{\bar{N}+1}\left(2u_2\sqrt{\sin(\phi_2^{(2)}+\theta)\sin(\phi_2^{(2)}-\theta)}\right) \\ &\times \left(\frac{\sin(\phi_1^{(2)}+\theta)}{\sin(\phi_1^{(2)}-\theta)}\right)^{\bar{N}/2}\left(\frac{\sin(\phi_2^{(2)}-\theta)}{\sin(\phi_2^{(2)}+\theta)}\right)^{(\bar{N}+1)/2}. \end{aligned} \tag{25b}$$

Here, the recoil phases for each pulse are defined as

$$\phi_1^{(1)} = \omega_q(t - T_1), \tag{26a}$$

$$\phi_1^{(2)} = \omega_q[t - T_2 - \bar{N}(T_2 - T_1)] = \omega_q \Delta t, \tag{26b}$$

$$\phi_2^{(2)} = \omega_q(t - T_2) = \omega_q[\Delta t + \bar{N}(T_2 - T_1)], \tag{26c}$$

where T_j is the onset time of pulse j, u_j is the magnitude of the complex pulse area, $\Theta_j = u_j e^{i\theta}$, given by

$$u_j = \frac{\Omega_0^2 \tau_j}{2\Delta}\left[1 + \left(\frac{\Gamma}{2\Delta}\right)^2\right]^{-1/2}, \tag{27}$$

and θ is a phase that represents the degree to which SE contributes to the signal:

$$\theta = \tan^{-1}\left(-\frac{\Gamma}{2\Delta}\right). \tag{28}$$

There are two main features that are observed when SE is present. First, within a single period, the signal develops an *asymmetry* about the zeroes. Second, there is a temporal shift of the zeroes toward earlier times relative to the zeroes expected without SE. Both of these features are best demonstrated when the pulse area is large—causing the double-peak structure within each period of the recoil signal. This is illustrated in Figure 9a for the one-pulse case, and has been observed experimentally in the two-pulse case as shown in Figure 9b.

In the absence of SE the signal develops multiple peaks within each period for large pulse areas (compare Figure 7c to Figure 7d). This

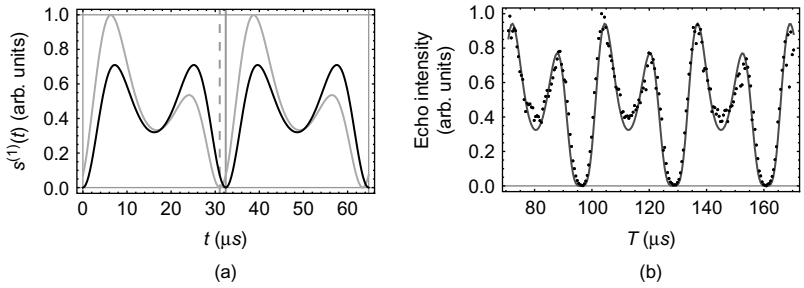

Figure 9 (a) Comparison of recoil curves (scattered field intensity as a function of time after the sw pulse) predicted by the one-pulse theory (square of Equation [25a]) with and without SE. The black curve corresponds to a SE-free system ($\Gamma = 0 \rightarrow \theta = 0$), while the gray curve corresponds to a system where SE is present ($\Gamma = \Gamma_N \rightarrow \theta = -0.133$ rad). The solid vertical line shows the first zero in the signal after $t = 0$ in the absence of SE, while the dashed vertical line shows the zeroes shift by a temporal amount $\delta t = \theta/\omega_q$ in the presence of SE. Pulse parameters: $\Delta = 7.5\,\Gamma_N$; $\Omega_0 = 1.5\,\Gamma_N$; $\tau_1 = 250$ ns; pulse area $u_1 \sim 1.43$. (b) Data from the two-pulse recoil experiment fitted to the square of Equation (25b)—solid line. The data exhibit a similar asymmetric shape to that predicted by the theory. Pulse parameters: detuning $\Delta \sim 50$ MHz; intensity $I \sim 50$ mW/cm^2; pulse durations $\tau_1 = 300$ ns, $\tau_2 = 70$ ns; circular polarization.

structure is due to the interference of higher order momentum states which become more populated as the pulse area increases. In the absence of any phase shifts of the individual harmonics, the shape of the recoil signal ($s^{(1)}(t) = |E^{(1)}(t)|^2$) is symmetric (black curve in Figure 9a).

On the other hand, when SE is present the phases of the individual harmonics comprising the signal are shifted by a phase $\phi_n^{(1)} \approx |n|\theta - n\pi/2$ (Barrett et al., 2010), as a result of the decay of the excited state into the ground state. Here, n is an integer denoting the momentum states that are interfering ($\langle n\hbar q \,|\, (n+1)\hbar q\rangle$) to produce each harmonic of the signal. Since the signal is a coherent sum over all the harmonics, it exhibits more constructive interference on one side of its zeroes than the other, giving rise to an asymmetry in the peak amplitude within each recoil period. It also results in an overall temporal shift of the waveform equal to $\delta t = \theta/\omega_q$.

2.4.2 Effects due to Magnetic Sublevels

In the experiment ^{85}Rb is used, which is a multilevel atom. If only the $F = 3 \rightarrow F' = 4$ transition is considered, there are $2F + 1 = 7$ ground-state magnetic sublevels and nine excited state sublevels. These energetically degenerate sublevels have a significant effect on the response of the AI.

The coupling strength between states $|g\rangle = |n_g J_g m_g\rangle$ and $|e\rangle = |n_e J_e m_e\rangle$ is determined by the dipole matrix element

$$\mu_{eg} = -e\,\langle e \,|\, \hat{\epsilon}_{q_L} \cdot \boldsymbol{r} \,|g\rangle = -e\langle n_e J_e \| r \| n_g J_g\rangle C^{J_g\ 1\ J_e}_{m_g\ q_L\ m_e}, \tag{29}$$

where n_g, n_e are the principal quantum numbers, J_g, J_e are the total angular momenta, and m_g, m_e are the magnetic sublevels of the ground and excited states, respectively. In our case, $J_g = F = 3$ and $J_e = F' = 4$. The unit vector $\hat{\epsilon}_{q_L}$ represents the polarization of the laser field. Linear and circular polarization states are denoted by q_L. Here, $q_L = 0$ for linearly polarized light along the quantization axis, $\hat{z}$ ($\boldsymbol{k} \parallel \hat{z}$), and $q_L = \pm 1$ for $\sigma^{\pm}$ polarizations in the xy-plane ($\boldsymbol{k} \perp \hat{z}$). The factor $\langle n_e J_e \| r \| n_g J_g\rangle$ in Equation (29) is the reduced matrix element associated with the radial part of the wave functions—the magnitude of which is unimportant for this treatment and will be absorbed into the Rabi frequency, $\Omega_0 = \mu_{eg} E_0/\hbar$. The factor $C^{J_g\ 1\ J_e}_{m_g\ q_L\ m_e}$ is the Clebsch-Gordan coefficient, which describes how strongly two states are coupled by the photon and depends on the particular transition. We are concerned only with electric dipole transitions that obey the selection rules: $J_e = J_g + 1$ and $m_e = m_g + q_L$.

From Equation (29), it is apparent that each degenerate m-level interacts with a sw pulse (of a given polarization) with a different coupling strength—which is proportional to the Rabi frequency for each transition: $C^{J_g\ 1\ J_e}_{m_g\ q_L\ m_e}\,\Omega_0$. In the experiment, this differential coupling causes the

population of the m-levels to become unbalanced after the interaction with the sw pulse (optical pumping). The degree of the imbalance is determined by Ω_0, Δ, and the pulse durations. In the analytical treatment that follows, optical pumping is not taken into account. We assume that the population of each m-level remains constant during the sw pulses. However, optical pumping effects can be taken into account using numerical simulations of the AI, which will be discussed later.

The area of a given sw pulse, denoted by index j, is given by

$$u_j^{(m_g)} = \frac{\Omega_0^2 \tau_j}{2\Delta}\left[1+\left(\frac{\Gamma}{2\Delta}\right)^2\right]^{-1/2}\left(C^{J_g\ 1\ J_e}_{m_g\ q_L\ m_e}\right)^2. \tag{30}$$

For the first-order echo of the two-pulse recoil signal ($\bar{N}=1$), the total scattered field amplitude is a sum over the fields scattered by each state $|J_g\, m_g\rangle$ (Barrett et al., 2010)

$$\begin{aligned} E_1^{(2)}(\Delta t;T) \propto e^{-(\Delta t/\tau_{coh})^2}&\left(\frac{\sin(\phi_1^{(2)}+\theta)}{\sin(\phi_1^{(2)}-\theta)}\right)^{1/2}\left(\frac{\sin(\phi_2^{(2)}-\theta)}{\sin(\phi_2^{(2)}+\theta)}\right)\\ &\times\sum_{m_g}\left(C^{J_g\ 1\ J_e}_{m_g\ q_L\ m_e}\right)^2 J_1\left(2u_1^{(m_g)}\sqrt{\sin(\phi_1^{(2)}+\theta)\sin(\phi_1^{(2)}-\theta)}\right)\\ &\times J_2\left(2u_2^{(m_g)}\sqrt{\sin(\phi_2^{(2)}+\theta)\sin(\phi_2^{(2)}-\theta)}\right), \end{aligned} \tag{31}$$

where the $\phi_j^{(2)}$ are recoil phases given by Eqs. (26b) and (26c). The extra factor of $\left(C^{J_g\ 1\ J_e}_{m_g\ q_L\ m_e}\right)^2$ in Eq. (31) arises because of the coupling of states $|J_g\, m_g\rangle$ and $|J_e\, m_e\rangle$ by the traveling-wave read-out pulse (assuming that the scattered field has the same polarization as the read-out pulse).

The form of Equation (31) allows for interference between scattered fields from each m-level. This additional interference from magnetic sublevels strongly affects the shape of the recoil signal. Figure 10a shows a comparison of two-pulse recoil signals predicted by the simple two-level theory (square of Equation [25b]) and the theory including multiple sublevels (square of Equation [31]). The two-level theory predicts extra zeroes in the signal shape that are not observed experimentally. In contrast, for the same set of pulse parameters, the multilevel theory correctly predicts that these extra zeroes should not be present. Their absence is due to the interference of back-scattered light from each magnetic sublevel.

Indeed, as Figure 10b shows, data from the two-pulse recoil experiment strongly support the multilevel model, described by Equation (31). In particular, the multilevel theory successfully models the asymmetry

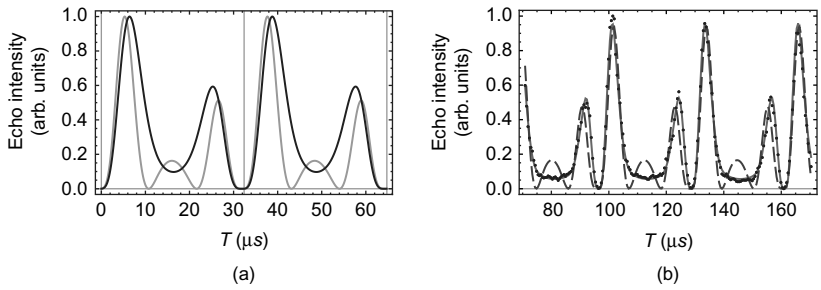

Figure 10 (a) Two-pulse recoil curves predicted by the two-level theory (square of Equation [25b]—gray curve) and the theory including magnetic sublevels (square of Equation [31]—black curve). The *m*-level populations were assumed to be equally distributed among the seven levels of the $J_g = 3$ ground state of ^{85}Rb. Pulse parameters: $\Delta = 10\,\Gamma_N$; $\Omega_0 = 2.5\,\Gamma_N$; $\Gamma = \Gamma_N$, $\tau_2 = 250$ ns. (b) Data from the two-pulse recoil experiment. Data are fitted to the two-level expression (square of Equation [25b]—dashed line), and the multilevel expression (square of Equation [31]—solid line). Pulse parameters: detuning $\Delta \sim 50$ MHz; intensity $I \sim 50$ mW/cm^2; polarization state $|q_L| = 1$; first pulse durations $\tau_1 = 300$ ns, $\tau_2 = 98$ ns.

and the broad valleys between zeroes that occur as the area of the second pulse is increased. Fits using the multilevel theory show a factor of $\sim$10 improvement in the χ^2/dof compared to that of the two-level theory, which corresponds to a factor of $\sim$3 improvement in the relative uncertainty of the recoil frequency. Thus, the multilevel model is necessary for precision measurements of ω_q using the two-pulse technique.

2.4.3 Spatial Profile

Another complication in modeling the AI is that magnetic sublevels and the spatial intensity profile of the excitation beams can be shown to produce similar effects on the signal shape. For the data presented earlier, the beam diameter ($\sim$1 cm) was larger than the diameter of the atomic cloud ($\sim$0.6 cm). Under these conditions, magnetic sublevels played the dominant role on the response of the AI. However, when the beam diameter is comparable to the size of the atomic cloud, these effects are indistinguishable.

Figure 11 shows a typical measurement of ω_q using the two-pulse technique. The echo intensity is recorded over two widely separated periods. The fit to the data shown in both plots is based on a phenomenological treatment including the effects due to SE and the spatial profile of excitation beams (Beattie et al., 2008) and gives an error for ω_q of $\sim$3 parts per million (ppm). This is a factor of $\sim$3 more precise than the fits using models without accounting for the spatial profile.

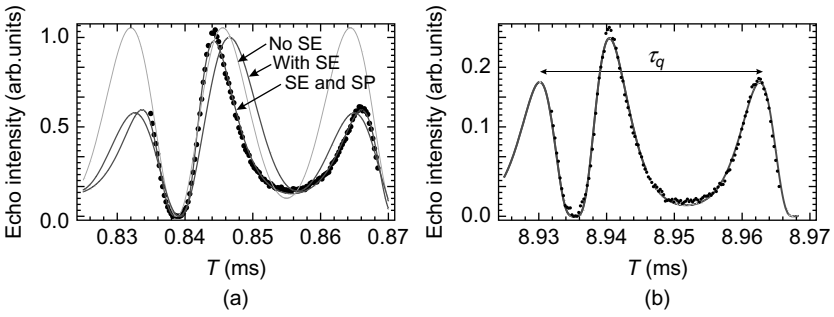

Figure 11 Grating contrast as a function of T for the two-pulse experiment shown at (a) $T \sim 1$ ms and (b) $T \sim 9$ ms. Part (a) shows three fits to the data, one based on the theory of echo formation ignoring effects due to SE (labeled "No SE"), one including SE (labeled "With SE"), and one based on a phenomenological treatment including both SE and the spatial profile of excitation beams (labeled "SE and SP"). Part (b) shows only the fit based on the phenomenological model. This fit gave a single measurement of ω_q precise to ~3 ppm.

In either case of small or large beam diameter, the importance of including both SE and magnetic sublevels/spatial profile in the model of the signal is quite significant for precision measurements.

2.4.4 Effects due to B-Field Gradients and Gravity

The effect of a constant acceleration on the interferometer manifests itself as a phase shift of the atomic grating, and therefore of the back-scattered electric field. Here, the modification of the scattered field amplitude due a constant force is presented. Two physical examples are considered: the force due to gravity and the force on the atom due to the presence of a uniform magnetic field gradient (Weel et al., 2006). Both of these forces can be written in the form $\hat{U}(z) = -\hat{\mathcal{M}}z$, where $\hat{\mathcal{M}}$ is an operator that commutes with both the position (z) and momentum (p) operators, and acts on the basis states $|F\, m_{\mathrm{F}}\rangle$. In the case of gravity, $\hat{\mathcal{M}} = \mathcal{F}\hat{I}$, with $\mathcal{F} = -Mg$ and identity matrix $\hat{I}$ since gravity acts equally on all magnetic sublevels. In the case of a magnetic field gradient, the potential is

$$\hat{U}(z) = -\boldsymbol{\mu} \cdot \boldsymbol{B}(z) = -g_{\mathrm{F}}\mu_{\mathrm{B}} G \frac{\hat{F}_z}{\hbar} z, \tag{32}$$

where g_{F} is the Landé g-factor, μ_{B} is the Bohr magneton, and $\boldsymbol{B}(z) = Gz$, where $G = \partial B/\partial z$ is a uniform magnetic field gradient along z, and $\hat{F}_z$ is the projection operator for total angular momentum, $\boldsymbol{F}$. In this case, $\hat{\mathcal{M}} = \mathcal{F}\hat{F}_z/\hbar$ and $\mathcal{F} = g_{\mathrm{F}}\mu_{\mathrm{B}}G$.

The total scattered field from all magnetic sublevels in the presence of a gradient G can be shown to be

$$E^{(2)}_{\bar{N},G}(\Delta t;T) = E^{(2)}_{\bar{N}}(\Delta t;T)\sum_{m_F}|\alpha_{m_F}|^2 e^{im_F\phi^{(2)}_G}, \tag{33}$$

where $E^{(2)}_{\bar{N}}$ is given by Equation (23) and the phase due to the gradient is

$$\phi^{(2)}_G(\Delta t;T) = \frac{qg_F\mu_B G}{2M}\left[\bar{N}(\bar{N}+1)T^2 + 2(\bar{N}+1)\Delta tT + \Delta t^2\right]. \tag{34}$$

From Equation (33), it is clear that the scattered field amplitude from state $|F\,m_F\rangle$ exhibits phase modulation as a function of the pulse spacing, T, at a frequency $m_F\omega^{(2)}_G(T)$ due to the presence of the gradient, where $\omega^{(2)}_G(T) = \partial\phi^{(2)}_G/\partial T$. This frequency depends linearly on the value of T (since the phase scales as T^2) and the magnetic quantum number, m_F. For an arbitrary set of m-level populations, $\{|\alpha_{m_F}|^2\}$, the total scattered field contains all the allowed harmonics of frequency $\omega^{(2)}_G(T)$. If more than one sublevel is populated, this effect can be detected in the signal intensity ($|E^{(2)}_{\bar{N},G}(t)|^2$), since interference between differentially oscillating sublevels would manifest as an amplitude modulation. However, if the system is optically pumping into a single sublevel, the modulation only affects the phase of the electric field—which cannot be observed using intensity detection. Instead, one can use a balanced heterodyne detector to measure the in-phase and in-quadrature components of the electric field amplitude to obtain the phase.

Taking into account the phase evolution of the wave function due to gravity, the scattered field can be shown to be

$$E^{(2)}_{\bar{N},g}(\Delta t;T) = E^{(2)}_{\bar{N}}(\Delta t;T)e^{i\phi^{(2)}_g}, \tag{35}$$

where $\phi^{(2)}_g(T) \sim -qg\bar{N}(\bar{N}+1)T^2/2$. Since gravity acts equally on all states, its effect is a modification of the phase of the density grating. This phase is then imprinted on the electric field scattered by the grating from the read-out pulse and cannot be detected from the intensity of the scattered light.

If the system is optically pumped into a single magnetic sublevel, other than $m_F = 0$, then a magnetic field gradient will affect only the phase of the scattered electric field in the same manner as gravity. Since both forces affect the phase of the scattered field in a similar manner, some care must be taken to isolate one effect or the other in an experiment. By performing the echo experiment in the horizontal direction, for example, one can eliminate the effect of gravity and isolate the effect of a magnetic field gradient. Similarly, by performing the experiment along the vertical direction

and canceling field gradients along all other directions, or by optically pumping into the $m_F = 0$ state, it is possible to eliminate the effect of B-field gradients in order to isolate the acceleration due to gravity.

The scale of these two physical mechanisms is also quite different. The force due to gravity on a ^{85}Rb atom is $\mathcal{F}_g \sim 1.4 \times 10^{-24}$ N. To achieve this same force with a B-field gradient, an atom in the $|F = 3, m_F = 3\rangle$ state would have to be exposed to a gradient of $G \sim 15$ Gauss/cm. In the lab, gradients as small as $G \sim 10^{-5}$ Gauss/cm can be applied to the atoms. Experimental timescales of $2T \sim 60$ ms have been achieved in a glass vacuum chamber with gradients at this level. At a pulse separation of $T \sim 30$ ms, amplitude modulation of the grating contrast due to a gradient of this size oscillates at a frequency of $m_F \omega_G^{(2)}(T) \sim 1$ Hz for $m_F = 3$ and $\bar{N} = 1$.

Figure 12 shows the recoil signal decay in the presence of a magnetic field gradient. The signal is modulated by the phase, $m_F \phi_G(T)$, for each sublevel $|F\, m_F\rangle$. By fitting the data to a model based on Equation (33), we measure the gradient to be $G = (23.9 \pm 0.09) \times 10^{-3}$ Gauss/cm, which is within a factor of two of the estimate of the applied gradient: $G \sim 0.05$ Gauss/cm.

Related studies of the effects of magnetic gradients involving guided atom interferometers are described in Wu et al. (2005).

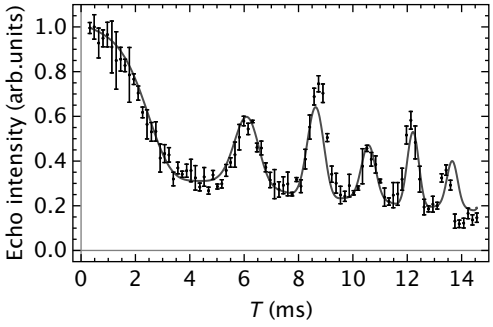

Figure 12 Data showing the effect of a magnetic field gradient on the recoil signal decay. Here, a gradient is applied to the atomic sample during the time of the experiment. The pulse separation, T, is varied in integer multiples of the recoil period, τ_q, so as to avoid any modulation due to recoil. The echo intensity is recorded at the first-order echo time, $t_{\text{echo}}^{(1)} = 2T$. Error bars represent the standard deviation of a set of three measurements of the echo intensity at the same T. The signal is modulated by the phase, $m_F \phi_G(T)$, for each sublevel $|F\, m_F\rangle$. The data are fitted to the function: $A[\alpha_0^2 + (\alpha_1 \cos \omega_G T + \alpha_2 \cos 2\omega_G T + \alpha_3 \cos 3\omega_G T)^2]e^{-T/\tau}$, shown as the solid line. From the fit we extract the gradient to be $G = (23.86 \pm 0.09) \times 10^{-3}$ Gauss/cm. The m-level populations are also measured to ~1% as $|\alpha_{m_F}|^2 = \{0.51, 0.46, 0.01, 0.02\}$, from $m_F = 0$ on the left to $m_F = 3$ on the right.

2.5 Multi-pulse atom interferometer

For the purposes of a precision measurement of ω_q, the two-pulse technique has one significant drawback: the signal exhibits a complicated, asymmetric shape as a function of T due to the different effects discussed earlier. A different technique for measuring ω_q with this interferometer—which makes use of multiple sw pulses—eliminates this difficulty.

It is relatively straightforward to generalize the expression of the scattered field for two sw pulses (Equation [23]) to N-pulses by applying a succession of phase gratings to the ground-state wave function (Beattie et al., 2009a; Strekalov et al., 2002). Work related to quantum kicked-rotors, which also use multiple-pulse AIs (Tonyushkin & Prentiss, 2009; Tonyushkin et al., 2009b; Wu et al., 2009), have also demonstrated sensitivity to atomic recoil.

Assuming that the jth pulse has a duration τ_j, complex pulse area $\Theta_j = u_j e^{i\theta}$ (where u_j and θ are given by Equations [27] and [28], respectively), and onset time $T_j > T_{j-1}$, followed by a period of free evolution $T_{j+1} - T_j$ before the $(j+1)$th pulse, the velocity averaged atomic density can be expressed as

$$\langle \rho_g^{(\boldsymbol{l})}(\boldsymbol{r}, t; \boldsymbol{T}) \rangle = \frac{1}{V} \sum_{l_N} \chi_{l_N}^{(\boldsymbol{l})}(t; \boldsymbol{T}) e^{-i l_N \boldsymbol{q} \cdot \boldsymbol{r}}, \tag{36}$$

where $\chi_{l_N}^{(\boldsymbol{l})}(t; \boldsymbol{T})$ is the amplitude of the $(l_N \boldsymbol{q})$-Fourier harmonic of the density distribution. Here, N is the number of pulses, $\boldsymbol{l} = \{l_1, l_2, \ldots, l_N\}$ denotes the set of interfering momentum states after the pulse sequence, and $\boldsymbol{T} = \{T_1, T_2, \ldots, T_N\}$ is the set of pulse onset times. The amplitude of each spatial component of the density is

$$\begin{aligned} \chi_{l_N}^{(\boldsymbol{l})}(t; \boldsymbol{T}) = - \sum_{l_1, \ldots, l_{N-1}} & e^{-\left[l_N \left(t - t_{\text{echo}}^{(\boldsymbol{l}, \boldsymbol{T})}\right)/\tau_{\text{coh}}\right]^2} \\ & \times \prod_{j=1}^{N} J_{(l_j - l_{j-1})}(w_j) \left(\frac{\sin(\phi_j - \theta)}{\sin(\phi_j + \theta)} \right)^{(l_j - l_{j-1})/2}, \end{aligned} \tag{37}$$

where $\tau_{\text{coh}} = 2/q\sigma_v$ and ϕ_j is the recoil phase due to pulse j:

$$\phi_j = \omega_q \sum_{k=j}^{N} l_k (T_{k+1} - T_k), \tag{38a}$$

$$w_j = 2u_j \sqrt{\sin(\phi_j + \theta) \sin(\phi_j - \theta)}. \tag{38b}$$

In Equations (37) and (38a), $l_0 = 0$ and $T_{N+1} = t$. The echo times, $t_{\text{echo}}^{(\boldsymbol{l},\boldsymbol{T})}$, occur at temporal locations where the Doppler phase cancels and are determined by the set of interferences, $\boldsymbol{l}$, and onset times, $\boldsymbol{T}$, that satisfy

$$t_{\text{echo}}^{(\boldsymbol{l},\boldsymbol{T})} = T_N - \frac{1}{l_N}\sum_{j=1}^{N-1} l_j(T_{j+1} - T_j). \tag{39}$$

Owing to the detection technique typically employed in experiments, one is sensitive only to the amplitude of the q-Fourier harmonic of the density distribution, which corresponds to $\chi_1^{(\boldsymbol{l})}$ $(l_N = 1)$. The scattered field amplitude for N-pulses is therefore given by

$$E^{(N)}(t;\boldsymbol{T}) \propto \chi_1^{(\boldsymbol{l})}(t;\boldsymbol{T}). \tag{40}$$

Setting $N = 2$ and $l_1 = -\bar{N}$ in Equation (40) gives the expression for the two-pulse scattered field at the $\bar{N}$th-order echo time (Equation [25b]).

An interesting feature of the N-pulse echo signal is that, in the absence of spontaneous emission ($\theta = 0$), the contrast of the grating at $t = t_{\text{echo}}^{(\boldsymbol{l},\boldsymbol{T})}$ is zero. There is a scattered field only at times $\sim\tau_{\text{coh}}/l_N$ about the echo times, just as in the two-pulse case. Thus, the echo technique produces conditions in the atomic sample at the echo times that are similar to those at $t = 0$, namely an absence in density modulation.

2.5.1 Three-Pulse Atom Interferometer

As an illustrative example, one can consider three sw pulses applied in the following sequence: $T_1 = 0$, $T_2 = T$, and $T_3 = T + \delta T$, and a read-out pulse applied at $t_{\text{echo}} = (\bar{N}+1)T$ to detect the $\bar{N}^{\text{th}}$-order echo. Just as in the two-pulse sequence considered in previous sections, the first two pulses cause all the momentum states to interfere in the vicinity of the echo time. However, only those states that differ by $\hbar\boldsymbol{q}$ are detected. The third pulse diffracts all the momentum states once more, as shown in Figure 13, but effectively converts the difference between those states that interfere at $(\bar{N}+1)T$ from $m\hbar\boldsymbol{q}$ $(m > 1)$ to $\hbar\boldsymbol{q}$. Equivalently, the third pulse displaces the $\bar{N}$th-order echo from $(\bar{N}+1)T$ to $(\bar{N}+1)T + \delta T$. However, there is still an echo at $(\bar{N}+1)T$ provided δT is an integer multiple of τ_q. In this way, the role of the third pulse is different from the first two pulses, whose sole purpose is to produce an echo at $(\bar{N}+1)T$.

The detected signal in this three-pulse scheme (as a function of δT) is sensitive to more sets of interferences than in the two-pulse sequence. As a result, the shape of the signal differs significantly from the two-pulse signal. One should expect periodic revivals in grating contrast as a function of δT, with maxima occurring when δT is an integer multiple of the recoil period, $\tau_q = \pi/\omega_q$.

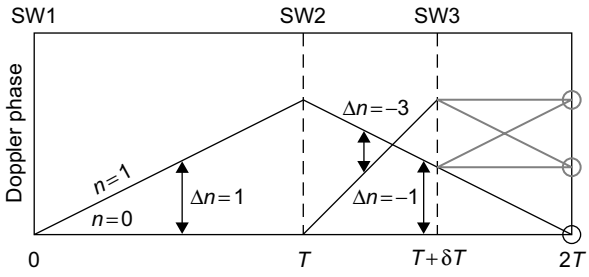

Figure 13 Simplified recoil diagram for the three-pulse signal. Two momentum states that differ by $|\Delta n| = 3$ ($|-\hbar q\rangle$ and $|2\hbar q\rangle$) interfere at $2T$ (gray circles) because of diffraction from the third pulse. This shows an example of how the third pulse can convert the difference between interfering states from $|\Delta n| > 1$ to $|\Delta n| = 1$.

Using Equation (39) with $l_1 = -\bar{N}$ and $l_2 = 1$, the three-pulse recoil signal can be approximated by

$$s^{(3)}(\delta T) \propto J_0^2\left(2u_3\sqrt{\sin(\omega_q \delta T + \theta)\sin(\omega_q \delta T - \theta)}\right), \tag{41}$$

where θ is a phase caused by spontaneous emission during the pulses, δT is varied between 0 and $\bar{N}T$, and T is held fixed. The signal as a function of δT is shown in Figure 14a for various pulse lengths, τ_3. The shape of the three-pulse signal is considerably different from that of the two-pulse signal. Its symmetric, periodic peak-shaped structure is particularly advantageous for precision measurements of ω_q. Furthermore, it can be shown that the full-width at half-maximum (FWHM) of the peaks is $\sim 1/u_3\omega_q$. This implies that by increasing the area of the third pulse (increasing the field intensity, pulse duration or decreasing the detuning) one can decrease the width of the peaks. This improves the determination of a given peak center and therefore the measurement of ω_q. This scaling law has been confirmed experimentally and shown in Figure 14b.

It is possible to reduce the fringe width even further by increasing the number of perturbation pulses (Beattie et al., 2009a). In order for each additional perturbation pulse to rephase momentum states at the echo time, they must be separated from all other perturbation pulses by a multiple of the recoil period, τ_q. Assuming that all perturbation pulses have the same pulse area, u_3, each additional pulse contributes to the signal shape an additional factor of $s^{(3)}(\delta T)$ from Equation (41). This effectively narrows each recoil fringe by a factor of $N^{-1/2}$ such that the FWHM scales as $\sim 1/\sqrt{N}u_3\omega_q$. Figure 14c shows the theoretically predicted and experimentally observed $(2 + N)$-pulse recoil signals. The scaling of the FWHM with N has been confirmed experimentally and is shown in Figure 14d.

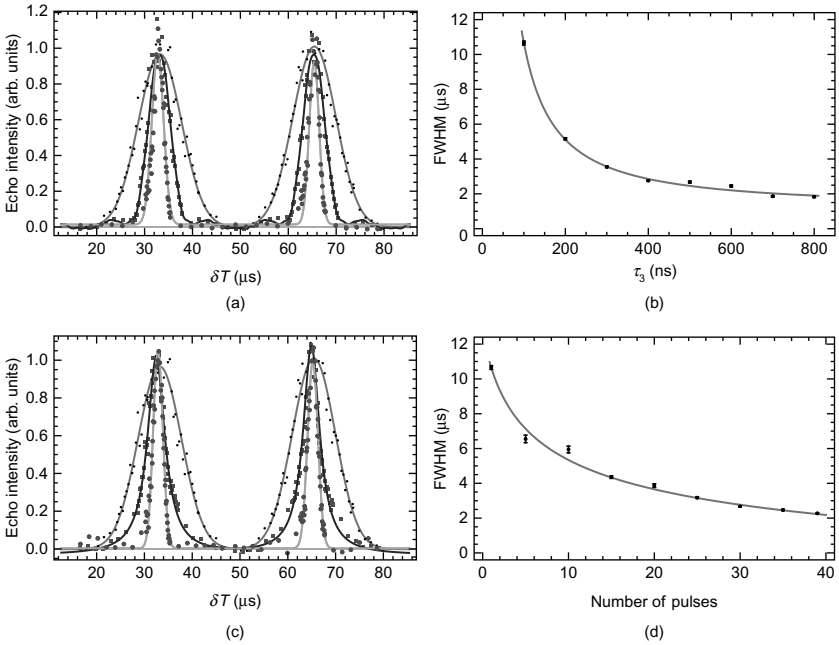

Figure 14 (a) Data from the three-pulse recoil experiment as a function of onset time, δT, for various pulse durations, τ_3. ~~Solid circles~~: $\tau_3 = 100$ ns; ~~solid~~ squares: $\tau_3 = 200$ ns; ~~large~~ circles: $\tau_3 = 500$ ns. (b) Scaling of the peak FWHM as a function of τ_3. Data is fitted to the function $A(\tau_3 - \tau_0)^{-n} + B$. The power was found to be $n = 1.18 \pm 0.88$. (c) Data from the $(2 + N)$-pulse recoil experiment as a function of onset time, δT, for various numbers of pulses, N, each with a duration of 100 ns. ~~Small circles:~~ $N = 1$; ~~solid~~ squares: $N = 15$; ~~large~~ circles: $N = 35$. (d) Scaling of the peak FWHM as a function of N. Data are fitted to the function $A(N - N_0)^{-n} + B$. The power was found to be $n = 0.32 \pm 0.47$. In both (a) and (c), data are fitted to different lineshapes (shown as solid lines) to guide the eye. The FWHM of the peaks was obtained from these fits. Other pulse parameters: $\Delta \sim 255$ MHz, $I \sim 250$ mW/cm^2, $\tau_1 = 700$ ns, $\tau_2 = 200$ ns.

In work relating to quantum kicked-rotors (Tonyushkin et al., 2009b), a large number of pulses was used, each with pulse area $u_j \ll 1$, for a measurement of ω_q. An appreciable loss in contrast and subsequent revival was observed when N was increased. For the technique described in Tonyushkin et al. (2009b), the time scale increases linearly with N. The prediction that the FWHM of each recoil fringe scales as $N^{-1/2}$ above is equivalent to the $N^{-3/2}$ scaling predicted in Tonyushkin et al. (2009b), since a factor of N^{-1} is related to the linear increase in time scale with an increase in N.

Figure 15a and b show a measurement of atomic recoil using the three-pulse technique. The sw pulses of the AI are separated by ~24 ms. The

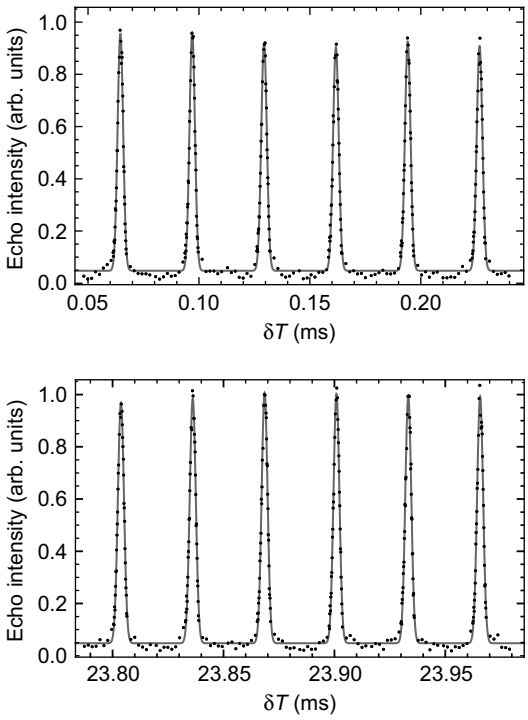

Figure 15 Recoil measurement using the three-pulse technique. Two windows are shown, one at $\delta T \sim 0.1$ ms (a) and one at $\delta T \sim 24$ ms (b). The solid line is a fit to the data consisting of a sum of Gaussians (one for each peak) that yields a measurement of the recoil frequency precise to ~350 ppb. Pulse parameters: $\tau_1 = 1100$ ns, $\tau_2 = 300$ ns, $\tau_3 = 400$ ns, $\Delta = 210$ MHz, intensity $I \sim 200$ mW/cm^2.

data were acquired in ~1 hour. A fit based on a sum of Gaussian lineshapes results in a measurement of ω_q precise to ~350 ppb. An interesting aspect of using a third pulse to measure ω_q is that the effect of signal decay due to the transit time of cold atoms is avoided because T is fixed.

In summary, the multiple-pulse technique is better suited for a precision measurement of ω_q than the two-pulse technique because the signal exhibits a simple, narrow-featured shape. Further improvements in the single measurement precision to the level of ~50 ppb appear to be attainable by improving the signal to noise ratio and exploiting scaling laws that can reduce the fringe width. Since the precision scales inversely proportional to the timescale of the experiment, additional improvements in precision can be achieved by increasing the transit time of cold atoms through the region of interaction with a larger excitation beam diameter. Studies of systematic effects in a precision measurement will include the angle between traveling-wave components of the standing wave and the

index of refraction of the atomic sample (Campbell et al., 2005), which is affected by both the atomic density and the frequency of the excitation beams.

3. LATTICE INTERFEROMETRY

3.1 Introduction

In the interferometer considered so far in this chapter, a set of off-resonant standing-wave pulses are applied to a cloud of cold atoms. One of the characteristic features of this interferometer is that at the exact times of the echoes (when the Doppler phase difference between interfering amplitudes is zero), the amplitude of the echo signal is zero. As discussed in Strekalov et al. (2002), this property applies to an interferometer of the type discussed here consisting of an arbitrary sequence of pulses—each satisfying the Raman–Nath condition—and is due to cancelation of the recoil phases of the amplitudes contributing to the echo signal at the same instant that the Doppler phases cancel. This cancelation is related to the fact that immediately after the first standing-wave pulse, the density of the atomic cloud is uniform, since, under the Raman–Nath condition, the atoms have not had time to move during the pulse. Consequently, one must observe the echo at times other than the exact echo time, where Doppler dephasing has reduced the size of the signal. A solution would be to cool the atoms further, for example using a BEC (Gupta et al., 2002) to achieve a subrecoil velocity spread. But this is technically more difficult and is likely to give rise to systematic errors due to interactions between atoms in the condensate.

In this section, we discuss a closely related type of echo-interferometer, which we refer to as a "lattice interferometer" (Andersen & Sleator, 2009), that doesn't suffer from the issue mentioned earlier. It uses atoms initially laser-cooled, then loaded into a one-dimensional (1D) optical lattice potential where it is further cooled in the potential, then released and later exposed to a pulse of the lattice potential. As is discussed below, one consequence of cooling the atoms in the lattice is that at the moment of release, the atomic density is strongly modulated with the period of the lattice potential. Consequently, at the exact echo times, the signal is a maximum, yielding a signal (in our measurements) more than a factor of four greater than obtained in the interferometer of Cahn et al. (1997). This interferometer shares the robustness against vibrations, accelerations, rotations, magnetic field gradients, and differences of AC Stark shifts between internal levels of the echo-type time-domain interferometers described in Section 1, and in Cahn et al. (1997).

In addition, we discuss how this interferometer performs when the optical lattice pulse violates the "short" pulse or Raman–Nath limit

(a regime not previously investigated in related interferometers), and find that a moderate violation of this limit can enhance the performance of the interferometer. We show that the interferometer reveals information on the quantum dynamics of atoms in an optical lattice potential, and thereby may be useful for the study of driven 1D systems (Raizen, 1999). Furthermore, we find that for specific pulse lengths, a coherent signal can occur at times that differ from the expected echo time by as much as $10\,\tau_{\mathrm{coh}}$, where $\tau_{\mathrm{coh}} = 2/q\sigma_v$ is the coherence time expected from the initial momentum spread of the atoms.

3.2 Description of the Interferometer

Figure 16 shows a timeline of the experiment, which uses a vapor cell loaded MOT of ^{85}Rb atoms loaded for 40 ms. An optical molasses stage of 7 ms further cools the atoms and loads them into the optical lattice, which is formed by two vertically polarized horizontally propagating laser beams with wave vectors $\boldsymbol{k}_1$ and $\boldsymbol{k}_2$, angled apart by 162°, and detuned 395 MHz above the $|5S_{1/2}, F = 3\rangle$ to $|5P_{3/2}, F' = 4\rangle$ transition. The lattice laser beams are clipped Gaussian beams with a diameter larger than the MOT cloud, so all the atoms in the MOT are loaded into the lattice. After the molasses stage, which cools the atoms to ∼36 μK, the repump laser remains on for 100 μs to prepare the atoms in the $F = 3$ ground state. Acousto-optic modulators control the optical lattice beams. At time $t = 0$ (∼10 μs after the turn-off of the repump light) we abruptly (in ∼20 ns) turn off the optical lattice. After leaving the atoms in darkness for a time T, we pulse the optical lattice on for a short time τ. Later we detect the amplitude of atomic density modulations with period $2\pi/q$, where $\boldsymbol{q} = \boldsymbol{k}_1 - \boldsymbol{k}_2$, by applying a weak off-resonant optical field along direction

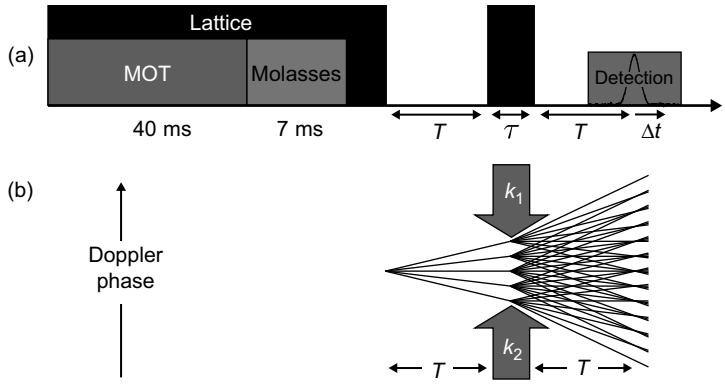

Figure 16 (a) Timeline of the experimental cycle. (b) Doppler phase diagram for atoms released from the optical lattice.

$\boldsymbol{k}_1$ and measuring the amplitude of the field Bragg scattered off of the atomic density modulation along the direction $\boldsymbol{k}_2$ using the heterodyne technique described in Section 1 and in Cahn et al. (1997).

3.3 Calculation of the Signal

To calculate the expected signal we assume that the atoms are in thermal equilibrium in the optical lattice, and localized to narrow regions near the potential minima, so they form a periodic density distribution and effectively experience a harmonic oscillator potential. Since the temperature of the atoms is $\sim$36 μK, their thermal de Broglie wave coherence length is much shorter than the period of the optical lattice. Under these conditions, it can be shown that the state of the atomic system can be closely approximated by an incoherent mixture of states identical to the ones obtained by an atomic plane wave of momentum $\boldsymbol{k}_0$ impinging on a periodic array with period $\boldsymbol{a} = (2\pi/q)\hat{\boldsymbol{q}}$ of Gaussian transmission functions, each with width σ (the width of the atomic density distribution in a single minimum in the lattice). Thus, we can write $\psi_{k_0}(\boldsymbol{r}) = \psi_0(\boldsymbol{r})\mathrm{e}^{i\boldsymbol{k}_0\cdot\boldsymbol{r}}$, where

$$\psi_0(\boldsymbol{r}) = \frac{1}{(2\pi\sigma^2)^{1/4}} \sum_m \exp[-(\boldsymbol{r} - m\boldsymbol{a})^2/4\sigma^2]. \tag{42}$$

We would like to express Equation (42) as a sum of momentum eigenstates, so we write

$$\psi_0(\boldsymbol{r}) = \sum_{n_1} A_{n_1} \mathrm{e}^{in_1\boldsymbol{q}\cdot\boldsymbol{r}}, \tag{43}$$

with

$$A_n = \frac{1}{a}\int_{a/2}^{a/2} \psi_0(x)\mathrm{e}^{-in_1qx}\mathrm{d}x \approx \frac{1}{a}\int_{\infty}^{\infty} \frac{\mathrm{e}^{-x^2/4\sigma^2}}{(2\pi\sigma^2)^{1/4}}\mathrm{e}^{-in_1qx}\mathrm{d}x \tag{44}$$

$$\approx \left(\sqrt{2}/a\right)(2\pi\sigma^2)^{1/4}\,\mathrm{e}^{-n_1^2(q\sigma)^2}, \tag{45}$$

where the integral is along the direction of $\boldsymbol{a}$. This gives, up to a constant factor,

$$\psi_{k_0}(\boldsymbol{r}, t=0) = \sum_{n_1=-\infty}^{\infty} \mathrm{e}^{-n_1^2(q\sigma)^2}\mathrm{e}^{i(\boldsymbol{k}_0+n_1\boldsymbol{q})\cdot\boldsymbol{r}}. \tag{46}$$

Each state ψ_{k_0} contributes to the mixture with a weight given by the momentum ($\hbar\boldsymbol{k}_0$) distribution of a gas of atoms in thermal equilibrium.

The experimental signal can be computed by first calculating the signal resulting from the system initially in state $\psi_{k_0}(\boldsymbol{r}, 0)$ and then summing this signal over the weighted distribution of $\boldsymbol{k}_0$.

After the lattice is turned off at $t = 0$, each plane wave, $\exp[i(\boldsymbol{k}_0 + n_1\boldsymbol{q}) \cdot \boldsymbol{r}]$, in Equation (46) acquires a phase $\phi = (\omega_{k_0} + n_1^2\omega_q + n_1\boldsymbol{q} \cdot \boldsymbol{v}_0)\, t$, where $\omega_q = \hbar q^2/2M$ is the (two-photon) recoil frequency and $n_1\boldsymbol{q} \cdot \boldsymbol{v}_0 t$ is the Doppler phase, which is proportional to the initial atomic velocity $\boldsymbol{v}_0 = \hbar\boldsymbol{k}_0/M$, and $\omega_{k_0} = \hbar k_0^2/2M$ contributes to an overall phase that can be ignored. The optical lattice pulse, turned on at time $t = T$, diffracts each plane wave into a set of plane waves with wave vectors differing by integer multiples of $\boldsymbol{q}$. If τ is so short that atomic motion can be neglected during the pulse (Raman–Nath condition), no Doppler phase evolution occurs during this time. Figure 16(b) shows a diagram of the Doppler phase evolution of various amplitudes as a function of time in the interferometer. Crossing lines in the diagram occur at times when different momentum states have the same Doppler phase, and atomic fringe patterns are produced at these times. In particular, fringe patterns with period $2\pi/q$ are produced close to times $t_{\bar{N}} = (\bar{N} + 1)T$ for positive integer $\bar{N}$ (the $t_{\bar{N}}$ are called echo times). A detailed calculation similar to the one in outlined in Section 1, which assumes that the interaction during the pulse is given by $H = \hbar\chi \cos(\boldsymbol{q} \cdot \boldsymbol{r})$, gives a signal

$$S(\Delta t) \propto \mathrm{e}^{-(q\sigma_v \Delta t/2)^2} \mathrm{e}^{-\frac{1}{2}\bar{N}^2(q\sigma)^2} J_{\bar{N}+1}\{2u \sin[\omega_q(\bar{N}T + \Delta t)]\}. \tag{47}$$

where $\sigma_v = \sqrt{2k_B\mathcal{T}/M}$, k_B is Boltzmann's constant, $\mathcal{T}$ the temperature of the atoms, $\Delta t \equiv t - t_{\bar{N}}$, and $u \sim \chi\,\tau$ is the area of the lattice pulse.

3.4 Experimental Results

Figure 17a shows the signal obtained at around $T = 81\,\mu\mathrm{s}$ with a short pulse of duration $\tau = 350\,\mathrm{ns}$ (solid curve). All data shown correspond to the fundamental echo $\bar{N} = 1$. The estimated temperature of the atomic gas was found by fitting Equation (47) to the data. The signals shown in Figure 17a are the largest that could be obtained in the short pulse limit with the laser power and detuning used. In contrast to the signal obtained from the interferometer in Cahn et al. (1997) (also shown in Figure 17a for a similar number of atoms), the lattice interferometer signal reaches a maximum at the echo time ($\Delta t = 0$) and with a maximal signal size more than a factor of four larger, demonstrating an improved signal-to-noise ratio and higher contrast of the atomic density modulation. We ascribe this to the fact that in this interferometer the signal is an echo of a density modulation of the atoms, whereas in Cahn et al. (1997) it is a velocity (or phase) modulation that with time evolves into a density modulation, but also partially dephases because of the thermal velocity spread of the atoms. By laser cooling the atoms into the optical lattice, we avoid the huge loss of

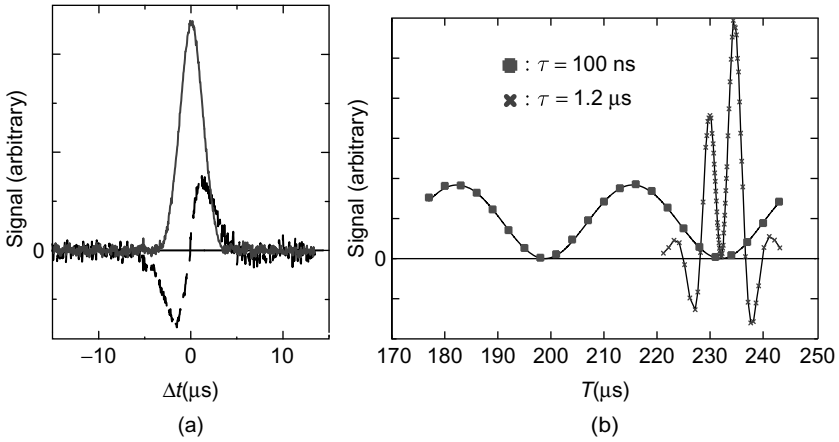

Figure 17 (a) Solid curve: signal from lattice interferometer for $\tau = 350\,\text{ns}$ and $T = 81\,\mu\text{s}$. Dashed curve: the maximum signal we could obtain from the interferometer described in Cahn et al. (1997). (b) Peak signal as a function of pulse separation T for small-area pulses $\tau = 100\,\text{ns}$ (squares). Peak signal theoretically expected from Equation (47) (corresponding solid curve). Crosses connected by a solid line: the measured peak signal for $\tau = 1.2\,\mu\text{s}$, too long to satisfy the Raman–Nath condition. The longer pulse yields sharper features in the signal.

atoms, associated with using an optical mask—the atom-optics analog of an absorption grating in light optics (Turlapov et al., 2005)—for generation of the atomic density modulation. Note that the revival of the density modulation shows that the atomic state continues to carry the information of its lattice preparation, despite its density distribution shortly after release being indistinguishable from a thermal cloud.

Equation (47) also shows that the peak signal at the echo time varies periodically as a function of T with period given by the Talbot time $\tau_T = 2\tau_q = 2\pi/\omega_q$. This interferometer can therefore be used to measure the Talbot time (or equivalently, the recoil frequency), which, together with other well-known constants, constitutes a measurement of the fine structure constant, α (see Section 2). Figure 17b shows the analytical prediction of Equation (47) together with the experimental measurements of the peak signal as a function of T for a pulse length of 100 ns. In the analytical prediction we use $\chi = 2.0\,\text{MHz}$ determined in a separate measurement of the value of τ that yields the first maximum in the signal for $T = 81\,\mu\text{s}$. The overall amplitude of the analytical result was adjusted to fit the data. By comparing the size of the echo signal for $\bar{N} = 1$, 2, and 3, we can use Equation (47) to extract the degree of localization, σ, of the atoms in the lattice. We find that $\sigma = 55\,\text{nm}$, or about 1/7th the 390-nm period of the lattice potential. This could be reduced by using a BEC released from an optical lattice.

Sharp features in the interferometric signal as a function of T (or equivalently higher frequency components in the signal) improves the precision with which the Talbot time and recoil frequency can be determined (Cataliotti et al., 2001). Equation (47) indicates that if one increases u, more oscillations and sharper features occur in each period when T is scanned, thus increasing the sensitivity of the interferometer. The depth of the lattice potential $\hbar\chi$, and thereby u, can be increased by increasing the power in the lattice beams, but these results were obtained using the maximum laser power available. Increasing τ will also increase u, but this will eventually lead to a breakdown of the Raman–Nath condition, and Equation (47) will no longer apply. When the Raman–Nath condition is violated, the signal is still periodic in T, however, with period τ_T independent of pulse duration. Thus, the recoil frequency can be determined simply from this period. It is therefore of interest to know what happens when the pulse length is increased beyond the Raman–Nath limit. Figure 17b shows the signal as a function of T for a pulse duration of $\tau = 1.2\,\mu$s, which is too long to satisfy the Raman–Nath condition. It is clear that the longer pulse yields sharper features in the signal as a function of T.

Figure 18 shows the echo signal as a function of both T and Δt for different pulse durations τ. Horizontal cross sections in this figure represent the signal as a function of Δt (as shown in Figure 17a), and vertical cross sections represent the signal as a function of T (as shown in Figure 17b). For $\tau = 1.2\,\mu$s (Figure 18c) we see a clear deviation from the results predicted by Equation (47), namely that the signal vanishes for T around $(n + 1/2)\tau_T/2$ with n an integer ($\sim$80 μs in Figure 18c), and that the signal is asymmetric around $n\tau_T/2$. However, the narrow "dark" fringe around $n\tau_T/2$ persists, enabling an accurate determination of τ_T. The experimental observation that the sharpest features of the echo signal are found for pulse durations between 1 and 2 μs is perhaps not surprising, since the optical lattice imparts maximum momentum into the atoms for durations around $\tau \sim \tau_{\text{osc}}/4$, where τ_{osc} is the oscillation period of an atom close to a potential minimum.

We use the sharp features described earlier to determine the Talbot time by taking data with high resolution in T for $\tau = 1.2\,\mu$s around $T = 65\,\mu$s and around $T = 455\,\mu$s—differing in T by $\sim$6 Talbot times (see Figure 18d). From this we obtain a value[1] of $h/M_{\text{Rb}} = (4.6997 \pm 0.0003) \times 10^{-9}$ m^2/s^2, where M_{Rb} is the mass of a ^{85}Rb atom, in agreement with the value of $h/M_{\text{Rb}} = 4.6994 \times 10^{-9}$ m^2/s^2 deduced from Audi et al. (2003). Our "large" uncertainty arises from the determination of the angle between the beams, a problem that can be overcome by using counter

[1]The uncertainties are one standard deviation combined systematic and statistical.

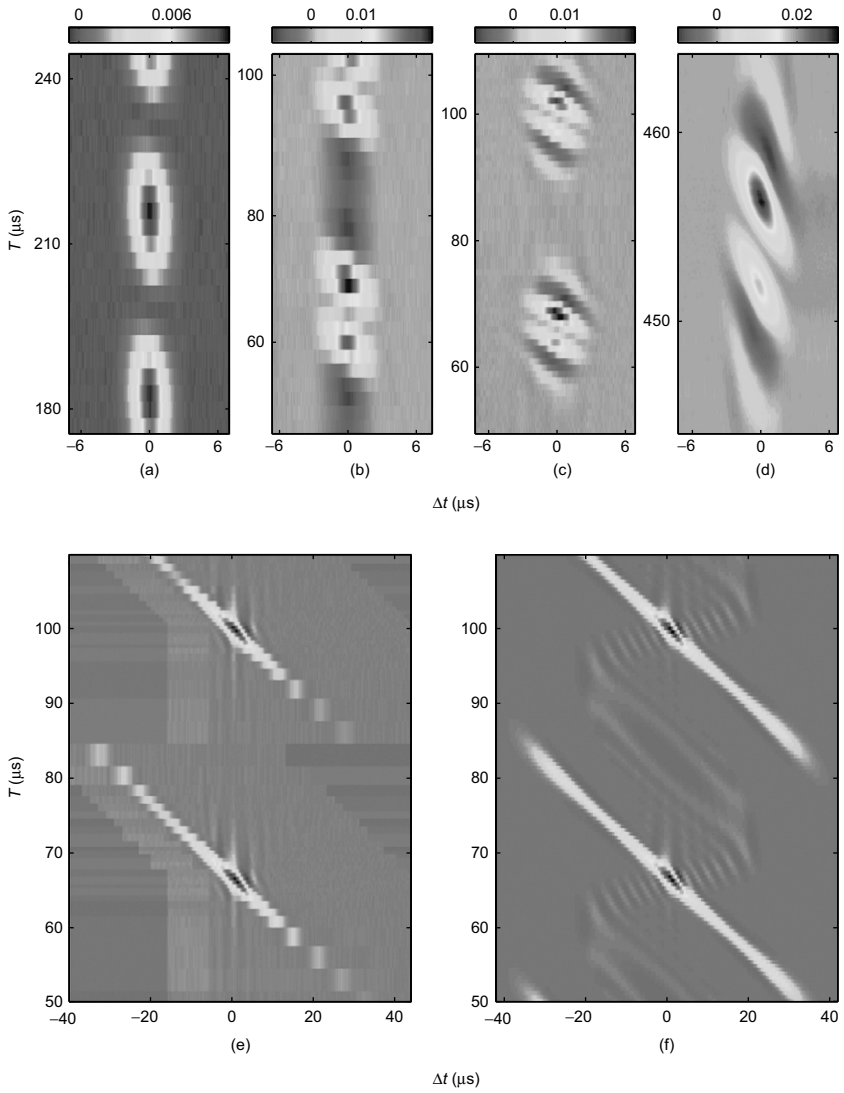

Figure 18 Echo signal as a function of Δt and time of the lattice pulse T (the echo time is $t_1 = 2T + \tau$). Figure 17b is a vertical cross section at the echo time ($\Delta t = 0$) and Figure 17a is a horizontal cross section of the data in this figure. (a), (b), (c): Experimental data for pulse durations $\tau = 100$ ns, 600 ns, and 1.2 μs, respectively. For $\tau = 1.2\,\mu$s, the signal vanishes for all T around 80 μs. (d) High-resolution experimental data for $\tau = 1.2\,\mu$s. (e) Experimental data for $\tau = 3.5\,\mu$s. Features as a function of T are no longer as sharp as for $\tau = 1.2\,\mu$s. We observe a coherent signal for times that differ greatly from the echo time. (f) Numerical calculation of the expected signal for the parameters of (e).

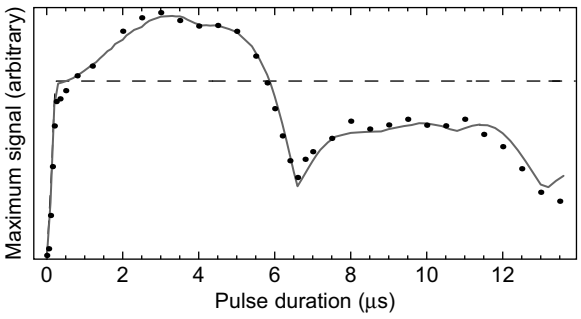

Figure 19 Maximum signal as a function of pulse duration. Dots are the data, and the solid curve is a numerical calculation multiplied by an exponential decay to accommodate for decoherence due to photon scattering. The dashed line is the maximum signal expected from Equation (47) and does not show oscillations. We see that violating the Raman–Nath condition can increase the contrast of the atomic density modulation.

propagating beams and coupling between optical fibers (Cladé et al., 2006; Muller et al., 2008).

For $\tau = 3.5\,\mu$s (see Figure 18e), we observe the interesting phenomenon that a coherent signal for certain values of T is observed for times that differ from the echo time $(2T + \tau)$ by as much as 40 μs. This is more than 10 times the decoherence time of a few μs expected from the initial thermal spread of atoms. The nature of the signal also seems to indicate that its occurrence is not due to long coherence times, but rather because the dynamics of the atoms during the lattice pulse enables a coherent rephasing at this time. We note that this phenomenon occurs for pulse durations τ around $\tau_{\text{osc}}/2$. Figure 18f shows a 1D numerical calculation of the expected signal for the same parameters as the experimental results in Figure 18e. No photon scattering was included in the calculation.

To further investigate the dynamics of the atoms in the optical lattice we measured the maximum signal size for a given pulse duration τ by scanning the pulse separation T. Figure 19 shows a plot of this maximum signal as a function of τ. We observe that violating the Raman–Nath limit can improve the contrast of the atomic density modulation since pulse lengths from 1 to 5 μs yield a larger signal than predicted by Equation (47) (also shown in Figure 19). In contrast to the prediction of Equation (47), the signal shows damped oscillations with a period of around 6.6 μs. This period is consistent with τ_{osc} reflecting a partial revival of the initial state at this time. This effect has been observed previously using a BEC in an optical lattice (Ovchinnikov et al., 1999), and the fact that it is easily seen in our data indicates that this interferometer can be used as a sensitive probe of the quantum dynamics in diffracting structures, including classical

chaotic systems such as the δ-kicked rotor (Raizen, 1999). Figure 19 also shows a numerical calculation of the expected maximum signal as a function of τ. This calculation is based on the coherent interaction of the atoms with the laser field, but to account for decay of coherence due to photon scattering in the optical lattice, includes a multiplicative exponential decay as a function of τ, where the decay rate of 3.5×10^4 s^{-1} is found by fitting to the data. This decay rate is smaller than the average photon scattering rate of 9×10^4 s^{-1} calculated from our measured value of χ and the detuning of the light.

In summary we have described an atom interferometer that uses atoms, laser-cooled into an optical lattice, followed by an optical-lattice pulse. The technique is capable of producing atomic density modulations with a contrast significantly higher than the interferometer of Cahn et al. (1997). This increases the signal-to-noise ratio of the interferometric signal. We discussed how the interferometer performs when the pulse violates the Raman–Nath condition and found that a moderate violation can improve the sensitivity and increase the contrast of the atomic density modulation. For specific pulse lengths in the long-pulse regime, we observe a coherent signal at times that differ greatly from the echo time. We showed that the interferometric signal can be used as a probe of the dynamics of the atoms in the optical lattice. The technique also reveals the degree of localization of atoms in an optical lattice, and may therefore be employed in the study of superfluid to Mott-insulator quantum phase transition of BECs in optical lattices (Greiner et al., 2002; Spielman et al., 2007).

4. FREQUENCY-DOMAIN AI EXPERIMENTS

4.1 Frequency-Domain Measurements of Recoil

This section describes an atom interferometric frequency-domain measurement of ω_q (Weel & Kumarakrishnan, 2003) that uses the echo technique to generate a ground-state Ramsey fringe pattern. This work is based on the scheme proposed in Dubetsky and Berman (1997).

Figure 20 shows the pulsed-laser fields used to excite the laser-cooled sample. At $t = 0$, an excitation pulse consisting of two off-resonant, counter-propagating traveling waves with frequencies ω_1 and ω_2 is used to drive two-photon transitions in atoms prepared in a single hyperfine ground state. The sample is again excited at time $t = T$ by a second set of traveling-wave pulses with reversed k-vectors. As a result, the sample experiences an intensity modulation that is translated along two opposing directions. Reversing the directions of the second set of excitation pulses results in a cancelation of Doppler phases associated with momentum states differing by $\hbar q$ that interfere in the vicinity of the echo time $t =$

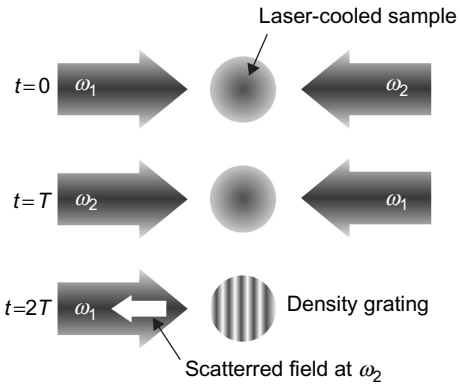

Figure 20 Schematic diagram of pulsed laser fields used in experiment.

$2T$. Here, $q = 2k$. The rephased density grating formed in the sample is detected by scattering an off-resonant traveling wave with frequency ω_1 and measuring the amplitude and phase of the scattered light at frequency ω_2. In this manner, it is possible to probe the oscillatory Ramsey phase $\phi = T\delta$ acquired by the grating, which depends on the frequency difference $\delta = \omega_1 - \omega_2$. In comparison, other Ramsey fringe experiments involving ground or excited states (Barger et al., 1979; Bergquist et al., 1977; Ruschewitz et al., 1998; Sengstock et al., 1993; Weiss et al., 1993) rely on similar excitation schemes and the detuning dependence of the population or coherence associated with an atomic level.

Using the treatment in (Dubetsky & Berman, 1997), the back-scattered electric field amplitude can be expressed as

$$S(\delta; T) = \exp(4iT\delta)J_2[2u_2 \sin(\omega_q T)], \tag{48}$$

where u_2 is the pulse area of the second excitation pulse. The complex exponential in Equation (48) makes it necessary to measure the phase of the signal in order to observe the effect of recoil.

In Ramsey fringe experiments using atomic beams (Bordé et al., 1984), the excitation zones are spatially separated. The time between interactions with the laser fields, T, differs for each velocity class associated with the longitudinal velocity distribution of the atomic source. As a consequence, the fringe pattern can be observed because the signal is averaged over the entire velocity distribution. In an experiment with a laser-cooled sample, the time separation between interactions with light are the same for all the atoms. Therefore, it is necessary to average the signal over T to obtain the Ramsey lineshape (Vasilenko et al., 1985).

4.2 Experimental Details

The experiment is carried out in a laser-cooled sample with a temperature of $\sim 200\,\mu$K that contains $\sim 10^8$ Rb atoms. The traveling-wave pulses used for atom interferometry are tuned ~ 90 MHz above the $F = 3 \rightarrow F = 4'$ transition in ^{85}Rb, and controlled by AOMs. The AOMs are driven by oscillators which are phase locked to a commercially available rubidium frequency standard with a stability characterized by a 1-second Allan deviation of 2×10^{-11}. The oscillators operate near 250 MHz and the frequency difference, δ, can be adjusted to within 1 mHz. The time separation, T, between pulses can be controlled with an accuracy of 500 ps using delay generators with time bases slaved to the rubidium standard. Signal detection is accomplished using the balanced heterodyne detection system used in Cahn et al. (1997) and Weel and Kumarakrishnan (2003). The echo signal is observed on both channels of the detection system in the form of a beat note. These signals are mixed down to DC to obtain the in-phase and in-quadrature components from which the signal amplitude and phase can be determined.

4.3 Results and Discussion

By integrating the first half (before the zero crossing) of the dispersion-shaped echo envelope (shown in Fig. 3a) and subtracting the integral of the second half, it is possible to obtain an amplitude component. Figure 21a shows the amplitude as a function of δ for $T = 100\,\mu$s. The amplitude exhibits an oscillatory dependence on δ given by $S_0 = \cos(T\delta)$ as seen from the fit in Figure 21a. For a fixed value of T, the average value of the oscillation frequency is determined from the in-phase and

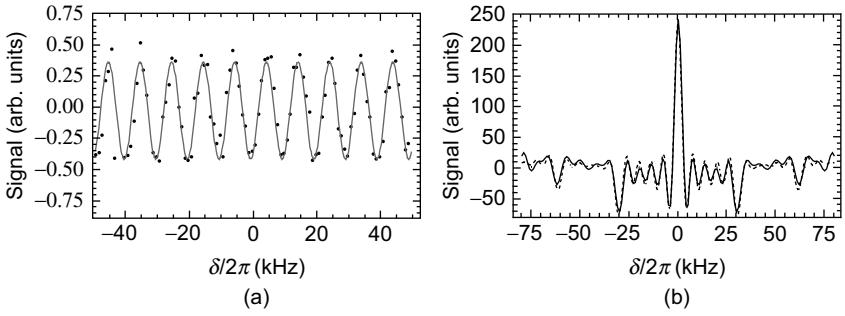

Figure 21 (a) Oscillation of a component of the echo signal as a function of detuning, δ, for $T = 100\,\mu$s. Data are fitted to the form $\cos(T\delta)$ (solid line). The fit gives a period of 9.99 kHz, which is consistent with $T = 100\,\mu$s. (b) Average of the signal over T—Ramsey fringe pattern. The solid line is data and the dashed line is a fit which yields $\omega_q = 97.0 \times 10^3$ s^{-1} and $u_2 = 1.8$.

in-quadrature components of the signal. The measurement is repeated for different time pulse separations, T. A linear fit of the measured period as a function of T gives a slope of 4.004 and an offset of 0.7 μs. The value of the slope is in agreement with Equation (48), which predicts a slope of 4.

The amplitudes of the oscillatory signals are weighted to compensate for the exponential decay of the echo amplitude versus T due to decoherence from scattered light and collisions. The Ramsey fringe pattern shown in Figure 21b is obtained by averaging a particular signal component over the range $T = 12 \rightarrow 164\,\mu$s in steps of 4 μs.

The fringe pattern in Figure 21b shows peaks at $\pm 0.5\,\omega_q$ and $\pm\,\omega_q$, which is consistent with Equation (48). The value of ω_q is obtained by fitting the data to Equation (48) using a least squares fit with ω_q and u_2 as free parameters. The fit yields $\omega_q = 97.0 \times 10^3\ \mathrm{s}^{-1}$, which is consistent with the expected value of the two-photon recoil frequency. Analysis of the residuals allows a determination of ω_q with a precision of $\sim 1/10^3$. The precision can be improved by measuring the frequency difference between widely separated recoil components that can be recorded by increasing the pulse area u_2. As in all Ramsey experiments, the range of detunings (~10 MHz) is determined by the excitation pulse bandwidth, and the width of the recoil peaks is expected to scale as $\sim 1/T$.

4.4 Frequency Synthesizer

A potential advantage of this measurement technique is that possible systematic uncertainties in the definition of T that can affect time-domain experiments are avoided, since the signal is averaged over T. In contrast to Ramsey experiments with excited states (Barger et al., 1979; Bergquist et al., 1977; Ruschewitz et al., 1998; Sengstock et al., 1993) that are limited by the radiative decay time, the precision that can be achieved if decoherence mechanisms are eliminated should be limited only by the transit time of ground-state atoms through the region of interaction. Since the experiment utilizes the same laser to generate excitation frequencies ω_1 and ω_2, variations in laser frequency are common to both beams and a laser with an ultra narrow linewidth is not required, as it is in atomic clock experiments (Barger et al., 1979; Bergquist et al., 1977; Ruschewitz et al., 1998; Sengstock et al., 1993). In comparison, an advantage of time-domain measurements is that they are insensitive to the effect of vibrations, since they do not rely on the phase of the scattered electric field.

If the transit time limit is achieved, as in time-domain experiments, the precision of frequency-domain measurements will depend on the precision and tunability of δ. The measurement in Weel and Kumarakrishnan (2003) relied on a RF synthesizer assembled from commercially available components to produce dual outputs (differing by δ) to drive the excitation AOMs. The synthesizer allows δ to be varied over ~10 MHz in steps

of 1 mHz while maintaining frequency stability with respect to a master reference oscillator. Additionally, a simple measurement and correction loop ensures that the outputs maintain a fixed phase relationship if δ is varied.

The block diagram of the synthesizer is shown in Figure 22. In this circuit, there are two phase-locked loops (PLLs) operating at 250 MHz and 238 MHz. These are fractional-divide-by-N PLLs, meaning that the reference and output frequencies are not necessarily related by an integer multiple. These devices are tunable only in steps of $\sim$0.2 MHz, necessitating additional electronics for fine-tuning. To tune the output at 250 MHz + δ, a commercially available arbitrary waveform generator (AWG) tunable in steps as small as 1 mHz is incorporated. This device has a maximum output frequency of 30 MHz and is set to 12 MHz + δ. The choice of 12 MHz ensured that when the AWG's output is mixed with the PLL output at 238 MHz, a sum frequency near 250 MHz is obtained. A signal with frequency 250 MHz + δ is obtained by filtering out the difference frequency. Filtering is accomplished using a commercially fabricated narrow-band notch filter (FWHM 8 MHz) whose center frequency is 250 MHz. Both of the PLLs and the AWG are referenced to a rubidium clock operating at 10 MHz. This clock has excellent short-term stability, with a 1-second Allan deviation of 2×10^{-11}. Both the 250 MHz and 250 MHz + δ outputs are locked in phase to the stable Rb clock, and are therefore phase-locked to each other.

4.5 Measurements of Rotation

The frequency synthesizer developed for the recoil measurement is also suitable for a proof of concept measurement of rotation. If a closed-loop optical interferometer rotates about an axis perpendicular to its enclosed

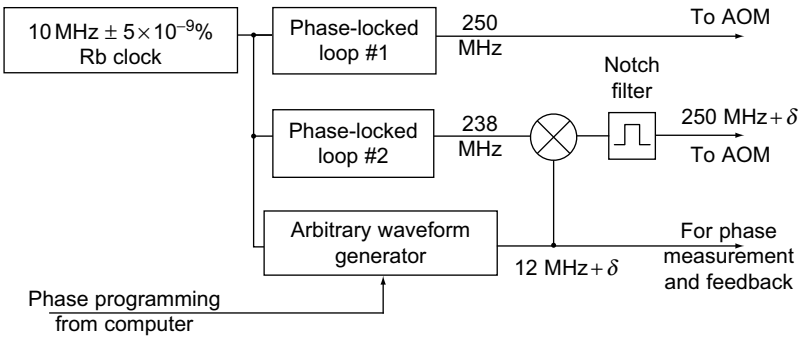

Figure 22 The block diagram for the synthesizer, where $\otimes$ is a RF mixer.

area, the path difference between counter-propagating waves due to rotation produces a phase shift $\Delta\phi_R = \Omega Ak/c$ (Sagnac effect). Here, Ω is the frequency of rotation, A is the area enclosed by the interferometer, k is the wave vector, and c is the speed of light. The Sagnac effect is the basis for the fibre ring gyroscope (Vali & Shorthill, 1976), a device commonly used in navigation. The obvious advantage of laser gyroscopes is that the enclosed area can be enhanced by sending the light on many round-trips, thereby improving the sensitivity.

For an AI, the corresponding phase shift is $\Delta\phi_R = \Omega AM/\hbar$, where M is the mass of the atom. Replacing light waves with matter waves can lead to a significant improvement in sensitivity. This is because, for the same enclosed area, the phase shift is $Mc/\hbar k \sim 10^{10}$ times greater for atoms in comparison with light. For atoms, the challenge is to produce a large enclosed area. Such atom gyroscopes should be able to detect rotations as small as 6×10^{-3} deg/h (Sleator et al., 1999). This is around three orders of magnitude smaller than the Earth's rate of rotation. Examples of AI-based measurements of rotation include a Raman interferometer measurement in a cesium atomic beam (Durfee et al., 2006; Gustavson et al., 1997a) and a BEC experiment in which the rotational phase shift is enhanced by circulating the sample in an elongated trap (Burke & Sackett, 2009). Another approach involves confining the atoms within a linear magnetic guide and moving this guide back and forth while diffracting the atoms, thereby enhancing the enclosed area through multiple circuits of the same small physical area (Wu et al., 2007).

If the Ramsey fringe experiment is carried out by launching a cloud of cold atoms across the zone of interaction in a direction such that $\boldsymbol{A} \cdot \boldsymbol{\Omega}$ is a maximum, the effect of the earth's rotation is expected to produce a shift in the position of the central fringe in Figure 21b. The area enclosed by the AI can be estimated as

$$A = \frac{\hbar q v T^2}{M}. \tag{49}$$

For typical operating parameters of $T \sim 10$ ms and an atom launch speed $v \sim 2.5$ m/s the area is 0.76 mm^2. Assuming that Ω is the vertical component of the Earth's rotation in Toronto, we obtain a fringe shift of 0.8 Hz. The expected width of the central fringe for these parameters is 20 Hz, which suggests that the fringe shift should be easily observable, since δ can be varied in subhertz steps.

Although this experiment is simple in concept, the fringe shift due to rotation is indistinguishable from the shift produced by gravitational acceleration. Therefore, it is critical to align the AI beams in a plane

perpendicular to the local gravitational field and to measure the angle of the beams with respect to the horizontal.

5. TIME-DOMAIN AI EXPERIMENTS—GRAVITY

5.1 Introduction

Atom interferometers based on cold atoms have enormous practical applications related to inertial sensing because of the extraordinary sensitivity to gravitational acceleration, g (Peters et al., 1999), gravity gradients, (McGuirk et al., 2002; Snadden et al., 1998), and rotation (Durfee et al., 2006; Gustavson et al., 1997b, 2000). Common applications include oil and mineral prospecting, seismic exploration and monitoring, and correction of tidal charts. Most of these developments have been realized using the well-known Raman interferometer (Kasevich & Chu, 1991) in which cold cesium atoms are manipulated in two hyperfine ground states using optical Raman transitions. Raman interferometers have also been used for precision measurements of the universal gravitational constant, G (Fixler et al., 2007; Lamporesi et al., 2008), and gravitational redshift (Müller et al., 2010). The technology based on this class of interferometers has become sufficiently advanced that it is being utilized for remote sensing using mobile payloads (Le Gouët et al., 2008; Young et al., 2007; Yu et al., 2006). Another independent technique for realizing precise measurements of gravity in a compact setup involves exploiting the properties of Bloch oscillations in an optical lattice (Poli et al., 2011).

Despite the advances of Raman interferometers, it is interesting to consider the potential for realizing precise measurements of gravitational acceleration using the single-state echo type interferometer used for recoil measurements as described in earlier sections. The AI is based on the configuration developed at NYU (Cahn et al., 1997; Weel et al., 2006). As in the case of cold-atom Raman interferometers, the timescale of the experiment is determined by the transit time of atoms through the region of interaction defined by the laser beams. A particular advantage of the echo AI is that only a single laser frequency is used and that no velocity selection is required. Transit-time-limited recoil experiments using this technique that are presented in this work indicate that state selection may not be required if magnetic gradients are adequately suppressed (Weel et al., 2006).

5.2 Theoretical Background

The AI involves excitation of the sample along the vertical by two standing-wave pulses separated by a time T as shown in Figure 23. This configuration is similar to that of the AI used in the time-domain

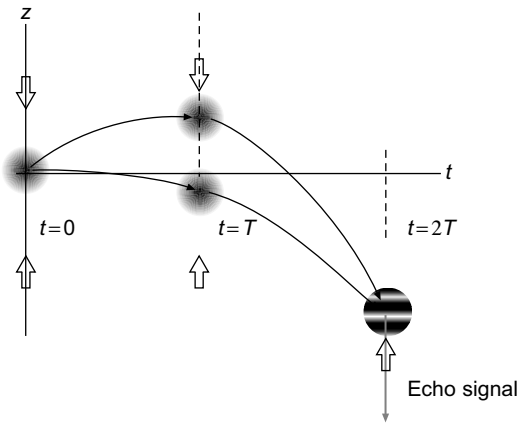

Figure 23 Curved trajectories of atomic wave packets due to gravity.

measurements of atomic recoil. The traveling-wave components of the standing-wave pulses are sufficiently blue detuned with respect to the excited state such that the effects of spontaneous emission during excitation can be ignored. The durations of the excitation pulses are sufficiently short, meeting the Raman–Nath criterion that the displacement of atoms is small compared to the standing-wave period during the interaction time. The first pulse at $t = 0$ diffracts atoms into a superposition of momentum states that differ by $n\hbar q$, where $q = 2k$ for counter-propagating beams and $\boldsymbol{k} = 2\pi/\lambda\hat{z}$ is the wavevector of the laser light. The $\lambda/2$ grating that is formed by atoms focused to the nodes of the standing wave potential is rephased by the second standing-wave pulse at $t = T$ in the vicinity of the echo time $t = 2T$. The determination of gravitational acceleration relies on measuring the contrast and phase of the grating by coherently back-scattering a traveling-wave read-out pulse from the sample.

Figure 23 shows a recoil diagram representing curved trajectories of a subset of momentum states that contribute to the signal. The read-out pulse detects the amplitude and phase of the matter wave interference in the vicinity of $2T$ only from trajectories that differ by $\hbar q$. It is possible to show that the gravitational phase shift is not related to the difference in path lengths between the arms of the interferometer. Rather, it is related to the energy of the atom that is affected by both recoil and gravity. Using the action principle, it can be shown that the phase accumulation due to gravity scales as gT^2. Thus, the measurement of gravity relies on the connection of the phase of the back-scattered light and the phase of the grating.

A calculation of the signal in the absence of spontaneous emission is discussed in Cahn et al. (1997). It can be shown that the back-scattered

electric field amplitude is proportional to the $\lambda/2$-periodic spatial component (q-Fourier harmonic) of the atomic density grating. The echo signal (scattered field amplitude) can be written as

$$E(\Delta t; T) \propto -e^{-(\Delta t/\tau_{coh})^2} J_1[2u_1 \sin(\omega_q \Delta t)] J_2\{2u_2 \sin[\omega_q (T + \Delta t)]\}, \tag{50}$$

where $J_n(x)$ is the nth-order Bessel function of the first kind, u_1 and u_2 are the pulse areas of the first and second standing-wave pulses, respectively, which define the atom-field coupling, $\omega_q = \hbar q^2/2M$ is the two-photon recoil frequency, and $\Delta t = t - 2T$ is the time relative to the echo time.

In the presence of gravity, the echo signal can be shown to be (Weel et al., 2006)

$$E_g(\Delta t; T) = E(\Delta t; T) e^{i\phi_g(\Delta t; T)}, \tag{51a}$$

$$\phi_g(\Delta t; T) = -\frac{qg}{2}\left(2T^2 + 4T\Delta t + \Delta t^2\right), \tag{51b}$$

where ϕ_g is the phase of the atomic grating, which is accelerating downward because of gravity. This phase is imprinted on the light scattered by the atoms from the read-out pulse. It is useful to split the phase due to gravity into two components, $\phi_g = \phi_{AI} + \phi_D$. The first term, $\phi_{AI} = -qgT^2$, is referred to as the AI phase, since it depends solely on T and is proportional to the area of the interferometer. The second term, $\phi_D = -qg(2T\Delta t + \Delta t^2/2)$, is called the Doppler phase, since it can be shown that $\phi_D = qv(t)\Delta t$, where $v(t) = \partial(\phi_D/q)/\partial\Delta t = -gt$ is the speed the atoms have gained in the presence of gravity.

Figure 24a is an illustration of the effect of the Doppler phase on the signal envelope at fixed T. The overall signal amplitude as a function of T in Figure 24b illustrates the modulation at the recoil period $\tau_q = \pi/\omega q$ and the increasing oscillation frequency due to the interferometer phase. The experiment relies on measuring the phase of the signal with respect to a frame of reference in which the atomic sample is falling in gravity. Such an inertial reference frame can be defined by an optical local oscillator (LO) with a frequency ω_{LO}. The back-scattered light from the sample due to the read-out pulse with a frequency ω_{AI} is detected in the form of a beat note at a frequency $\omega_{LO} - \omega_{AI}$ using a heterodyne technique (Cahn et al., 1997; Shim et al., 2002, 2005; Weel et al., 2006).

The electric field of the LO can be written as $E_{LO}(z, t) = E_0 e^{i(kz - \omega_{LO} t)}$, while the scattered electric field from the atoms has the form $E_{AI}(z, t) = E(T; \Delta t) e^{i(k(z+\Delta z) - \omega_{AI} t)}$. The heterodyne signal produced by overlapping the two beams on a photodetector can be shown to be

$$I(t) \propto E_0 E(T; \Delta t) \cos[(\omega_{AI} - \omega_{LO})t + k\Delta z] \tag{52}$$

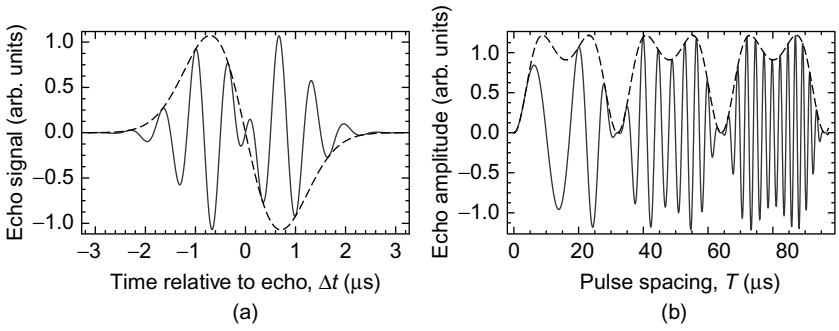

Figure 24 Illustrative plots representing the echo signal in Equation (51a) and the dependence of the AI phase as a function of T in Equation (51b). (a) Echo signal (shown as the dashed line) exhibits a dispersion shape in the absence of gravity. The echo signal in the presence of gravity (shown as the solid line) exhibits additional oscillations due to the Doppler phase in Equation (51b). (b) The amplitude of the echo signal as a function of T (dashed curve) is modulated at the recoil frequency, ω_q. The solid curve shows the in-phase component of the echo amplitude in the presence of gravity. A value of $g = 980$ m/s^2 has been used so that the changing frequency is evident over successive recoil periods. This represents the effect of the AI phase term in Equation (51b). In experiments involving laser-cooled rubidium atoms, the duration of the signal envelope is $\tau_{\text{coh}} \approx 2\,\mu$s, and the recoil period $\tau_q \approx 32\,\mu$s.

where $E(T; \Delta t)$ is given by Equation (50) and

$$\Delta z = -\frac{1}{2} g(2T)^2 + v_0(2T) + z_0. \tag{53}$$

Here, the grating displacement Δz is determined by g, a launch velocity v_0, and the initial position of the grating, z_0. The next section describes how the in-phase and in-quadrature components of the electric field are obtained from the signal intensity in Equation (52).

5.3 Experimental Setup

Figure 25a shows the experimental setup. Figure 25b illustrates the displacement Δz given by Equation (53). An acousto-optic modulator (AOM) is used to produce the excitation beams. The diffracted beam from the AOM passes through the atom cloud and is reflected by a corner cube retro-reflector to produce a standing wave. At the time of the read-out pulse, a mechanical shutter blocks the retro-reflection to produce a traveling wave. The undiffracted beam from the AOM is the LO, which is aligned through the same optical elements as the excitation beam and is physically separated from the atomic cloud. The back-scattered light from the sample and the LO are combined on a balanced heterodyne detector to produce a beat note at $\omega_{\text{RF}} = \omega_{\text{LO}} - \omega_{\text{AI}}$. The heterodyne signal is

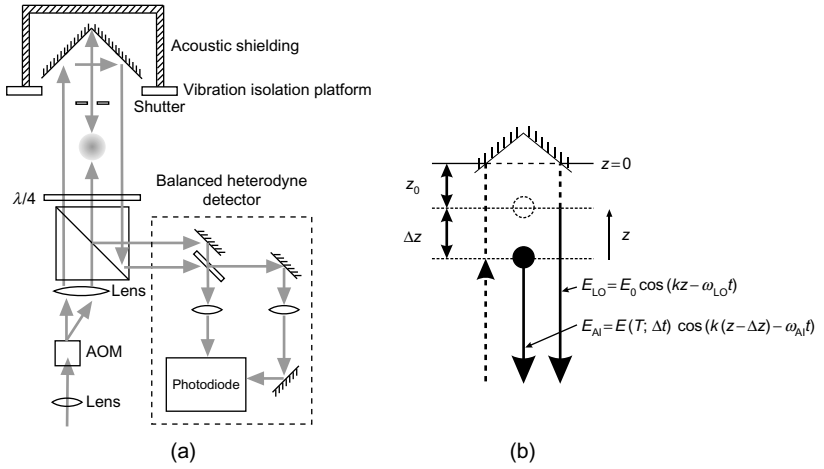

Figure 25 (a) Experimental setup. (b) Illustration of beam paths and cloud displacement in Equation (53). As T is increased, the atom cloud falls in gravity, changing the path difference between the back-scattered signal and the local oscillator.

mixed down to DC using the RF oscillator driving the AOM to generate the in-phase and in-quadrature components of the back-scattered electric field. The signal components are squared and integrated to obtain the in-phase and in-quadrature amplitudes. The total signal amplitude is equal to the individual component amplitudes combined in quadrature.

5.4 Measurement of g

Figure 26a shows the in-phase component of the scattered field in the vicinity of the echo for $T \sim 1.5$ ms. The signal envelope can be modeled by Equation (51a). At small values of T, the effect of gravity is not appreciable and the signal envelope resembles a dispersion shape. Figure 26b shows the echo signal shape for a larger pulse separation: $T \sim 11$ ms. The signal envelope is modulated by the Δt-dependent Doppler phase, $\phi_D = -qgt\Delta t$, due to the effect of gravity. It is interesting that g can be inferred from the echo signal shape by measuring the change in the Doppler frequency as a function of t, where t is the time relative to trap turn-off. Here, t can be changed by increasing the area of the interferometer (i.e., increasing T), or by holding T constant and varying the timing of the excitation pulses relative to trap turn-off. Figure 26c shows the in-phase and in-quadrature components of the signal as a function of T. The two signals can be used to measure the AI phase, $\phi_{AI} = -qgT^2$. Since the AI phase scales as T^2, while the Doppler frequency effectively scales as T, a measurement of ϕ_{AI} results in a more sensitive measurement of g.

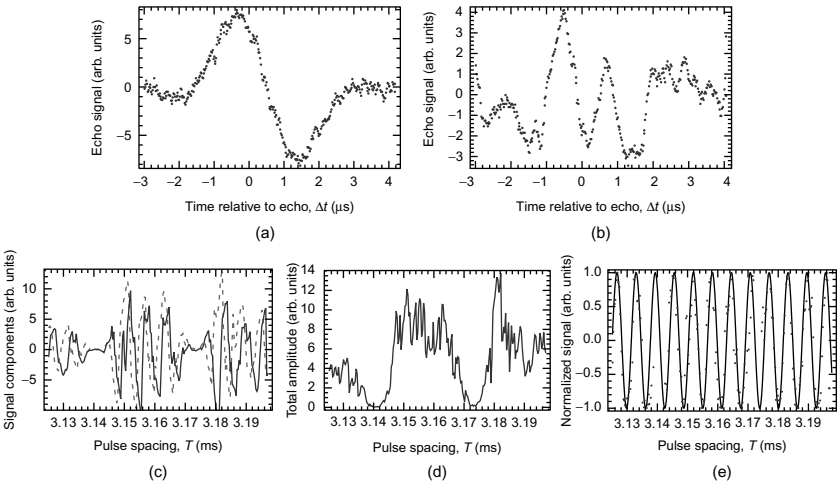

Figure 26 (a) Dispersion-shaped echo envelope at $T \sim 1.5$ ms. (b) Echo envelope modulated because of the effect of gravity at $T \sim 11$ ms. (c) In-phase (dashed) and in-quadrature (solid) components of the signal as a function of T obtained by averaging 32 repetitions. (d) Total signal amplitude (components combined in quadrature) as a function of T, showing modulation due to atomic recoil. (e) In-phase component of the signal as a function of T obtained by normalizing the total signal amplitude.

Figure 26d represents the total signal amplitude obtained from the signal components combined in quadrature. The shape of the signal, which is modeled by the square of Equation (50), exhibits recoil modulation at $2\omega_q$ given by $J_2^2[2u_2 \sin(\omega_q T)]$. Figure 26e shows ϕ_{AI} as a function of T. The AI phase has the functional form $\cos(-qgT^2 + qv_0T + \phi_0)$, where v_0 is the initial launch velocity v_0 of the atomic cloud and ϕ_0 is an arbitrary phase representing the initial position of the grating. The data in this figure were obtained by normalizing the in-phase component of the signal using the total signal amplitude. Similar data are obtained in a number of discrete windows over the timescale of the experiment ($2T \sim 20$ ms). A least-squares fit of the data across all observational windows yielded a measurement of g precise to 5 part per million (ppm).

Other work related to gravimetry that involves repeated reflections in a multipulse AI is discussed in Hughes et al. (2009).

5.5 Future Prospects

The preliminary measurement presented here relied on turning on an attenuated excitation beam during the time in which the atom trap is loaded, measuring the equipment phase and correcting the effect of vibrations by actively controlling the phase of the RF oscillator used

to drive the AOM. In this method, the feedback can be engaged during the period the atom trap is loaded, but not during the excitation pulses. As a result, the phase stability progressively deteriorates over the timescale of the measurement. The experimental timescale was limited by the magnetization of the stainless steel vacuum chamber. Several developments suggest that the precision in the determination of g can be improved significantly. Atomic recoil experiments using this AI have achieved transit-time limited timescales of $2T \sim 70$ ms in a nonmagnetizable glass vacuum chamber in which magnetic gradients were suppressed using external canceling coils. Additionally, the experimental setup shown in Fig[illegible]fied to include a probe beam that continuously[illegible]ns resulting in a hundredfold improvement in phase stability. If a transit time of 300 ms is achieved, a compact experiment can be realized using an atomic fountain. Under these conditions, it is anticipated that competitive measurements of g precise to better than ~1 part per billion (ppb) is possible.

Insert extended hyphen: ---

6. INTERNAL STATE LABELED INTERFEROMETER

6.1 Introduction

In this section, we describe the temporal evolution of magnetic sublevel coherences in laser-cooled samples under the influence of static magnetic fields. Previous work (Chan et al., 2008; Kumarakrishnan et al., 1998a,b) has shown that spatially periodic superposition states (coherence gratings) of magnetic sublevels within the same hyperfine ground-state manifold can be optically excited using two-photon transitions driven by appropriately polarized laser fields. For excitation by counter-propagating pulses, the grating period is $\lambda/2$, where λ is the wavelength of light. The decay time of the coherence due to Doppler dephasing occurs on a time scale of a few microseconds in which the displacement of a typical atom exceeds the grating period. For this geometry, the effect of atomic recoil is significant as in the standing-wave experiments described in earlier sections. In contrast to single-state interferometers, echo experiments involving magnetic sublevel coherences represent state-labeled interferometers in which the exchange of photons with the laser fields is associated with a precise change in internal state (Kasevich & Chu, 1991). For nearly copropagating small-angle excitation, recoil effects are not important and the spatial period can be $\sim 1000\,\lambda$. As a result, the decay time of the coherence can be several milliseconds. The relatively long coherence decay time and the ability to apply a uniform magnetic field across a compact laser-cooled sample can be exploited for precision measurements of magnetic interactions such as atomic g-factor ratios. Such a measurement relies on a determination of the Larmor frequency ω_L associated with the

evolution of a coherent superposition of magnetic levels in a static magnetic field. We use a magneto-optical trap (MOT) consisting of spatially overlapped samples of laser-cooled ^{85}Rb and ^{87}Rb isotopes. Our measurements suggest that a precision of better than 1 ppm is attainable. Such a measurement represents a sensitive test of the Zeeman Hamiltonian. In comparison, pioneering measurements (Cohen-Tannoudji & Kastler, 1966; Cohen-Tannoudji et al., 1969; White et al., 1968) used RF spectroscopy to ensure narrow linewidths and paraffin-coated vapor cells to prevent spin relaxation from wall collisions (that resulted in transit-time-limited signal decay) to achieve precisions of a few ppm.

We use coherent transient effects designated as magnetic grating free induction decay (MGFID) and magnetic grating echoes (MGE) that were originally predicted in Dubetsky and Berman (1994). A laser-cooled gas is excited using two simultaneous traveling-wave laser pulses applied at $t = 0$ with wave vectors $\boldsymbol{k}_1$ and $\boldsymbol{k}_2$ at a small angle ($\theta' \sim 10$ mrad), as shown in Figure 27a. The individual traveling waves pulses have orthogonal linear or circular polarizations so that it is possible to excite $\Delta m = 1$ or $\Delta m = 2$ coherences, respectively. The pulses are detuned from the excited state and resonant with the two-photon transition that couples two magnetic sublevels of the ground state as shown in Figure 27b. The timing diagram is shown in Figure 27c. The excitation creates a spatially periodic superposition (coherence grating) between the magnetic sublevels of the ground state. The grating, which has a period of $\sim \lambda/\theta'$, is probed by a read-out pulse along $\boldsymbol{k}_2$. The resulting MGFID signal is coherently scattered along $\boldsymbol{k}_1$ due to conservation of momentum. The grating dephases because of thermal motion of the atoms causing the MGFID to decay on a time scale of $\lambda/\theta' u$, where u is the most probable speed associated with the Maxwell–Boltzmann velocity distribution. The dephasing time of the MGFID can therefore be used to infer the temperature of the sample.

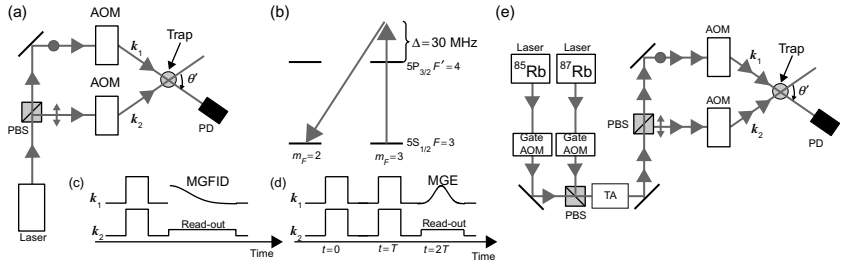

Figure 27 (a) Experimental schematic; $\theta' \sim 10$ mrad. PBS = Polarizing beam splitter, PD = photodetector, AOM = acousto-optic modulator. (b) Level diagram in ^{85}Rb showing two-photon excitation with orthogonal linear polarizations; Δ is the one-photon detuning. (c), (d) Timing diagram for the MGFID and MGE experiments respectively. (e) Experimental schematic for precision measurements.

The effect of Doppler dephasing can be eliminated by observing magnetic grating echo (MGE) signals. The MGE is observed using a second set of excitation pulses at $t = T$ to rephase the coherence grating as in Figure 27d. The second pulse modifies the time-dependent coefficients that describe the coherent superposition of magnetic sublevels so that the grating reforms at $t = 2T$. This effect is analogous to the reversal of the Doppler phases of individual atoms in a traditional two-pulse photon echo experiment (Rotberg et al., 2007). In the absence of decoherence due to collisions and background light, the MGE amplitude should decay on a time scale determined by the transit time of atoms through the laser beams as shown in Kumarakrishnan et al. (1998b).

The excitation and read-out pulses are derived using acousto-optic modulators (AOM) and intersect at a small angle in a sample of laser-cooled atoms as in Figure 27a. A single tapered amplifier (TA) is used to generate the trapping light for both ^{85}Rb and ^{87}Rb isotopes. Another TA is used to generate the excitation beams as in Figure 27e. In order to minimize the effect of time-varying magnetic fields, the ^{85}Rb and ^{87}Rb traps are spatially overlapped. This allows the MGFID signals from both isotopes to be recorded $\sim$1 ms apart. The trapping chamber is made of pyrex to minimize magnetized materials near the MOT and to avoid the effects of eddy currents. Magnetic field canceling coils suppress magnetic gradients to the level of 10^{-5} G/cm. The experiment also relies on active feedback to stabilize magnetic fields. In this manner, variations of static fields are limited to $\sim$10 μG and fluctuations in AC fields are reduced to $\sim$30 μG over the time scale of the measurement. At the start of the experiment, both ^{85}Rb and ^{87}Rb atoms are simultaneously loaded from background vapor into the dual isotope MOT. After turning off the magnetic field gradient of the MOT, both isotopes are cooled in an optical molasses for $\sim$10 ms to temperatures of $\sim$30 μK. The excitation pulses ($\sim$5 μs in duration) and read-out ($\sim$1 ms in duration) for each isotope are separately switched on in a random sequences. The signal is recorded by a gated photomultiplier tube or a balanced heterodyne detector that is turned off at the time of the excitation pulses.

The Doppler dephasing time can be measured by mapping out the MGFID using a short intense read-out pulse with a variable delay with respect to the excitation pulse in the absence of magnetic fields using a single isotope. Figure 28a shows the MGFID from a sample of laser-cooled ^{85}Rb atoms optically pumped into a single magnetic sublevel. The MGFID is fitted to a Gaussian form predicted by theory (Dubetsky & Berman, 1994) and consistent with previous observations (Kumarakrishnan et al., 1998a,b). The time constant of the decay, τ, and the angle between the excitation beams are used to extract the most probable speed (and temperature) associated with the Maxwell–Boltzmann distribution of the cloud along the direction $\boldsymbol{k}_1 - \boldsymbol{k}_2$. Figure 28b shows the radius of the sample along $\boldsymbol{k}_1 - \boldsymbol{k}_2$ measured using a CCD camera as a function of delay time

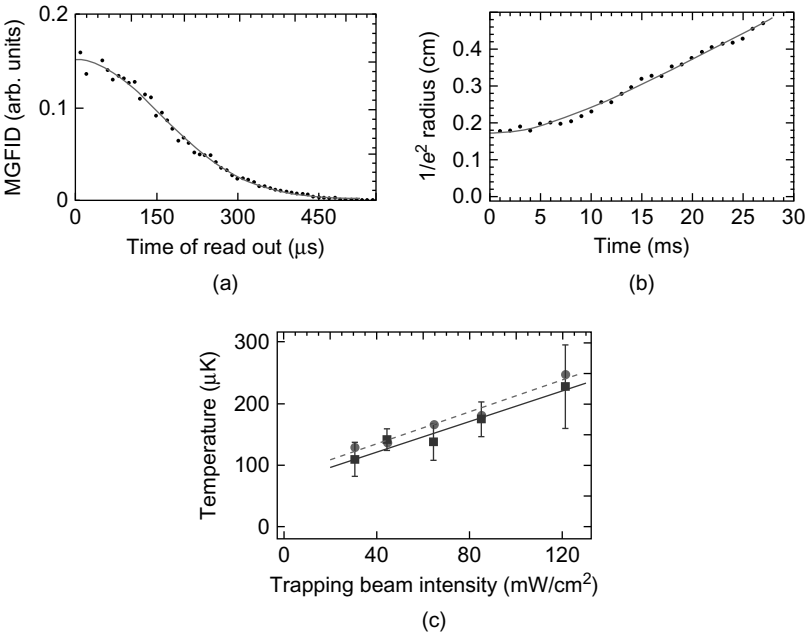

Figure 28 (a) Decay of the MGFID (circles) as a function of time for an angle $\theta' = 6.6$ mrad. The decay time extracted by fitting the data to the equation $Ae^{-(t/\tau)^2} + C$ (solid line) is $\tau = 221\,\mu$s. The most probable speed, given by $u = 2/(k\theta'\tau)$, is 0.17 m/s. The corresponding temperature is $\mathcal{T} = 149.2\,\mu$K. (b) Ballistic expansion of the cloud as a function of time (circles). u is extracted by fitting the cloud radius $R(t)$ to a hyperbola $R(t) = \sqrt{R_0^2 + (ut)^2}$ (solid line), where R_0 is the initial cloud radius. (c) Temperature of the cloud measured by the CCD camera (circles) and the temperature measured from the decay time of the MGFID (squares) as a function of total trap laser intensity. Linear fits are represented by a dashed line with $1.3I + 82.6\,\mu$K and a solid line with $1.2I + 73.3\,\mu$K. Here, I is the trapping laser intensity in mW/cm^2.

with respect to the turn off of the trapping lasers (Vorozcovs et al., 2005). The temperature is extracted by fitting the data to a hyperbola using the measured cloud size and the delay time. A comparison of the temperature measurements using these two techniques is shown in Figure 28c. The temperature was varied by changing the total trap laser intensity. It is clear that the temperature measurements show good agreement within experimental error.

6.2 Effect of a Uniform Magnetic Field on the MGFID

It is known that the Zeeman shift between magnetic sublevels causes temporal oscillations within the envelopes of these signals at multiples of ω_L (Kumarakrishnan et al., 1998a). Chan et al. (2008) presents an analytical

calculation that predicts the functional form of the Larmor oscillations in the the MGFID in arbitrary static magnetic fields for excitation pulses with both orthogonal linear and circular polarizations.

The theoretical treatment is based on a rotation matrix approach (Edmonds, 1996; Rochester & Budker, 2001; Shore, 1990) in which the effect of the magnetic field can be described as a time-dependent rotation of the atomic system about the quantization axis. The evolution of $\Delta m = 1$ and $\Delta m = 2$ coherences in a magnetic field resembles the evolution of dipole and quadrupole moments of the atom (effects termed alignment and orientation respectively) in an irreducible tensor basis. On the basis of the treatment in Rochester and Budker (2001), the probability of the atom being in a specific coherent superposition is defined by $\langle F\, m \mid \rho \mid F\, m' \rangle$, where F and m refer to the total angular momentum and magnetic quantum numbers of the ground state, respectively, and ρ is the atomic density matrix. To calculate the probability that an atom will be in a particular atomic state in the presence of a magnetic field, we apply the rotation operator to align the quantization axis as defined by the laser polarizations with the quantization axis as defined by the magnetic field. This involves rotating the atomic coordinate system through the Euler angles (α,β,γ) that describe rotations about each of the axes. The rotated density matrix is given by

$$\rho_{m\,m'}(\theta,\phi) = \left[D^{-1}(\phi,\theta,0)\rho D(\phi,\theta,0)\right]_{m\,m'}, \tag{54}$$

where

$$D(\alpha,\beta,\gamma) = \exp\left(i\gamma\hat{J}_z\right)\exp\left(i\beta\hat{J}_y\right)\exp\left(i\alpha\hat{J}_z\right). \tag{55}$$

In Equation (54), θ and ϕ represent the polar and azimuthal angles in the new coordinate system. The rotation generates a surface such that the distance from the origin to a point on the surface defined by (r, θ, ϕ) is proportional to the probability of finding the system in a particular state.

The rotation matrix in Equation (55) can be evaluated for the level structure of interest (specific angular momentum $\hat{\boldsymbol{J}}$). We apply the rotation operator D to the density matrix and evolve the system in time using the Hamiltonian for the magnetic interaction. The time-dependent atomic density matrix element $\rho_{m\,m'}(t)$ is then transformed into an irreducible tensor basis $\rho^K_Q(t)$ using the transformation

$$\rho^K_Q = \sum_{m,m'}(-1)^{F-m'}\left\langle F,m;F,-m' \,\middle|\, K,Q\right\rangle \rho_{m\,m'}, \tag{56}$$

where $\langle F,m;F,-m' \mid K,Q\rangle$ is a Clebsch–Gordan coefficient. It is particularly convenient to write the atomic density matrix in this basis, since the

coherence that is established by the laser pulses is proportional to the tensor elements ρ_Q^K. The inverse transformation allows us to predict the state of the system in the m basis and is given by

$$\rho_{mm'} = \sum_{K=0}^{2F} \sum_{Q=-K}^{K} (-1)^{F-m'} \langle F, m; F, -m' \mid K, Q \rangle \, \rho_Q^K. \tag{57}$$

Since the time dependence of the density matrix in Equation (54) is given by

$$\dot{\rho}_{m\,m'}(\theta, \phi, t) = -\frac{i}{\hbar} \left[\hat{H}, \rho(\theta, \phi, t) \right]_{m\,m'}. \tag{58}$$

where $\hat{H} = -g_J \mu_B \boldsymbol{B} \cdot \boldsymbol{J}$, the solution to Equation (58) is

$$\rho_{m\,m'}(\theta, \phi, t) = \left[e^{-i\hat{H}t/\hbar} \rho(\theta, \phi, t = 0) e^{i\hat{H}t/\hbar} \right]_{m\,m'}. \tag{59}$$

We calculate ρ_Q^K (defined by Equation (56)) as a function of time for the $F = 3$ manifold in ^{85}Rb for excitation by Lin⊥Lin and $\sigma^+\sigma^-$ pulses. The relevant tensor elements are ρ_1^1 and ρ_2^2, respectively. Correspondingly, the time dependence of the MGFID in a magnetic field is given by

$$\rho_1^1(t) \propto \cos(\omega_L t) + \sin(\eta) + i \cos(\eta) \sin(\omega_L t). \tag{60}$$

$$\rho_2^2(t) \propto e^{-2i(\omega_L t + \eta)} \left[i \left(1 - e^{-i\eta} \right) + e^{i\omega_L t} + e^{i(\omega_L t + \eta)} \right]^4. \tag{61}$$

Here, we use η to specify the angle between the magnetic field and the quantization axis of the atoms as defined by the laser polarizations. It is evident that the signals exhibit Larmor oscillations because of the magnetic field. The precision measurement of the g-factor ratio relies on a determination of the ratio of Larmor frequencies in two rubidium isotopes under such conditions. In order to compare predictions to experimental results, Equations (60) and (61) are multiplied by a Gaussian decay to model Doppler dephasing.

The temporal evolution of the coherences is illustrated in Figure 29 which shows the MGFID from laser-cooled ^{85}Rb atoms. The entire decay was recorded using a long weak read-out pulse. A heterodyne technique was used to determine the in-phase and quadrature components of the signal.

Figure 29 shows the signals for Lin⊥Lin and $\sigma^+\sigma^-$ excitation with the uniform magnetic field at an angle $\eta = \pi/4$ with respect to the quantization axis. For Lin⊥Lin excitation, the MGFID is proportional to the irreducible tensor element ρ_1^1 predicted by Equation (60). For $\sigma^+\sigma^-$ the

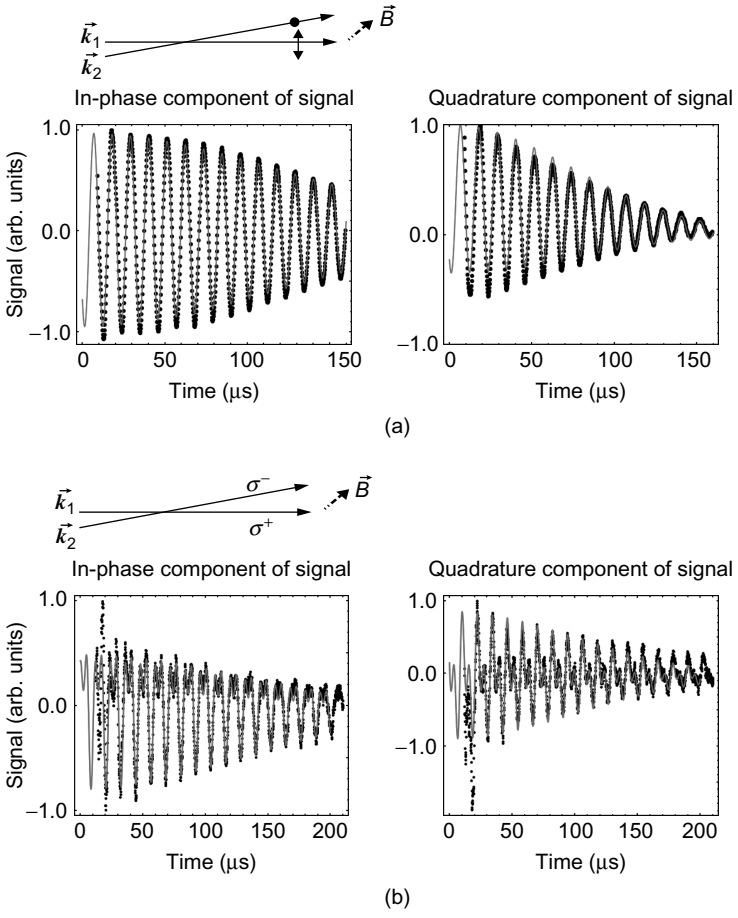

Figure 29 Evolution of the in-phase and quadrature parts of the MGFID in a sample of cold atoms. (a) The excitation pulses have orthogonal linear polarizations and the magnetic field is directed at an angle of $\pi/4$ with respect to the polarization of k_2. (b) The excitation pulses have opposite circular polarizations with the direction of the magnetic field at an angle of $\pi/4$ to the direction of k_1. In both cases the excitation pulse widths were 2 μs, and the detuning was 40 MHz. The data are shown as dots and the solid lines are fits based on Equations (60) and (61).

MGFID is given by ρ_2^2 predicted by Equation (61). Data shown in Figure 29 exhibits excellent agreement with the fits based on Equations (60) and (61). The overall signal shapes and oscillation frequency are consistent with predictions. It is also clear that Larmor oscillations can be recorded over the entire signal dephasing time.

Figure 30 shows an example of single-shot measurements of the MGFID signals from the dual species MOT for Lin⊥Lin excitation. To determine

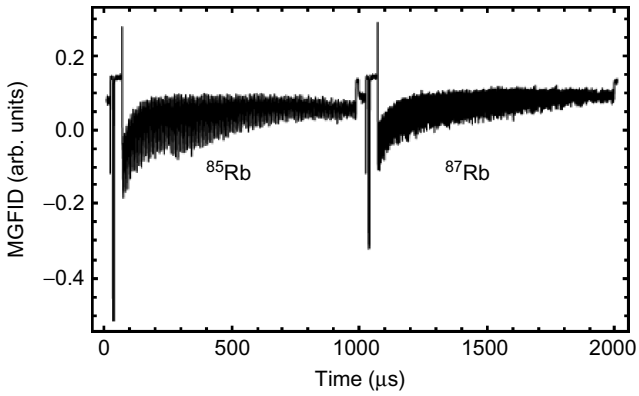

Figure 30 MGFID signals from a dual isotope MOT. The temporal separation of the signals is 1 ms.

the oscillation frequency, the data are fitted to a function based on Equation (60) with $\eta = 0$. This procedure can be used to extract the ratio of g-factors, which is taken to be the ratio of Larmor frequencies. The precision in the measured Larmor frequencies is 24 ppm and 16 ppm for ^{85}Rb and ^{87}Rb respectively. For a given set of experimental conditions (pulse power, duration, magnetic field, read-out pulse intensity, distribution of magnetic sublevel populations) the average value of the ratio is determined by averaging $\sim$100 repetitions. The major systemic effects that are being investigated include AC stark shifts associated with the read-out pulse, the Breit–Rabi correction due to the nonlinear variation of the Larmor frequency with magnetic field that causes the g-factor ratio to be dependent on the field, and magnetic sublevel population distributions that cause a variation in the Larmor frequencies of $\Delta m = 1$ coherences within the same ground-state manifold due to the Breit–Rabi effect.

6.3 Effect of a Uniform Magnetic Field on the MGE

The precision of the g-factor ratio can be improved by observing T dependent oscillations in the amplitude of the MGE signal. Such a measurement raises the exciting prospect of testing relativistic effects that have been predicted at the level of 100 ppb by Anthony and Sebastian (1994).

The rotation matrix approach described in Section 6.2 is clearly well suited to describing the MGFID in the tensor basis, since it gives analytical expressions for arbitrary magnetic field directions. In contrast, the evolution of the MGE is more complicated. It requires knowledge of the evolution of the magnetic sublevel populations and coherences during both excitation pulses as well as the evolution of the Doppler and Larmor

phases during the experiment. As a result, we use numerical simulations to model a system of rate equations (Berman, 1991; Berman et al., 1993) to describe the MGE and to understand this signal in a magnetic field.

An interesting prediction of the simulations is that the amplitude of the MGE envelope exhibits oscillations that depend on the Rabi frequencies of the excitation pulses and the magnetic field as a function of the time between excitation pulses. The amplitude of the MGE oscillates as a function of T with a characteristic frequency $\sqrt{(\chi^2/\Delta)^2 + \omega_L^2}$, where χ and Δ are the Rabi frequency and detuning of the excitation beams, respectively. This expression has the same form as the generalized Rabi frequency for a laser field interacting with a two-level atom (Allen & Eberly, 1987). The term χ^2/Δ characterizes the two-photon interaction and replaces the one-photon Rabi frequency. The two-photon detuning ω_L due to the Zeeman shifted magnetic sublevels levels replaces the one-photon detuning. Owing to the spatial variation in the Rabi frequency χ, the component of the MGE oscillation at frequency $\xi = \chi^2/\Delta$ averages out on a time scale of $\sim 1/\xi$ ($\sim$100 ns). As a result, it can be expected that the frequency of the T-dependent oscillations on suitably long time scales will be determined by ω_L. The results of simulations are consistent with expectations based on a derivation in the limit $\chi \ll \delta$, where δ is the two-photon detuning (Dubetsky & Berman, 1994). This treatment shows that the echo envelope oscillates as a function of T with frequency δ (which is analogous to ω_L). Since it should be possible to observe the MGE on a time scale comparable to the transit time of cold atoms through the region of interaction (several tens of milliseconds), it should be possible to use this signal to achieve a significant improvement in the precision with which the g-factor ratio can be determined. However, the time scale on which magnetic-field-induced oscillations in the amplitude of the echo envelope can be observed will be limited by the presence of magnetic field gradients. In the presence of a gradient, all the atoms that contribute to the signal have slightly different Larmor frequencies, depending on their spatial locations. As T increases, the oscillations from individual atoms get out of phase and cancel out as shown in Chan et al. (2008).

Figure 31 shows the amplitude of the MGE at $t = 2T$ as a function of T from laser-cooled ^{85}Rb atoms. These data were obtained using a short intense read-out pulse. To record MGE signals for small values of T, we used counter-propagating excitation pulses ($\boldsymbol{k}_1 \approx -\boldsymbol{k}_2$) so that durations of the MGFID and MGE envelopes are $\sim$1 μs. The data show that the effect of atomic recoil is significant for this geometry. The signal amplitude in Figure 31 shows the expected modulation at the atomic recoil frequency $\omega_q = \hbar q^2/2M$, where $\hbar \boldsymbol{q} = \hbar(\boldsymbol{k}_1 - \boldsymbol{k}_2)$ is the momentum transfer to the atoms from the laser fields and M is the atomic mass. The corresponding value of $\tau_q = \pi/\omega_q$ shown in Figure 31 is $\tau_q \sim 32$ μs. The Larmor

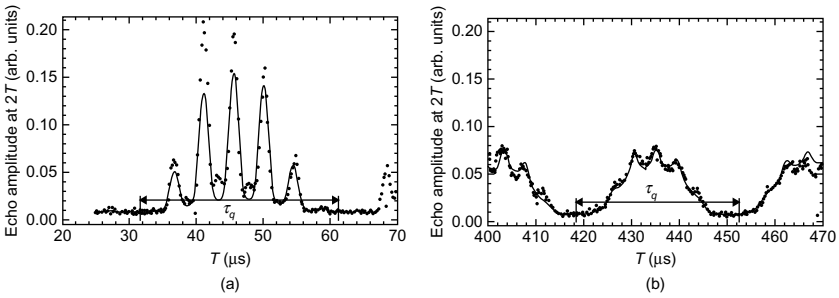

Figure 31 MGE signal intensity measured with a PMT (dots) using counter-propagating Lin⊥Lin excitation pulses in a laser-cooled sample. A magnetic field of $B \sim 0.25$ G is directed along the polarization direction of k_1. The first and second excitation pulses are 680 ns and 70 ns in duration, respectively. In addition to the T-dependent magnetic field oscillations, the signal is modulated at the atomic recoil frequency ($\omega_q = 96.95(4)$ rad/ms). The extracted value of ω_L from the fit (solid line) is consistent with the expected value.

frequency was determined to be $\omega_L = 110.395(15)$ kHz (∼100 ppm) from a fit based on Equation 26 in Beattie et al. (2008) with an additional $\cos^4(\omega_L T)$ term to account for the magnetic field oscillations. The value of ω_L was consistent with expectations based on the applied magnetic field. Both ω_q and ω_L were obtained from a single multiparameter fit to the data in Figure 31a and b.

Figure 31b shows that Larmor oscillations in the amplitude of the echo envelope cancel out for $T \sim 500\,\mu$s although the overall decay time of the signal is several milliseconds. This behavior is due to the presence of a magnetic field gradients of ∼0.05 G/cm due to the magnetized walls of a stainless steel vacuum chamber (Weel et al., 2006). Following the demonstration of transit-time-limited recoil experiments in the glass cell, we anticipate similar observations on time scales of ∼70 ms. As a result, it should be possible to utilize the MGE to improve the precision in the g-factor ratio measurements to ∼100 ppb. The main experimental challenge will be associated with the long-term stability of magnetic fields, since the time for acquiring a data set such as in Figure 31 is ∼1 hour.

7. COHERENT TRANSIENT EFFECTS

7.1 Introduction

In this section, we describe the suitability of the echo technique for precision measurements of radiative lifetimes of atomic excited states. The knowledge of atomic lifetimes is essential for a wide range of experiments in laser spectroscopy such as atom and ion trapping (Moehring

et al., 2006), trace gas analysis, and remote sensing. Precision measurements are also essential for testing quantum mechanical calculations of level structure (Blundell et al., 1991; Dzuba et al., 1989; Safronova et al., 2004).

Precision measurements of natural linewidths and atomic lifetimes have generally involved scanning a probe laser with a narrow linewidth or observing the decay of the atomic fluorescence using photon-counting techniques. The dominant systematic effects in these experiments are the contribution of laser linewidth and radiation trapping respectively. As a result, these experiments have required the development of sophisticated experimental setups. A prominent example is a measurement of the natural linewidth precise to $\sim$0.25% in a sample of velocity-selected laser-cooled Na atoms (Oates et al., 1996). This experiment utilized a laser with a linewidth of only a few kilohertz. Such lasers are accessible to only a small number of groups. An alternative technique for measuring the atomic lifetime with comparable precision involves exciting a sample of trapped atoms with a laser pulse and observing the fluorescence decay. Such an experiment requires specialized expertise to develop electronics for photon counting (Simsarian et al., 1998). Examples of other independent techniques include photo-association spectroscopy (McAlexander et al., 1996) in cold atoms and fast atomic-beam experiments (Volz & Schmoranzer, 1996; Young et al., 1994).

The widely established two-pulse photon echo technique is particularly well suited for precision measurements of atomic lifetimes because it is insensitive to the effects of radiation trapping and laser linewidth and is widely accessible to a large number of experimental groups. Although photon echoes have been used extensively to measure relaxation rates in atomic and molecular species (Patel & Slusher, 1968), collisional rates (Flusber et al., 1978), diffractive collisions (Forber et al., 1990), atomic level structure (Chen et al., 1980), and lifetimes in solids and doped crystals (Becker et al., 1988; Macfarlane & Shelby, 1981), it does not appear to have been used for atomic lifetime measurements.

Spin echoes (Hahn, 1950b) and photon echoes (Abella et al., 1965) are well understood and have been studied extensively over the past 60 years. In a typical photon echo experiment involving dilute atomic gases, a laser pulse is applied at $t = 0$ to create a coherent superposition of ground and excited states (Allen & Eberly, 1987). Owing to Doppler broadening, the superposition dephases with time. At $t = T$ a second pulse is applied and rephases the superposition so that dipole radiation occurs at $t = 2T$ (photon echo). The decay of the echo signal as a function of T can be used to measure various relaxation effects. The basic properties of a two-level atom and its interaction with an external electric field are based on the treatment in (Allen & Eberly, 1987; Cohen-Tannoudji et al., 1997, 1998). This treatment can be used to describe coherent transient effects such

as free induction decay and photon echoes using the semiclassical Bloch vector model.

In a typical photon echo experiment involving an inhomogeneously broadened sample, a $\pi/2$ pulse applied at $t = 0$ will rotate the Bloch vector associated with the macroscopic dipole moment to the uv-plane. Following the pulse, the Bloch vectors associated with the individual atoms will precess freely around the w-axis. Owing to Doppler broadening, the precession occurs with different rates for different atoms resulting in rapid dephasing of the macroscopic dipole moment (FID). It is possible to reverse the dephasing process after some time $t = T$ using a π-pulse. This creates a rephased dipole moment resulting in an echo at time $t = 2T$. A schematic representation of the process of echo formation is shown in Figure 32.

For a Doppler-broadened gas, in the absence of collisional dephasing, the echo intensity depends only on radiative decay. This dependence is given by

$$I = I_0 \exp\left(-\frac{2T}{\tau}\right). \tag{62}$$

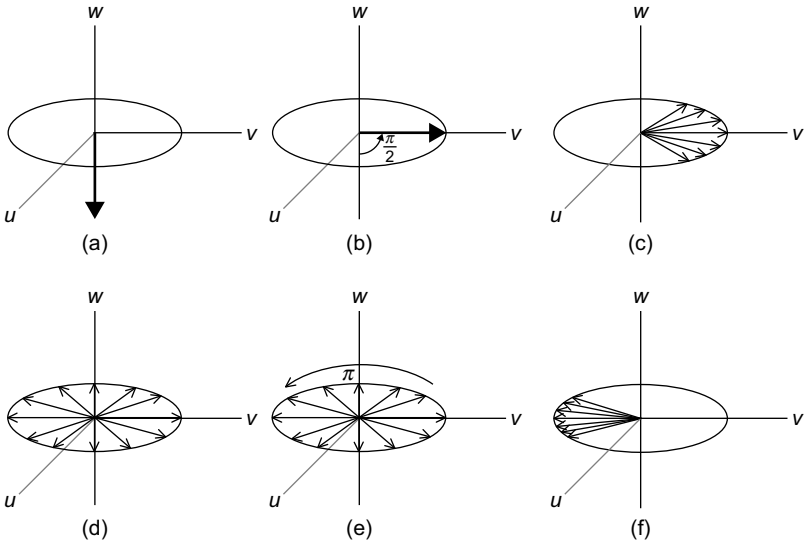

Figure 32 Bloch vector representation. (a) Macroscopic Bloch vector representing all atoms in the ground state. (b) Superposition state immediately after $\pi/2$-pulse. (c), (d) Bloch vector dephasing. (e) Inversion due to π-pulse. (f) Bloch vector rephasing (photon echo).

The laser linewidth and the temporal shape of the excitation pulses determine the velocity distribution that contributes to the echo formation. Although these factors affect the signal strength, they do not affect the decay time constant, τ. Similarly, the intensity, temporal shape of the excitation pulses and sample density affect the echo amplitude and pulse propagation but not the decay time constant. Spontaneous emission during the excitation pulses is also not expected to affect τ.

On the basis of Rotberg et al. (2007), we describe a measurement of the $5P_{3/2}$ excited state lifetime using two-pulse photon echoes in rubidium vapor. The measurement is precise to ~1% and agrees with the best measurement of atomic lifetime in Rb (Simsarian et al., 1998).

7.2 Experimental Setup and Results

The excited state lifetime is determined by measuring the exponential decay of the photon echo intensity as a function of the time T between the excitation pulses. The experiment relies on precisely timed and sufficiently short optical pulses generated from a CW laser using acousto-optic modulators (AOMs). The excitation pulses are on resonance with the $F = 3 \rightarrow F' = 4$ transition in ^{85}Rb or $F = 2 \rightarrow F' = 3$ transition in ^{87}Rb. The echo signal is detected using a heterodyne detection technique used in many experiments involving cold atoms. The signals are generated in a 7-cm-long vapor cell containing a natural abundance of rubidium isotopes (~72% of ^{85}Rb and ~28% of ^{87}Rb). The vapor density, which can be varied by heating the cell, is monitored by measuring the absorption of a probe laser scanned across the atomic resonance.

The experimental setup is shown in Figure 33. Short pulse generation was achieved by focusing and spatially filtering light into two AOMs operating at 260 MHz and 400 MHz. As a result, the resonant excitation pulses have temporal Gaussian profiles with a full width at half maximum (FWHM) of ~20 ns and an on/off ratio of $\sim 10^6 : 1$. The heterodyne detection technique involves use of a local oscillator (LO) derived from a separate 260 MHz AOM as shown in Figure 33. The echo signal is combined with the LO on a beam splitter and detected as a 400 MHz beat note using photodiodes. The echo decay time can be measured by varying T and recording the echo amplitude by averaging 128 repetitions as shown in Figure 34a. To acquire the background for each data point, the experiment is repeated with the first pulse turned off. The oscilloscope traces shown in Figure 34a are squared and integrated to obtain the echo intensity. The echo intensity is expected to show an exponential decay as a function of $2T$ (see Equation [62]). The measurement of the lifetime is achieved by fitting the signal as a function of $2T$ to this model, as shown in Figure 34b.

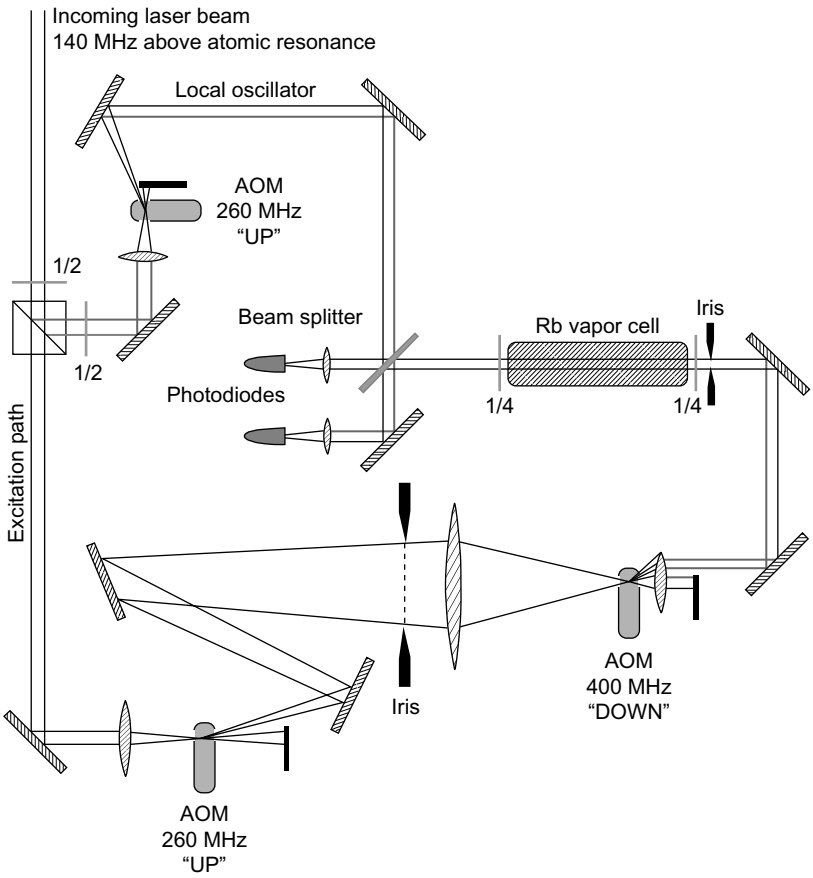

Figure 33 The optical layout. 1/2 and 1/4 represent $\lambda/2$ and $\lambda/4$ wave plates respectively.

7.3 Discussion

Systematic effects on the echo decay time constant were investigated by varying several parameters affecting the echo intensity. These include the intensity and durations of the excitation pulses, cell temperature, strength of a quantizing magnetic field, and the beam diameter of the excitation pulses. Other effects such as collisional dephasing and decoherence due to background light can be ruled out on the time scale of the experiment on the basis of experimental conditions. As shown in Rotberg et al. (2007), these parameters did not produce systematic effects on the measured echo decay time. The final value for the lifetime was determined on the basis of a double-blind study by averaging 67 equally weighted data sets distributed between both ^{85}Rb and ^{87}Rb isotopes. The distribution of

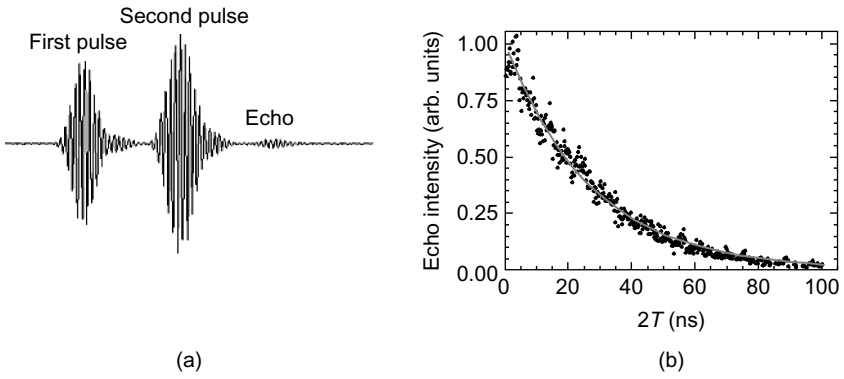

Figure 34 (a) Oscilloscope trace of excitation pulses and the photon echo using heterodyne detection. (b) Decay of the echo intensity as a function of $2T$. Data are fitted to an exponential function that results in a lifetime measurement of $\tau = 25.25 \pm 0.38$ ns.

points is a Gaussian with an average value $\tau = 26.47 \pm 0.30$ ns. The quoted error represents the standard deviation of the mean (1σ uncertainty). The measurement has a precision of 1.14% and is in agreement at the level of 1σ with the best measurement in rubidium (Simsarian et al., 1998) (26.20 ± 0.09 ns).

The theoretical prediction for the echo intensity as a function of the excitation pulse area is well understood in the absence of spontaneous emission (Allen & Eberly, 1987). Since the experiment involved pulse widths that are comparable to the lifetime and since the excitation beams have a finite spatial profile, the dependence of the signal intensity is expected to differ from that in the ideal case. The theory must be modified to include the effect of spontaneous emission and Gaussian pulse shapes (Allen & Eberly, 1987). The effect of the spatial profile can also be taken into account by assigning a Gaussian distribution of Rabi frequencies and averaging the response over the profile. Results based on numerical simulations (Rotberg et al., 2007) show that the maximum echo intensity is obtained when the ratio of the excitation pulse areas is $\sim$1.2. In contrast, for the ideal case, the theory ignores the effect of spontaneous emission and the temporal and spatial profiles of the excitation beams so that this ratio is predicted to be 2.

In summary, the results suggest that improved measurements precise to $\sim$0.25% are attainable through additional data acquisition and studies of systematic effects. Improvements are expected to include optical pumping into a single magnetic sublevel to achieve an increase in the signal-to-noise ratio and use of shorter excitation pulses to minimize the effects of spontaneous emission. The work can also be extended to the $5P_{1/2}$ transitions so that comparisons with previous measurements (such as in

Young et al. [1994]) are possible. The absence of systematic effects and the relative simplicity of this technique suggest that the photon echo technique may be well suited for precision measurements in atomic and ionic transitions that have relatively large oscillator strengths.

8. SUPERFLUORESCENCE IN COLD ATOMS

8.1 Introduction

Previously described experiments on single-state atom interferometers and magnetic sublevel coherences have relied on the coherent transient response of a sample of laser-cooled atoms for signal detection. It is well known that the radiation from a coherently driven sample containing N_{ex} excited atoms will exhibit an N_{ex}^2 enhancement in peak intensity in the far field. It is interesting that this well-known signature is shared by two distinct collective effects termed superfluorescence (SF) and superradiance (SR). In this section, we review observations of both effects in a sample of laser-cooled atoms (Paradis et al., 2008).

In SF, a sample of incoherently excited atoms can be locked in phase to produce coherent emission by spontaneously emitted photons emitted into preferred electromagnetic modes (Gross & Haroche, 1982). SF is characterized by a burst of radiation that has some of the features of radiation from a phased array of dipoles (Rehler & Eberly, 1971). For SR (Dicke, 1954), the direction of emission is defined by the initial phases of excitation pulses and phase-matching conditions (Schneble et al., 2003). In contrast, the shape of the sample defines the directions of SF emissions (Bonifacio & Lugiato, 1975).

The ideal conditions for SF can be achieved if the propagation time for light to travel through the sample, τ_e, satisfies the condition $\tau_e < \tau_r$, where $\tau_r = (N_{ex}\Gamma\mu)^{-1}$ is the dipole coupling time for the evolution of a macroscopic dipole moment (Bonifacio & Lugiato, 1975). Here, Γ is the rate of spontaneous emission for a single atom and μ is the diffraction solid angle at the SF wavelength, which defines the fraction of spontaneously emitted photons that are amplified. Under these conditions, spontaneously emitted photons from one end of the sample can influence the collective evolution of the entire sample. In this regime, the SF peak intensity scales as N_{ex}^2 and the pulse width scales as N_{ex}^{-1} to conserve energy. If $\tau_e > \tau_r$, the emission of the system can be regarded as the incoherent sum of coherent emissions from a number of subregions within the sample that evolve independently (Arecchi & Courtens, 1970; Gross & Haroche, 1982; Kumarakrishnan & Han, 1998; Kumarakrishnan et al., 2005).

SF is also characterized by a delay time with respect to the excitation pulse. Under conditions in which $\tau_e < \tau_r$, a fully quantum-mechanical model for SF initiation predicts that the delay time for SF with respect

to the excitation pulse is given by (Polder et al., 1979):

$$\tau_d = \frac{\tau_r}{4}\left[\ln\left(\sqrt{2\pi N_{ex}}\right)\right]^2. \tag{63}$$

Since τ_d is proportional to τ_r, it approximately scales as N_{ex}^{-1}.

The threshold number of atoms N_T required for SF is achieved when $\tau_r = T_2$, where T_2 is the dephasing time of the system. For a Doppler-broadened vapor $N_T \sim 10^{10}$ (Gibbs et al., 1977), whereas it is typically $\sim 10^5$ for the case of laser-cooled atoms because of the negligible effect of the Doppler broadened linewidth $\Gamma_D \lesssim 1\,\text{MHz}$. Therefore, SF can become a dominant channel for relaxation and observations of SF from atom traps can be recorded with a high signal-to-noise ratio. Studies of SF scaling laws can serve as useful diagnostic tools for studying various dephasing processes, such as cold Rydberg atom interactions (Gross & Haroche, 1982). Another interesting aspect of working with atom traps is that it is relatively straightforward to change the shape of the sample and to observe the enhancement of SF along the preferred axes of the atomic cloud. Apart from realizing the threshold atom number, it is further necessary that $\tau_d < \tau_n$, where τ_n is the natural radiative decay time associated with the excited state. In some cases (Kumarakrishnan & Han, 1998), effects such as radiation trapping can extend the effective lifetime of the excited state permitting SF to evolve even from rapidly decaying atomic states.

SF has been extensively studied in atomic gases to understand its scaling laws (Gibbs et al., 1977), effects of pulse propagation (Skribanowitz et al., 1973), quantum fluctuations (Gross & Haroche, 1982; MacGillivray & Feld, 1985; Vrehen et al., 1982), and dephasing processes (Maki et al., 1989; Schuurmans, 1980). SF has also been studied as an amplifier of quantum noise, since peak heights, pulse widths, and delay times exhibit characteristic fluctuations because of the stochastic nature of SF initiation (Glauber & Haake, 1976; Haake et al., 1979; Raymer & Walmsley, 1990).

In recent studies (Paradis et al., 2008), we have observed SF from spherical and cigar-shaped clouds of laser-cooled Rubidium atoms. The atomic system is excited to the $5D_{5/2}$ level from the $5S_{1/2}$ ground state via two-photon excitation through the intermediate $5P_{3/2}$ level as shown in Figure 35. The evolution of the system from the $5D_{5/2}$ level through the $6P_{3/2}$ level to the $5S_{1/2}$ ground level is monitored by time-resolved measurements of the light emitted on the $6P \rightarrow 5S$ transition at 420 nm. The time delays for the 420-nm radiation scaled as $\sim N^{-1}$, where N is the atom number. However, the delays are much smaller than expectations for uncorrelated cascade fluorescence. Since N is significantly smaller than the threshold number for SF on the 420-nm transition and larger than the threshold number for the $5D \rightarrow 6P$ transition at 5.2 μm, our observations suggest that rapid de-excitation of the 5D to the 6P level via SF

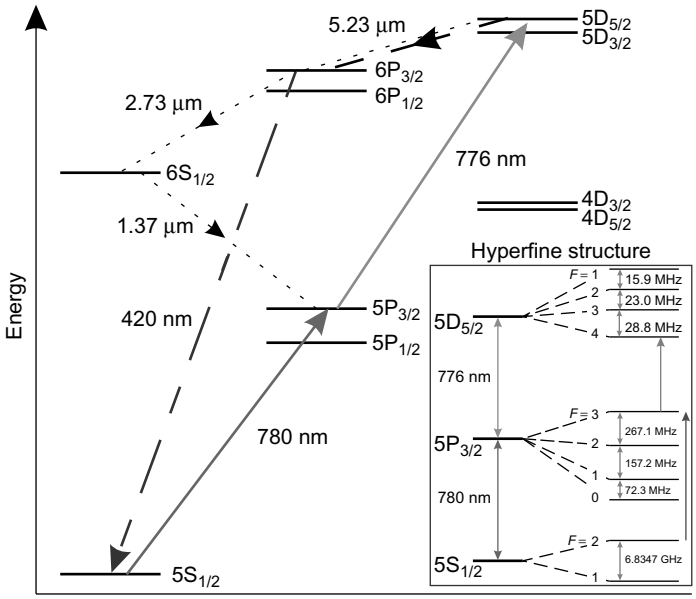

Figure 35 Rubidium 87 level diagram: the solid lines represent excitation pulses, and the dashed lines correspond to SF emissions pertaining to this work. The dotted lines represent the expected SF cascade for incoherent excitation. The radiative lifetimes of the $5D_{5/2} \rightarrow 6P_{3/2}$ and the $6P_{3/2} \rightarrow 5S_{1/2}$ transitions are 690 ns and 357 ns, respectively. The total radiative lifetimes of the $5D_{5/2}$ and $6P_{3/2}$ states are 241 ns and 109 ns, respectively. These lifetimes are based on Arimondo et al. (1977), Sansonetti (2006). The hyperfine structure of the 5D state shown in the inset was measured in Grove et al. (1995).

at 5.2 μm triggered SR-like emissions at 420 nm. This inference is supported by the observed time delays for the 420-nm emission that agree with SF time-delay estimates for the 5.2-μm transition. Pronounced variations in the directionality of of the 420-nm radiation were also observed by changing the shape of the sample. For spherical clouds, the emission is isotropic, whereas for cigar-shaped clouds, it is highly anisotropic. Along the long axis of cigar-shaped atom clouds, it is possible to observe both triggered emission and incoherent cascade fluorescence as temporally well-resolved peaks in the detected signal. The triggered emission is highly concentrated along a direction in between the directions of the two almost parallel excitation beams, which is a well-known characteristic of SR-like emission.

The experiment showed that the evolution of the system depended critically on whether the excitation is coherent or incoherent. As shown in Bowden and Sung (1978), avoiding coherent excitation imposes a particularly restrictive condition on pumping. If the rubidium system can be excited without any initial coherence between the 5S and 5D states, the

system can be expected to decay through a multistep SF cascade involving the 6P → 6S (2.7 μm) and 6S → 5P (1.3 μm) transitions shown in Figure 35. In contrast, if there is an initial coherence between the 5S and 5D states, the system is expected to decay through SF on the 5D → 6P (5.2 μm) transition and triggered SF on the 6P → 5S (420 nm) transition—a process referred to as "Yoked SF" (Brownell et al., 1995; Lvovsky & Hartmann, 1999; Lvovsky et al., 2002).

8.2 Experimental Details

A schematic of the experimental setup is shown in Figure 36. Light from an external-cavity diode laser (ECDL) is used for both the MOT beams on the $5S_{1/2}$, $F = 2 \rightarrow 5P_{3/2}$, $F = 3$ transition in ^{87}Rb and the first excitation beam for the SF experiment (∼30 MHz above the MOT transition).

Another ECDL is used to produce ∼50 mW of 776-nm light. Beams derived from the locked 780-nm laser and the 776-nm laser are counter propagated through a rubidium vapor cell at room temperature. The inherently Doppler-free two-photon transition resonances associated with the $5D_{5/2}$ hyperfine levels can be observed by measuring the absorption of 776-nm light in the cell. The 776-nm laser is stabilized by means of side-locking to the $5P_{3/2}$, $F = 3 \rightarrow 5D_{5/2}$, $F = 4$ absorption resonance. This laser also produces the light for the second excitation beam for the SF experiment, which is ∼30 MHz below the $5P_{3/2}$, $F = 3 \rightarrow 5D_{5/2}$, $F = 4$ transition.

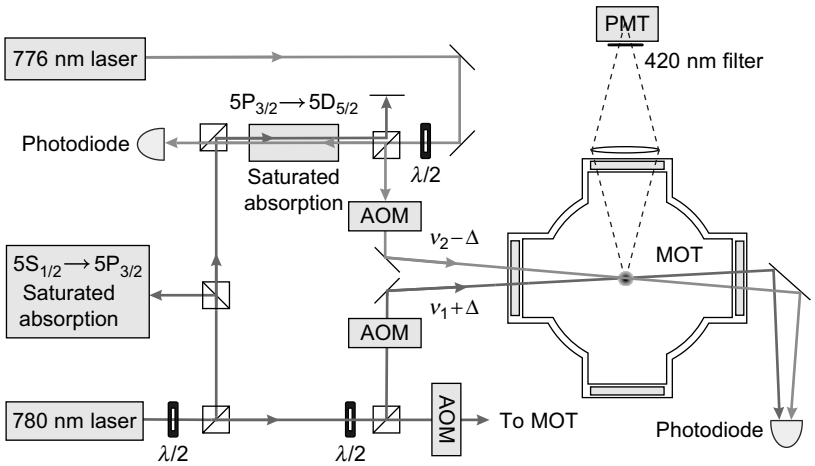

Figure 36 Diagram of experimental setup. SF emissions at 420 nm can be measured both perpendicular to and along the direction of the excitation pulses. (ν_1 denotes the frequency of the $5S_{1/2}$, $F = 2 \rightarrow 5P_{3/2}$, $F = 3$ transition, and ν_2, that of the $5P_{3/2}$, $F = 3 \rightarrow 5D_{5/2}$, $F = 4$ transition).

8.3 Results and Discussion

The ground-state atom number, N, was varied from $\sim 10^7$ to 10^9 by changing the loading time of the MOT. The observed emissions were found to be sensitive to the delay time between the two excitation pulses. One limiting case is when the lower-transition pulse peaks before the upper-transition pulse—referred to as sequential excitation. Another limiting case occurs when the upper-transition pulse peaks before the lower-transition pulse; this case is referred to as Stimulated Raman Adiabatic Passage (STIRAP) (Gaubatz et al., 1990). In both cases, a significant fraction of the ground-state population was transferred to the 5D state. We estimate a typical $5S \rightarrow 5D$ excitation efficiency of $\sim 50\%$ on the basis of the photon yield observed on the $6P \rightarrow 5S$ decay channel and on simulations of the excitation process.

We first describe time-resolved measurements of the 420-nm emission on the transition $6P_{3/2} \rightarrow 5S_{1/2}$ along the long axis of cigar-shaped atom clouds. Each curve in Figure 37 represents the emission intensity versus time for a distinct ground-state atom number, N. This atom number

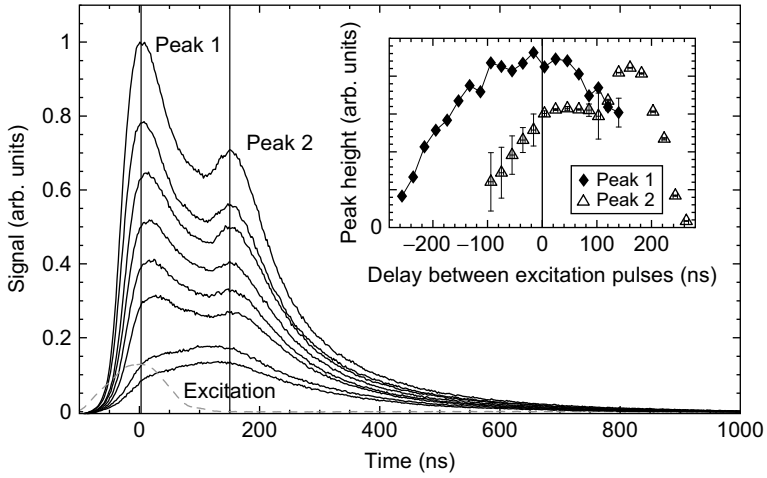

Figure 37 Time-resolved SF detected along the long axis of cigar-shaped atom clouds for various ground-state atom numbers, N. The excitation pulses are overlapped, and time $t = 0$ corresponds to the center of the excitation pulses. N increases from the bottom to the trop curve. The dashed curve indicates the time-dependence of the excitation pulses. The inset shows the height of the two maxima observed in the time-resolved emission signals (peak 1 and peak 2) for a fixed number of atoms, as a function of the delay time between the two excitation pulses. (Delay time < 0 corresponds to STIRAP excitation pulse ordering, while delay time > 0 corresponds to sequential excitation pulse ordering.)

is varied by changing the loading time of the MOT. The steady-state MOT fluorescence is monitored using a calibrated photodetector. N is determined from the measured photocurrent, the solid angle subtended by the detector, the total intensity of the MOT beams, and the detuning of the MOT beams from resonance. It is assumed that the MOT fluorescence is isotropic.

It is evident in Figure 37 that for a large N two time-resolved peaks occur. The time delay of the second peak (peak 2) remains unchanged. We interpret peak 2 as being due to cascade fluorescence. To support this interpretation, we have modeled the level system shown in Figure 35 using rate equations for atomic populations. In the simulation, a laser pulse with a Gaussian envelope (FWHM $\sim$200 ns) excites atoms from the 5S to the 5D level. The simulation shows that the 420-nm emission resulting from uncorrelated decay peaks at a delay time of $\sim$200 ns. This predicted delay of the cascade fluorescence peak matches peak 2 in Figure 37 reasonably well.

The first of the peaks in Figure 37 (peak 1) shows the essential characteristic of SF, namely a decreasing time delay with increasing N. In accordance with this interpretation, it is also observed that peak 1 increasingly dominates peak 2 as N increases. For large atom numbers, the peak 1 practically coincides in time with the excitation pulses, shown as a dashed line in Figure 37. This observation indicates that the 5D level is regeneratively pumped while the SF emission occurs (Gross et al., 1976).

The inset in Figure 37 shows the peak heights of the time-resolved emissions as a function of the delay between the excitation pulses for a fixed atom number ($N \approx 3 \times 10^8$). Negative pulse delays correspond to STIRAP excitation, where the 776-nm pulse precedes the 780-nm pulse, while positive pulse delays correspond to sequential excitation. The SF emission in peak 1 is dominant in the STIRAP regime and a large part of the sequential regime. The cascade fluorescence (peak 2) dominates for sequential excitation-pulse ordering with pulse delays larger than about $+100$ ns.

Estimates based on Equation (63), assuming the largest atom numbers available in our experiment, show that SF should occur on the $5D \rightarrow 6P$ transition, while conditions are below the SF threshold for the $6P \rightarrow 5S$ transition. Therefore, for the higher atom numbers (see Figure 37) SF on the $5D \rightarrow 6P$ transition is expected to rapidly populate the 6P level, leading to a rapid onset of 420-nm emission, as observed for peak 1. The 420-nm emission appears to be SF as well, as evidenced by the presence of two peaks in Figure 37, the short duration of the emission peak 1 (which is of the order, or less than the 6P lifetime), and the high directionality of the 420-nm emission for cigar-shaped clouds. As the conditions in our experiment are below threshold for SF on the $6P \rightarrow 5S$ transition, the

observed (apparently superfluorescent) emission on that transition must be attributed to triggered SF (Lvovsky & Hartmann, 1999; Lvovsky et al., 2002) that results from coherence between the 5S and 5D state amplitudes generated during excitation.

We now compare the time delays of the emission peaks observed for both cigar-shaped and spherical atom clouds. Figure 38 shows the time delays as a function of N for peak 1 (solid diamonds) and peak 2 (empty diamonds) for observation along the long axis of the cigar-shaped cloud. The delays are measured with respect to the peak of the excitation pulses (with 780-nm and 776-nm pulses temporally overlapped). A fit to the data for peak 1 (solid line) establishes that the SF emission exhibits the expected N^{-1} variation, with no fit offset. The dashed line shows the expected SF delay for 5.2-μm emission, for the same range of N, calculated using Equation (63) based on the measured trap parameters. Although the two curves are in excellent agreement, we note that there are systematic uncertainties with the measured trap parameters, at the level of $\pm 10\%$. Nevertheless, it is clear that the predicted time delay for the 5.2 μm occurs on the same

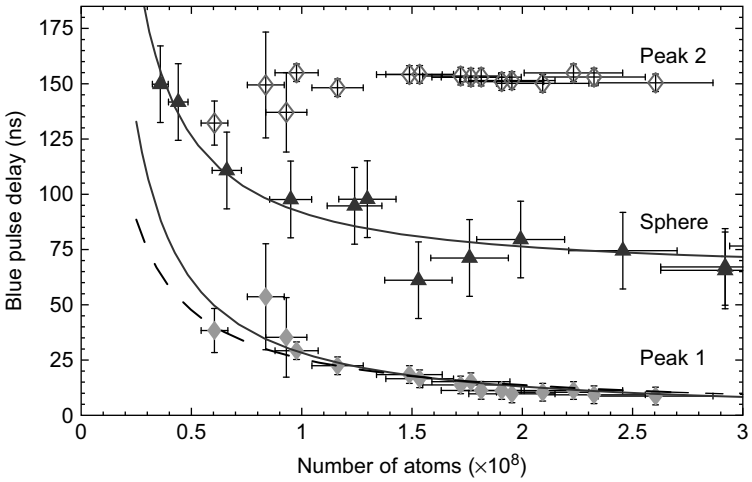

Figure 38 Delay time of SF versus number of atoms. The delays marked peak 1 (solid diamonds) and peak 2 (empty diamonds) correspond to temporally resolved peaks, as shown in Figure 37, measured along the long axis of the cigar-shaped cloud. Delays for the spherical trap are shown with triangles. For the case of the cigar and the sphere, the experimental data are fitted with functions of the type $aN^{-x} + b$ (with fit parameters a, b, and x), shown as solid lines. The fits show that the delays scale as the expected, with $x = (1.12 \pm 0.16)$ for the cigar and $x = (1.17 \pm 0.14)$ for the sphere, respectively. The offset b is zero for the cigar, and $\sim$70 ns for the sphere. The dashed line shows the predicted 5.2-μm delay, calculated on the basis of Equation (63) using measured cloud parameters. Numerical simulations for cascade fluorescence suggest that peak 2 should occur at 174 ns.

time scale as the 420-nm SF. This indicates that the 420-nm emission is triggered by the presence of the 5.2-μm emission, confirming the results in Lvovsky and Hartmann (1999). The data also show that there is no variation in the delay time for peak 2, consistent with expectations for cascade fluorescence. The discrepancy between the observed delay (∼150 ns) and the predicted delay for cascade fluorescence (174 ns for an excitation FWHM of 114 ns) can be attributed to the uncertainty in the degree of overlap between excitation pulses.

Similar data for the time delay of emission from the spherical trap (triangles) are also shown in Figure 38. A fit (solid line) establishes that the emission exhibits a N^{-1} dependence, indicating superfluorescent decay. The emission delay for the spherical cloud is considerably longer than for the case of the cigar-shaped cloud (peak 1). We attribute this difference to the fact that for the spherical cloud the value of μ and the atom density are lower than for the cigar-shaped cloud. For spherical atom clouds, we cannot resolve the SF emission from the cascade emission over the entire accessible range of N. The fact that for spherical clouds the SF and cascade emissions blend into one another may explain the fit offset of ∼70 ns for the case of the spherical cloud, apparent in Figure 38.

In future studies in cold atoms, it could be investigated if the expected SF cascade emissions at 5.2, 2.7, and 1.4 μm occur in the presence of incoherent excitation. Detection of time-resolved signals with adequate signal to noise ratio at these wavelengths would constitute the main experimental challenge. Applications of this work could extend to studies of dephasing processes, such as interatomic interactions, in cold atoms. Other applications could relate to Bose-condensed samples that typically have low atom numbers and verification of predicted statistical properties for spherical samples (Prasad & Glauber, 1985).

ACKNOWLEDGMENTS

We acknowledge Alexei Tonyushkin for useful comments on the manuscript.

Work at York University was supported by the institution and the Canada Foundation for Innovation, Ontario Innovation Trust, Natural Sciences and Engineering Research Council of Canada, and Ontario Centres of Excellence.

REFERENCES

Abella, I. D., Kurnit, N. A., & Hartmann, S. R. (1965). Photon echoes. *Physical Review*, *141*, 391.

Allen, L., & Eberly, J. H. (1987). *Optical resonance and two-level atoms*. New York: Dover.

Andersen, M. F., & Sleator, T. (2009). Lattice interferometer for laser-cooled atoms. *Physical Review Letters*, *103*, 070402.

Andrews, M. R., Townsend, C. G., Miesner, H. J., Durfee, D. S., Kurn, D. M., & Ketterle, W. (1997). Observation of interference between two bose condensates. *Science*, *275*, 637–641.
Anthony, J. M., & Sebastian, K. J. (1994). Relativistic corrections to the zeeman effect in hydrogenlike atoms and positronium. *Physical Review A*, *49*, 192.
Arecchi, F. T., & Courtens, E. (1970). Cooperative phenomena in resonant electromagnetic propagation. *Physical Review A*, *2*, 1730.
Arimondo, E., Inguscio, M., & Violino, P. (1977). Experimental determinations of the hyperfine structure in the alkali atoms. *Reviews of Modern Physics*, *49*, 31.
Audi, G., Wapstra, A. H., & Thibault, C. (2003). The ame2003 atomic mass evaluation (ii). tables, graphs and references. *Nuclear Physics A*, *729*, 337.
Bacon, A. M., Zhao, H. Z., Laverty, P. J., Wang, L. J., & Thomas, J. E. (1994). Photon-echo interferometry to measure collision-induced optical phase shifts. *Physical Review A*, *49*, 379–396.
Barger, R. L., Bergquist, J. C., English, T. C., & Glaze, D. J. (1979). Resolution of photon-recoil structure of the 6573-å calcium line in an atomic beam with optical ramsey fringes. *Applied Physics Letters*, *34*, 850.
Barrett, B., Yavin, I., Beattie, S., & Kumarakrishnan, A. (2010). Numerical simulation of a multi-level atom interferometer. *Physical Review A*, *82*, 023625.
Beattie, S., Barrett, B., Chan, I., Mok, C., Yavin, I., & Kumarakrishnan, A. (2009a). Atom interferometric studies of light scattering. *Physical Review A*, *80*, 013618.
Beattie, S., Barrett, B., Chan, I., Mok, C., Yavin, I., & Kumarakrishnan, A. (2009b). Technique for measuring atomic recoil frequency using coherence functions. *Physical Review A*, *79*, 021605(R).
Beattie, S., Barrett, B., Weel, M., Chan, I., Mok, C., Cahn, S. B., et al. (2008). Influence of spontaneous emission on a single-state atom interferometer. *Physical Review A*, *77*, 013610.
Becker, P. C., Fragnito, H. L., Cruz, C. H. B., Fork, R. L., Cunningham, J. E., Henry, J. E., et al. (1988). Femtosecond photon echoes from band-to-band transitions in gaas. *Physical Review Letters*, *61*, 1647.
Bergquist, J. C., Lee, S. A., & Hall, J. L. (1977). Saturated absorption with spatially separated laser fields: observation of optical "ramsey" fringes. *Physical Review Letters*, *38*, 159.
Berman, P. R. (1991). Nonlinear spectroscopy and laser cooling. *Physical Review A*, *43*, 1470.
Berman, P. R. (Ed.), (1997). *Atom interferometry*. San Diego: Academic Press.
Berman, P. R., & Malinovsky, V. S. (2011). *Principles of laser spectroscopy and quantum optics*. Princeton: Princeton University Press.
Berman, P. R., Rogers, G., & Dubetsky, B. (1993). Rate equations between electronic-state manifolds. *Physical Review A*, *48*, 1506.
Blundell, S. A., Johnson, W. R., & Sapirstein, J. (1991). Relativistic all-order calculations of energies and matrix elements in cesium. *Physical Review A*, *43*, 3407.
Bonifacio, R., & Lugiato, L. A. (1975). Cooperative radiation processes in two-level systems: superfluorescence. *Physical Review A*, *11*, 1507.
Bordé, C. J., Salomon, C., Avrillier, S., van Lerberghe, A., Bréant, A., Bassi, D., et al. (1984). Optical ramsey fringes with traveling waves. *Physical Review A*, *30*, 1836.
Bowden, C. M., & Sung, C. C. (1978). Cooperative behavior among three-level systems: transient effects of coherent optical pumping. *Physical Review A*, *18*, 1558.
Brownell, J. H., Lu, X., & Hartmann, S. R. (1995). Yoked superfluorescence. *Physical Review Letters*, *75*, 3265.
Burke, J. H. T., & Sackett, C. A. (2009). Scalable bose-einstein-condensate sagnac interferometer in a linear trap. *Physical Review A*, *80*, 061603.
Cadoret, M., de Mirandes, E., Cladé, P., Guellati-Khélifa, S., Schwob, C., Nez, F., et al. (2008). Combination of bloch oscillations with a ramsey-bordé interferometer: new determination of the fine structure constant. *Physical Review Letters*, *101*, 230801.
Cahn, S. B. (1997). Matter wave interference. Ph.D. thesis, Stony Brook, NY: State University of New York at Stony Brook 11794-3800.
Cahn, S. B., Kumarakrishnan, A., Shim, U., Sleator, T., Berman, P. R., & Dubetsky, B. (1997). Time-domain de broglie wave interferometry. *Physical Review Letters*, *79*, 784.
Campbell, G. K., Leanhardt, A. E., Mun, J., Boyd, M., Streed, E. W., Ketterle, W., et al. (2005). Photon recoil momentum in dispersive media. *Physical Review Letters*, *94*, 170403.

Cataliotti, F. S., Scheunemann, R., Hänsch, T. W., & Weitz, M. (2001). Superresolution of pulsed multiphoton raman transitions. *Physical Review Letters*, *87*, 113601.

Chan, I., Andreyuk, A., Beattie, S., Barrett, B., Mok, C., Weel, M., et al. (2008). Properties of magnetic sublevel coherences for precision measurements. *Physical Review A*, *78*, 033418.

Chapman, M. S., Hammond, T. D., Lenef, A., Schmiedmayer, J., Rubenstein, R. A., Smith, E., et al. (1995). Photon scattering from atoms in an atom interferometer: coherence lost and regained. *Physical Review Letters*, *75*, 3783.

Chen, Y. C., Chiang, K., & Hartmann, S. R. (1980). Spectroscopic and relaxation character of the $^3P_0$-$^3H_4$ transition in LaF_3:Pr^{3+} measured by photon echoes. *Physical Review B*, *21*, 40.

Chiow, S. W., Herrmann, S., Chu, S., & Müller, H. (2009). Noise-immune conjugate large-area atom interferometers. *Physical Review Letters*, *103*, 050402.

Cladé, P., de Mirandes, E., Cadoret, M., Guellati-Khélifa, S., Schwob, C., Nez, F., et al. (2006). Determination of the fine structure constant based on bloch oscillations of ultracold atoms in a vertical optical lattice. *Physical Review Letters*, *96*, 033001.

Cohen-Tannoudji, C., Dupont-Roc, J., & Grynberg, G. (1997). *Photons and atoms*. New York: Wiley-Interscience.

Cohen-Tannoudji, C., Dupont-Roc, J., & Grynberg, G. (1998). *Atom-photon interactions*. New York: Wiley-Interscience.

Cohen-Tannoudji, C., DuPont-Roc, J., Haroche, S., & Laloë, F. (1969). Detection of the static magnetic field produced by the oriented nuclei of optically pumped ^{3}He gas. *Physical Review Letters*, *22*, 758.

Cohen-Tannoudji, C., & Kastler, A. (1966). *Progress in optics* (Vol. V). Amsterdam: Elsevier.

Dicke, R. H. (1954). Coherence in spontaneous radiation processes. *Physical Review*, *93*, 99.

Dubetsky, B. (1997). (private communication).

Dubetsky, B., & Berman, P. R. (1994). Magnetic grating free induction decay and magnetic grating echo. *Laser Physics*, *4*, 1017.

Dubetsky, B., & Berman, P. R. (1997). Ground-state ramsey fringes. *Physical Review A*, *56*, R1091.

Dubetsky, B., & Kasevich, M. A. (2006). Atom interferometer as a selective sensor of rotation or gravity. *Physical Review A*, *74*, 023615.

Durfee, D. S., Shaham, Y. K., & Kasevich, M. A. (2006). Long-term stability of an area-reversible atom-interferometer sagnac gyroscope. *Physical Review Letters*, *97*, 240801.

Durr, S., Nonn, T., & Rempe, G. (1998). Origin of quantum-mechanical complementarity probed by a "which-way" experiment in an atom interferometer. *Nature*, *395*, 33–37.

Dzuba, V. A., Flambaum, V. V., Krafmakher, A. Y., & Sushkov, O. P. (1989). Summation of the high orders of perturbation theory in the correlation correction to the hyperfine structure and to the amplitudes of e1-transitions in the caesium atom. *Physical Letters A*, *142*, 373.

Edmonds, A. (1996). *Angular momentum in quantum mechanics*. San Diego: Princeton University Press.

Fixler, J. B., Foster, G. T., McGuirk, J. M., & Kasevich, M. A. (2007). Atom interferometer measurement of the newtonian constant of gravity. *Science*, *315*, 74.

Flusber, A., Mossberg, T., & Hartmann, S. R. (1978). Excited-state photon-echo relaxation in Na vapor. *Optics Communications*, *24*, 207.

Forber, R. A., Spinelli, L., Thomas, J. E., & Feld, M. S. (1990). Observation of quantum diffractive velocity-changing collisions by use of two-level heavy optical radiators. *Physical Review Letters*, *50*, 331.

Gaubatz, U., Rudecki, P., Schiemann, S., & Bergmann, K. (1990). Population transfer between molecular vibrational levels by stimulated raman scattering with partially overlapping laser fields. A new concept and experimental results. *The Journal of Chemical Physics*, *92*, 5363.

Gibbs, H. M., Vrehen, Q. H. F., & Hikspoors, H. M. J. (1977). Single-pulse superfluorescence in cesium. *Physical Review Letters*, *39*, 547.

Glauber, R. J., & Haake, F. (1976). Superradiant pulses and directed angular momentum states. *Physical Review A*, *13*, 357.

Greiner, M., Mandel, O., Esslinger, T., Hänsch, T. W., & Bloch, I. (2002). Quantum phase transition from a superfluid to a mott insulator in a gas of ultracold atoms. *Nature*, *415*, 39.

Gross, M., Fabrem, C., Pillet, P., & Haroche, S. (1976). Observation of near-infrared dicke superradiance on cascading transitions in atomic sodium. *Physical Review Letters*, *36*, 1035.
Gross, M., & Haroche, S. (1982). Superradiance: an essay on the theory of collective spontaneous emission. *Physics Reports*, *93*, 301.
Grove, T. T., Sanchez-Villicana, V., Duncan, B. C., Malecki, S., & Gould, P. L. (1995). Two-photon two-color diode laser spectroscopy of the Rb $5D_{5/2}$ state. *Physica Scripta*, *52*, 271.
Gupta, S., Dieckmann, K., Hadzibabic, Z., & Pritchard, D. E. (2002). Contrast interferometry using bose-einstein condensates to measure h/m and α. *Physical Review Letters*, *89*, 140401.
Gustavson, T. L., Bouyer, P., & Kasevich, M. A. (1997a). Precision rotation measurements with an atom interferometer gyroscope. *Physical Review Letters*, *78*, 2046.
Gustavson, T. L., Bouyer, P., & Kasevich, M. A. (1997b). Precision rotation measurements with an atom interferometer gyroscope. *Physical Review Letters*, *78*, 2046.
Gustavson, T. L., Landragin, A., & Kasevich, M. A. (2000). Rotation sensing with a dual atom-interferometer sagnac gyroscope. *Classical Quantum Gravity*, *17*, 2385.
Haake, F., King, H., Schröder, G., & Haas, J. (1979). Macroscopic quantum fluctuations in superfluorescence. *Physical Review Letters*, *42*, 1740.
Hackermüller, L., Hornberger, K., Brezger, B., Zeilinger, A., & Arndt, M. (2004). Decoherence of matter waves by thermal emission of radiation. *Nature*, *427*, 711–714.
Hagley, E. W., Deng, L., Kozuma, M., Trippenbach, M., Band, Y. B., Edwards, M., et al. (1999). Measurement of the coherence of a bose-einstein condensate. *Physical Review Letters*, *83*, 3112.
Hahn, E. L. (1950a). Spin echoes. *Physical Review*, *80*, 580.
Hahn, E. L. (1950b). Spin echoes. *Physical Review*, *80*, 580.
Hanneke, D., Fogwell, S., & Gabrielse, G. (2008). New measurement of the electron magnetic moment and the fine structure constant. *Physical Review Letters*, *100*, 120801.
Hughes, K. J., Burke, J. H. T., & Sackett, C. A. (2009). Suspension of atoms using optical pulses, and application to gravimetry. *Physical Review Letters*, *102*, 150403.
Kasevich, M., & Chu, S. (1991). Atomic interferometry using stimulated raman transitions. *Physical Review Letters*, *67*, 181.
Keith, D. W., Schattenburg, M. L., Smith, H. I., & Pritchard, D. E. (1988). Diffraction of atoms by a transmission grating. *Physical Review Letters*, *61*, 1580.
Kokorowski, D. A., Cronin, A. D., Roberts, T. D., & Pritchard, D. E. (2001). From single- to multiple-photon decoherence in an atom interferometer. *Physical Review Letters 86*, 2191.
Kumarakrishnan, A., Cahn, S. B., Shim, U., & Sleator, T. (1998a). Magnetic grating echoes from laser-cooled atoms. *Physical Review A*, *58*, R3387.
Kumarakrishnan, A., Chudasama, S., & Han, X. L. (2005). Collision-induced superfluorescence. *Journal of the Optical Society of America B*, *22*, 1538.
Kumarakrishnan, A., & Han, X. L. (1998). Superfluorescence from optically trapped calcium atoms. *Physical Review A*, *58*, 4153.
Kumarakrishnan, A., Shim, U., Cahn, S. B., & Sleator, T. (1998b). Ground-state grating echoes from rb vapor at room temperature. *Physical Review A*, *58*, 3868.
Lamporesi, G., Bertoldi, A., Cacciapuoti, L., Prevedelli, M., & Tino, G. M. (2008). Determination of the newtonian gravitational constant using atom interferometry. *Physical Review Letters*, *100*, 050801.
Le Gouët, J., Mehlstäubler, T. E., Kim, J., Merlet, S., Clairon, A., Landragin, A., et al. (2008). Limits to the sensitivity of a low noise compact atomic gravimeter. *Applied Physics B*, *92*, 133.
Lvovsky, A. I., Hartmann, S. R., & Moshary, F. (2002). Superfluorescence-stimulated photon echoes. *Physical Review Letters*, *89*, 263602.
Lvovsky, A. L., & Hartmann, S. R. (1999). Omnidirectional superfluorescence. *Physical Review Letters*, *82*, 4420.
Macfarlane, R. M., & Shelby, R. M. (1981). Sub-kilohertz optical linewidths of the $^7F_0 \leftrightarrow {}^5D_0$ transition in Y_2O_3: Eu^{3+}. *Optics Communications*, *39*, 169.
MacGillivray, J. C., & Feld, M. S. (1985). Coherent ringing in superfluorescence. *Physical Review Letters*, *54*, 677.
Maki, J. J., Malcuit, M. S., Raymer, M. G., Boyd, R. W., & Drummond, P. D. (1989). Influence of collisional dephasing processes on superfluorescence. *Physical Review A*, *40*, 5135.

Mandel, L. (1979). Distribution of atomic momentum in resonance fluorescence. *Journal of Optics (Paris)*, *10*, 51.

McAlexander, W. I., Abraham, E. R. I., & Hulet, R. G. (1996). Radiative lifetime of the 2p state of lithium. *Physical Review A*, *54*, R5.

McGuirk, J. M., Foster, G. T., Fixler, J. B., Snadden, M. J., & Kasevich, M. A. (2002). Sensitive absolute-gravity gradiometry using atom interferometry. *Physical Review A*, *65*, 033608.

Moehring, D. L., Blinov, B. B., Gidley, D. W., Kohn, R. N., Madsen, M. J., Sanderson, T. B., et al. (2006). Precision lifetime measurement of a single trapped ion with ultrafast laser pulses. *Physical Review A*, *73*, 023413.

Muller, H., Chiow, S. W., Herrmann, S., & Chu, S. (2008). Atom-interferometry tests of the isotropy of post-newtonian gravity. *Physical Review Letters*, *100*, 031101.

Müller, H., Peters, A., & Chu, S. (2010). A precision measurement of the gravitational redshift by the interference of matter waves. *Nature*, *463*, 926.

Oates, C. W., Vogel, K. R., & Hall, J. L. (1996). High precision linewidth measurement of laser-cooled atoms: resolution of the Na 3p $^2P_{3/2}$ lifetime discrepancy. *Physical Review Letters*, *76*, 2866.

Ovchinnikov, Y. B., Muller, J. H., Doery, M. R., Vredenbregt, E. J. D., Helmerson, K., Rolston, S. L., et al. (1999). Diffraction of a released bose-einstein condensate by a pulsed standing light wave. *Physical Review Letters*, *83*, 284.

Paradis, E., Barrett, B., Kumarakrishnan, A., Zhang, R., & Raithel, G. (2008). Observation of superfluorescent emissions from laser-cooled atoms. *Physical Review A*, *77*, 043419.

Patel, C. K. N., & Slusher, R. E. (1968). Photon echoes in gases. *Physical Review Letters*, *20*, 1087.

Peters, A., Chung, K. Y., & Chu, S. (1999). Measurement of gravitational acceleration by dropping atoms. *Nature*, *400*, 849.

Pfau, T., Spalter, S., Kurtsiefer, C., Ekstrom, C. R., & Mlynek, J. (1994). Loss of spatial coherence by a single spontaneous emission. *Physical Review Letters*, *73*, 1223.

Polder, D., Schuurmans, M. F. H., & Vrehen, Q. H. F. (1979). Superfluorescence: quantum-mechanical derivation of maxwell-bloch description with fluctuating field source. *Physical Review A*, *19*, 1192.

Poli, N., Wang, F., Tarallo, M. G., Alberti, A., Prevedelli, M., & Tino, G. M. (2011). Precision measurement of gravity with cold atoms in an optical lattice and comparison with a classical gravimeter. *Physical Review Letters*, *106*, 038501.

Prasad, S., & Glauber, R. J. (1985). Initiation of superfluorescence in a large sphere. *Physical Review A*, *31*, 1583.

Raizen, M. G. (1999). Quantum chaos with cold atoms. *Advances in Atomic, Molecular, and Optical Physics*, *41*, 43.

Raymer, M. G., & Walmsley, I. A. (1990). The quantum coherence properties of stimulated raman scattering. *Progress in Optics*, *28*, 181.

Rehler, N. E., & Eberly, J. H. (1971). Superradiance. *Physical Review A*, *3*, 1735.

Rochester, S. M., & Budker, D. (2001). Atomic polarization visualized. *American Journal of Physics*, *69*, 450.

Rotberg, E., Barrett, B., Beattie, S., Chudasama, S., Weel, M., Chan, I., et al. (2007). Measurement of excited state lifetime using two-pulse photon echoes in rubidium vapor. *Journal of the Optical Society of America B*, *24*, 671.

Ruschewitz, F., Peng, J. L., Hinderthür, H., Schaffrath, N., Sengstock, K., & Ertmer, W. (1998). Sub-kilohertz optical spectroscopy with a time domain atom interferometer. *Physical Review Letters*, *80*, 3173.

Safronova, M. S., Williams, C. J., & Clark, C. W. (2004). Relativistic many-body calculations of electric-dipole matrix elements, lifetimes and polarizabilities in rubidium. *Physical Review A*, *69*, 022509.

Sansonetti, J. E. (2006). Wavelengths, transition probabilities, and energy levels for the spectra of rubidium (rb i through rb xxxvii), volume = 35, pages = 301, note = from NIST Atomic Spectra Database (version 3.1.2), [Online]. Available: http://physics.nist.gov/asd3 [2007, May 7]. National Institute of Standards and Technology, Gaithersburg, MD. Journal of Physical Chemistry Ref. Data.

Schneble, D., Torii, Y., Boyd, M., Steed, E. W., Pritchard, D. E., & Ketterle, W. (2003). The onset of matter-wave amplification in a superradiant bose-einstein condensate. *Science*, *300*, 475.

Schuurmans, M. F. H. (1980). Superfluorescence and amplified spontaneous emission in an inhomogeneously broadened medium. *Optics Communications*, *34*, 185.

Sengstock, K., Sterr, U., Hennig, G., Bettermann, D., Müller, J., & Ertmer, W. (1993). Optical ramsey interferences on laser-cooled and trapped atoms, detected by electron shelving. *Optics Communications*, *103*, 73.

Shim, U., Cahn, S., Kumarakrishnan, A., Sleator, T., & Kim, J. (2002). Optical free induction decay in cold ^{85}Rb atoms. *Japanese Journal of Applied Physics*, 41, 3688.

Shim, U., Cahn, S. B., Kumarakrishnan, A., Sleator, T., & Kim, J. (2005). Optical nutation in cold ^{85}Rb atoms. *Japanese Journal of Applied Physics*, *44*, 168.

Shore, B. W. (1990). *The theory of coherent atomic excitation*. San Diego: Wiley.

Simsarian, J. E., Orozco, L. A., Sprouse, G. D., & Zhao, W. Z. (1998). Lifetime measurements of the 7p levels of atomic francium. *Physical Review A*, *57*, 2448.

Skribanowitz, N., Herman, I. P., MacGillivray, J. C., & Feld, M. S. (1973). Observation of dicke superradiance in optically pumped HF gas. *Physical Review Letters*, *30*, 309.

Sleator, T., Berman, P. R., & Dubetsky, B. (1999). High precision atom interferometry in a microgravity environment. arXiv physics/9905047v1 [physics.atom-ph].

Smiciklas, M., & Shiner, D. (2010). Determination of the fine structure constant using helium fine structure. *Physical Review Letters*, *105*, 123001.

Snadden, M. J., McGuirk, J. M., Bouyer, P., Haritos, K. G., & Kasevich, M. A. (1998). Measurement of the earth's gravity gradient with an atom interferometer-based gravity gradiometer. *Physical Review Letters*, *81*, 971.

Spielman, I. B., Phillips, W. D., & Porto, J. V. (2007). Mott-insulator transition in a two-dimensional atomic bose gas. *Physical Review Letters*, *98*, 080404.

Strekalov, D. V., Turlapov, A., Kumarakrishnan, A., & Sleator, T. (2002). Periodic structures generated in a cloud of cold atoms. *Physical Review A*, *66*, 023601.

Taylor, B. (1994). Determining the avogadro constant from electrical measurements. *Metrologia*, *31*, 181.

Thomas, J. E., & Wang, L. J. (1995). Precision position measurement of moving atoms. *Physics Reports*, *262*, 311.

Tonyushkin, A., & Prentiss, M. (2009). Selective manipulation of degenerate interferometer loops by an atom-optics kicked rotor. *Physical Review A*, *78*, 053625.

Tonyushkin, A., & Prentiss, M. G. (2010). Straight macroscopic magnetic guide for cold atom interferometer. *Journal of Applied Physics*, *108*, 094904.

Tonyushkin, A., Wu, S., & Prentiss, M. (2009a). Demonstration of a multipulse interferometer for quantum kicked-rotor studies. *Physical Review A*, *79*, 051402.

Tonyushkin, A., Wu, S., & Prentiss, M. (2009b). Demonstration of a multipulse interferometer for quantum kicked-rotor studies. *Physical Review A*, *79*, 051402(R).

Turlapov, A., Tonyushkin, A., & Sleator, T. (2005). Talbot-lau effect for atomic de broglie waves manipulated with light. *Physical Review A*, *71*, 043612.

Uys, H., Perreault, J. D., & Cronin, A. D. (2005). Matter-wave decoherence due to a gas environment in an atom interferometer. *Physical Review Letters*, *95*, 150403.

Vali, V., & Shorthill, R. W. (1976). Fiber ring interferometer. *Applied Optics*, *15*, 1099.

Vasilenko, L. S., Matveyenko, I. D., & Rubtsova, N. N. (1985). Study of narrow resonances of coherent radiation in time separated fields in SF_6. *Optics Communications*, *53*, 371.

Volz, U., & Schmoranzer, H. (1996). Precision lifetime measurements on alkali atoms and on helium by beam-gas-laser spectroscopy. *Physica Scripta*, *T65*, 48.

Vorozcovs, A., Weel, M., Beattie, S., Cauchi, S., & Kumarakrishnan, A. (2005). Measurements of temperature scaling laws in an optically dense magneto-optical trap. *Journal of the Optical Society of America B*, *22*, 943.

Vrehen, Q. H. F., Gibbs, H. M., & Bonifacio, R. (1982). *Dissipative systems in quantum optics*. Berlin: Springer-Verlag.

Watson, G. N. (1980). *A treatise on the theory of bessel functions*. Cambridge: Cambridge University Press.

Weel, M., Chan, I., Beattie, S., Kumarakrishnan, A., Gosset, D., & Yavin, I. (2006). Effect of a magnetic field gradient and gravitational acceleration on a time domain grating echo interferometer. *Physical Review A*, *73*, 063624.

Weel, M., & Kumarakrishnan, A. (2003). Observation of ground state ramsey fringes. *Physical Review A*, *67*, 061602(R).

Weiss, D. S., Young, B. C., & Chu, S. (1993). Precision measurement of the photon recoil of an atom using atomic interferometry. *Physical Review Letters*, *70*, 2706.

White, C. W., Hughes, W. M., Hayne, G. S., & Robinson, H. G. (1968). Determination of g-factor ratios for free Rb^{85} and Rb^{87} atoms. *Physical Review*, *174*, 23.

Wicht, A., Hensley, J. M., Sarajlic, E., & Chu, S. (2002). A preliminary measurement of the fine structure constant based on atom interferometry. *Physica Scripta*, *T102*, 82–88.

Wu, S., Su, E., & Prentiss, M. (2007). Demonstration of an area-enclosing guided-atom interferometer for rotation sensing. *Physical Review Letters*, *99*, 173201.

Wu, S., Su, E. J., & Prentiss, M. (2005). Time domain de broglie wave interferometry along a magnetic guide. *The European Physical Journal D*, *35*, 111.

Wu, S., Tonyushkin, A., & Prentiss, M. (2009). Observation of saturation of fidelity decay with an atom interferometer. *Physical Review Letters*, *103*, 034101.

Young, B., Bonomi, D. S., Patterson, T., Roller, F., Tran, T., Vitouchkine, A., et al. (2007). Atom optic inertial and gravitational sensors. In: Proceedings of the International Conference on Laser Science. Optical Society of America, p. LTuH1.

Young, L., Hill III, W. T., Sibener, S. J., Price, S. D., Tanner, C. E., Wieman, C. E., et al. (1994). Precision lifetime measurements of cs $6p\,^2P_{1/2}$ and $6p\,^2P_{3/2}$ levels by single-photon counting. *Physical Review A*, *50*, 2174.

Yu, N., Kohel, J. M., Kellogg, J. R., & Maleki, L. (2006). Development of an atom-interferometer gravity gradiometer for gravity measurement from space. *Applied Physics B*, *84*, 647.

Non-Print Items

Keywords: laser-cooled systems; Raman–Nath Condition; standing-wave pulse; traveling-wave pulse; matter waves